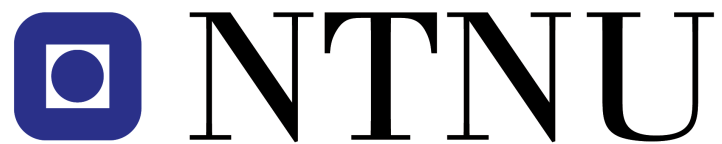

INSTRUMENTATION OF CRASH TESTING FOR
AUTOMOBILES

Stian Hoel

June 10, 2005



DEPARTEMENT OF ENGINEERING CYBERNETICS
NORWEGIAN UNIVERSITY OF SCIENCE AND TECHNOLOGY
TRONDHEIM NORWAY



MASTEROPPGAVE

Kandidatens navn: Stian Hoel
Fag: Teknisk Kybernetikk
Oppgavens tittel (norsk): Instrumentering for krasjtesting av biler
Oppgavens tittel (engelsk): *Instrumentation of crash testing for automobiles.*

Opgavens tekst:

Opgaven utføres i samarbeid med Hydro Aluminium Structures Raufoss AS. En testbil er påmontert komponenter (støtfanger, krasjbokser, eventuelt styrkekomponenter) for å teste ut hvordan disse fungerer i en krasjsituasjon. Denne bilen er instrumentert med lastceller og forskyvningsmålere. Da det er vanskelig å måle riktig ved dynamisk testing, foreslås det å bruke akselerometre for å måle hvordan bilen kastes til siden når vi krasjer på en side. I tillegg kan man da bruke sammenhengene mellom kraft, akselerasjon og forskyvning til å kontrollere måleresultatene mot hverandre samt definere en feilfaktor. Det vil bli en tidsforsinkele (grunnet dynamikk i måleinstrumenter) som må håndteres best mulig.

Data samples med 5000 Hz, Matlab og JAVA skal brukes til å visualisere resultatene.

Deloppgaver:

- Gjør et litteraturstudium der du vurderer vesentlige egenskaper ved forskjellige typer akselerometre
- Delta i testserie på testlabben på Raufoss
- Analysér resultatene, finn feilkilder og påpek punkter der utstyr og programvare kan forbedres
- Undersøk mulighetene for å bruke Kalmanfilter til å estimere tilstander.

Opgaven gitt: 10/1-05

Besvarelsen leveres: 13/6-05

Besvarelsen levert:

Utført ved Institutt for teknisk kybernetikk

Veileder: Tore Tryland, Hydro Aluminium Structures Raufoss AS

Trondheim, den 10/1-05

Jan Tommy Gravidahl
Faglærer

Preface

The work presented in the following is my Master thesis at the Norwegian University of Science and Technology (NUST), Department of Engineering Cybernetics.

I would like to thank my supervisor Associate Professor Tommy Gravdahl for his valuable inputs and guidance during this semester. I would also like to thank my adviser at Hydro Automotive Structures, Tore Tryland, for his help and the opportunity he gave me to write my thesis for Hydro. Finally, I would like to thank Associate Professor Arne Wold at Gjøvik University College for helping me with the Matlab source code.

Stian Hoel
Trondheim 10. June 2005.

Contents

Contents	iii
List of Figures	vi
Abstract	ix
1 Introduction	1
1.1 This thesis	1
1.2 Outline of the report	2
2 Accelerometer	4
2.1 Principles	4
2.2 Considerations when choosing an accelerometer	6
2.3 Accelerometer mounting considerations	7
2.4 Capacitive accelerometer	8
2.5 MEMS accelerometer	9
2.6 Piezoresistive accelerometer	9
2.7 Piezoelectric accelerometer	9
2.7.1 High and low impedance accelerometers	10
2.7.2 Piezoelectric materials	11
2.7.3 Mechanical configurations	11
2.8 Comparison of accelerometers	14
3 Theoretical background	17
3.1 Impacts and energy absorption	17
3.2 Accelerations tied to angular displacement	19
3.3 Computing the rotation	20
3.4 Mathematical modeling	22
3.5 The Kalman Filter	23
4 The Crash Test Lane	25
4.1 Test facility	25
4.1.1 Barrier	25
4.1.2 Test vehicle	26

4.1.3	The winch	26
4.1.4	High-speed cameraes	26
4.2	The instruments	26
4.2.1	Speed measurements	26
4.2.2	The laser (range finder)	27
4.2.3	Load-cells	28
4.2.4	Acceleration	29
4.3	The test procedures	29
4.3.1	AZT test	29
4.3.2	IIHS-test	30
4.3.3	Barrier test	30
4.3.4	The pendulum test	30
5	Analysis	31
5.1	Speed measuring unit	31
5.2	The lasers (range finders)	31
5.3	Load-cells	33
5.4	Accelerometers	34
6	Implementation of possible improvements	38
6.1	The problems	38
6.1.1	Displacement	38
6.1.2	The distance/compression measurement	38
6.1.3	Time delay	38
6.2	The different phases of the impact	40
6.3	Kalman filter	41
6.3.1	Accelerometer measurement	41
6.3.2	Accelerometer, load-cells, position and velocity measurement	42
6.3.3	Manufactured test data	43
6.4	Finding the rotation angle using the lasers	43
6.5	Force/Displacement plot	43
7	Results and discussion	45
7.1	Accelerometer measurements	45
7.2	Accelerometer, load-cells, velocity and position measurements	48
7.3	Manufactured test data	51
7.4	Finding the rotation angle using the lasers	55
7.5	Force/Displacement plot	56
7.6	Evaluation of the sensors and possible improvements in hardware	57
8	Conclusions and recommendations	59
8.1	Conclusion	59
8.2	Future work	60

References	61
A Simulink models	62
B Comparison of test-series.	65
C Plots from the results	69
C.1 w/ only accelerometer	69
C.2 w/ accelerometer, load-cells, position and velocity sensors	73
D Butterworth filter	74
E Data sheets	75
F CD-ROM contents	85
F.1 Plots	85
F.2 Matlab files	86

List of Figures

2.1	Transient response of a spring-mass system	5
2.2	A piezoresistive accelerometer	10
2.3	Shear Beam configuration and shear effect	12
2.4	Flexural beam configuration and longitudinal effect	13
2.5	Transverse effect	13
2.6	The three different compression modes(upright, inverted and isolated)	14
3.1	An example of a Load/Displacement plot.	18
3.2	A simple impact with two objects.	19
3.3	The two accelerations acting upon the accelerometer showed together with the accelerometer's axes.	20
3.4	The parameters needed to calculate the rotation angle.	21
4.1	The barrier.	25
4.2	The test vehicle.	27
4.3	Speed measurement instruments	28
4.4	The laser and the load-cell configuration.	28
4.5	AZT procedure	30
5.1	The pulse generated by the speed measuring unit(scaled).	32
5.2	The range finder arrangement.	32
5.3	The test vehicle's position in x-direction during impact.	33
5.4	Measurements from the individual load-cells	34
5.5	The total load on the left and right side of the bumper system.	35
5.6	The readings from accelerometer 1.	35
5.7	The readings from accelerometer 2.	36
5.8	The readings from accelerometer 3.	37
5.9	The mean values during the different phases.	37
6.1	Rotation of the test vehicle.	39
6.2	The compression error as a result of the rotation.	39
6.3	The Simulink model of the Kalman filter.	42
6.4	Calculation of the rotation angle using PGB3 and PGB4.	44

7.1	Results from series 9265	46
7.2	Rotation angle estimation in series 9265-9267	47
7.3	Results from series 9265	48
7.4	Rotation angle estimation in series 9265-9267	49
7.5	Results from the fabricated series without noise and the accelerometers as the only sensors.	51
7.6	Results from the fabricated series with noise and the accelerometers as the only sensors.	53
7.7	Results from the fabricated series with noise and the accelerometers, range finders and velocity measurement.	54
7.8	Rotation estimation based on range finder data.	55
7.9	Force/displacement plots using different measurements.	56
7.10	The effect of the rotation on the force/displacement plot.	57
A.1	Top-view of the Kalman filter in the Simulink diagram.	62
A.2	The Kalman filter.	63
A.3	The sensors in simulink. They get their data from *.mat files.	64
A.4	The Kalman Riccati equation.	64
B.1	Comparison of the acceleration measured in x-direction with accelerometer 1.	65
B.2	Comparison of the acceleration measured in y-direction with accelerometer 1.	66
B.3	Comparison of the acceleration measured in z-direction with accelerometer 1.	66
B.4	Comparison of the acceleration measured in x-direction with accelerometer 2.	67
B.5	Comparison of the acceleration measured in y-direction with accelerometer 2.	67
B.6	Comparison of the acceleration measured in x-direction with accelerometer 3.	68
B.7	Comparison of the acceleration measured in y-direction with accelerometer 3.	68
C.1	Results from series 9265	70
C.2	Results from series 9266	71
C.3	Results from series 9267	72
C.4	Results from series 9265	73
E.1	Data Sheet of the accelerometer 625B01.	76
E.2	Data Sheet of the accelerometer 629A31.	77
E.3	Data Sheet of the load-cells. The one used on the test facilities is U4200.	78
E.4	Model 350B50 Spec Sheet.	79
E.5	Model 356A12 Spec Sheet.	80
E.6	Model 352C23 Spec Sheet.	81
E.7	Model 3901F3HB2000G Spec Sheet.	82
E.8	Model 3703D1FE50G Spec Sheet.	83
E.9	Model 650A10 Spec Sheet.	84
F.1	CD-ROM contents.	85

Abstract

The topic of this work is instrumentation of crash testing for automobiles. The AZT test is performed with an offset barrier which causes the test vehicle to rotate slightly. If this rotation can be estimated, a better conformity with simulations can be obtained and improvement of the bumper system design will be easier.

The principles of different types of accelerometers are explained. Important considerations when choosing and mounting new accelerometers are introduced and recommendations made. The best accelerometer in a crash test scenario is found to be the piezoelectric accelerometer.

It became clear that the vibrations in the test vehicle during impact contaminate the acceleration readings. This renders the measurements useless with respect to estimation of the angular displacement. The vibrations measured had an amplitude larger than the accelerometers measurement range, and a frequency close to, or even larger than, their frequency range. This will introduce a bias error in the measurements.

Two solutions to the angular displacement are proposed. The first uses a Kalman filter to estimate the rotation, while the second uses two range finders to calculate it. The Kalman filter requires accelerometer measurements to function, and will not do so properly unless the vibrations can be filtered out or the accelerometers are swapped with new ones with higher frequency and measurement range. Except from the accelerometers, the sensors used in the crash tests perform satisfactory. The range finder solution, requires the purchase of new hardware, but seems to be a promising solution. It is found that the angular displacement has no direct effect on the force/displacement plots.

Chapter 1

Introduction

Hydro Aluminium Structures at Raufoss develops crash-boxes and bumpers in aluminium for the automobile industry. The objective is to produce a low-cost, lightweight design that absorbs as much energy as possible. Maximum absorption is obtained through design and choice of aluminium alloy.

The bumper systems of today need to fulfill several security requirements from both the government and the insurance industry. The requirements from the government deals mainly with security issues, while the insurance industry is interested in the degree of damage on the car and the repair costs as well. Since low-speed collisions make up a significant part of the total number of collisions, it is interesting to look at these in particular. Low-speed collisions are defined as collisions with an impact-speed of 15 km/h or less.

How well the bumper system performs in a test, will be of interest to the insurance companies which partially base the insurance premium on crash tests. For this reason, the car manufacturers require that the tests are performed with a small degree of uncertainty. Consequently it is important that all of the forces are measured and that the correct instruments are used to do this. When this is done, it becomes easier to improve the bumper system design in order to accommodate the requirements of the insurance companies and car manufacturers.

1.1 This thesis

The objective with this thesis is to determine what the best equipment for crash test analysis is, and how to process the information in order to obtain the desired information.

The bumper system is first and foremost designed to absorb energy in the direction of motion. In the AZT tests, described in section 4.3.1, the test vehicle will rotate slightly due to the offset barrier and introduce forces perpendicular to the direction of motion. Because of these forces, the bumper system, and the crash boxes in particular, may behave in a different way than expected. The result can be that they don't fold the way it were intended to, and absorb less energy than they would in the case of a homogenous force distribution. If the sideways forces are mapped, it may be easier to get a better conformity with simulation

results and improve the bumper system design.

There are some solutions on the market today to find the rotation angle. One of them uses a grid on the floor and a camera mounted above the barrier. It then computes the rotation angle using image processing. This solution, however, is very expensive and requires a very clean test facility. Another solution is to simply use a protractor. The problem with the protractor, is that it only gives information about the final rotation angle. When the rotation takes place, may be of as much importance as how large it is, and that information is unavailable when a protractor is used. Since there are no satisfactory solutions on the market today, or they are too expensive and impractical, this problem must be addressed.

1.2 Outline of the report

Chapter 1: Introduction

A short introduction to the thesis is given along with the motivation for doing it. An outline of the thesis is given as well.

Chapter 2: Accelerometer

The principles of accelerometers are described together with the mode of operation of different types of accelerometers. Important considerations when choosing and mounting an accelerometer are also given. Finally, there is a comparison of the types of accelerometers, and an appropriate accelerometer for crash testing is recommended.

Chapter 3: Theoretical background

In this chapter the theoretical background is given. This includes, among other things, impact and energy absorption theory, mathematical modeling and Kalman filter theory.

Chapter 4: The Crash Test Lane

In this chapter a brief introduction to the test facility and the instruments there is given. Different test procedures are described as well.

Chapter 5: Analysis

The different sensors' outputs during the crash test are analyzed and commented on.

Chapter 6: Implementation of possible improvements

The problems with the current implementation are identified and possible solutions suggested.

Chapter 7: Results and discussion

In this chapter the results of the solutions proposed in the previous chapter is presented and discussed.

Chapter 8: Conclusions and recommendations

The results are summarized and suggestions for future work are made.

Chapter 2

Accelerometer

There are several types of accelerometers with a variety of areas of application. In order to choose the correct accelerometer for the intended application, some considerations must be made. In this chapter, these considerations are pointed out. An introduction to the principles of the accelerometer and the most common accelerometer-designs are also given.

2.1 Principles

There are several different methods which can be used to measure acceleration, but in the industrial world the most common design uses a combination of Newton's law of mass and acceleration, and Hooke's law of spring action (Johnson 1997). Newton's law of mass and acceleration is given as

$$F = m \cdot a \quad (2.1)$$

and Hooke's law of spring action is

$$F = k \cdot \Delta x \quad (2.2)$$

where k is the spring constant and Δx is the distance from equilibrium. If Equation (2.1) and Equation (2.2) are combined, the measurement of acceleration is reduced to measuring the spring extension.

$$a = \frac{k}{m} \Delta x \quad (2.3)$$

The mass m that converts the acceleration to spring displacement is referred to as *seismic mass*.

A spring-mass system will always exhibit oscillations at some characteristic *natural frequency* (Johnson 1997). This natural frequency is given by

$$f_N = \frac{1}{2\pi} \sqrt{\frac{k}{m}} \quad (2.4)$$

Because of friction, the seismic mass will eventually come to rest. This friction is referred to as the *damping coefficient*. The friction and the oscillation gives a periodic damped signal

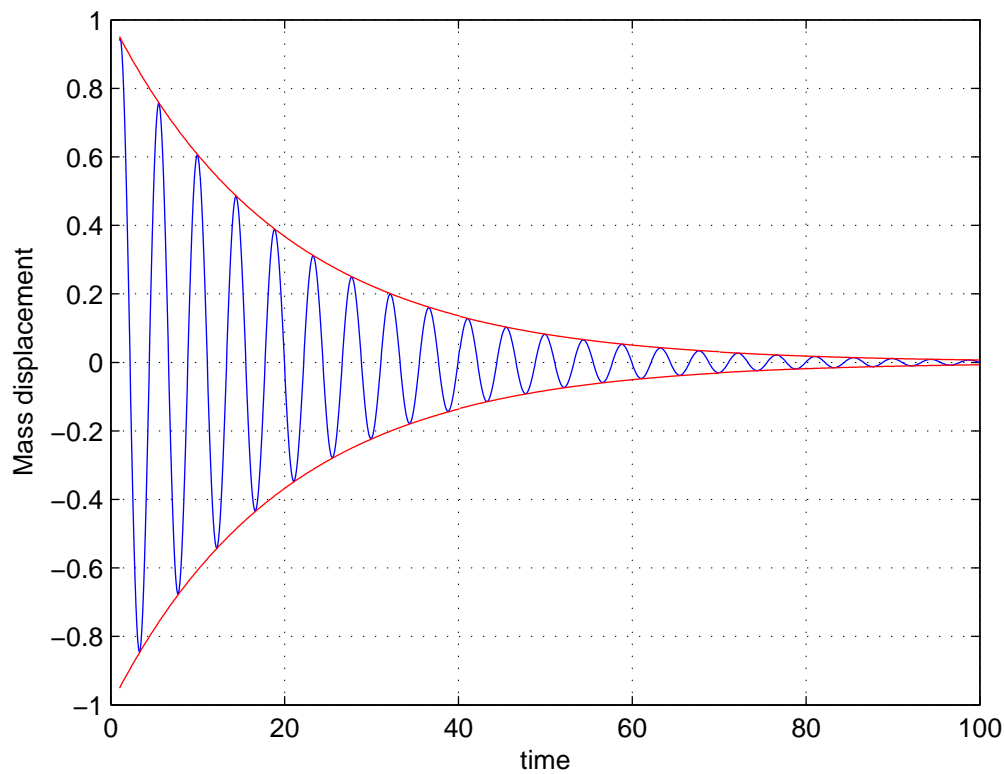


Figure 2.1: Transient response of a spring-mass system caused by an impulse input.

referred to as a *transient response*. The transient response has the equation

$$x_T(t) = x_0 e^{-\mu t} \sin(2\pi f_N t) \quad (2.5)$$

where x_T is the transient mass position, x_0 is the peak position, μ is the damping coefficient and f_N is the natural frequency. An example of a transient response is given in figure 2.1.

If a constant vibration is applied to the object at which the spring-mass system is mounted, it will result in an acceleration of this object described by the equation

$$a(t) = -\omega^2 x_0 \sin(\omega t) \quad (2.6)$$

where $\omega = 2\pi f$ and f is the applied vibration. Equation (2.6) is found by double differentiation of the equation for a simple periodic motion given by

$$x(t) = x_0 \sin(\omega t) \quad (2.7)$$

Combining Equation (2.6) with Equation (2.3) yields

$$\Delta x = -\frac{mx_0}{k} \omega^2 \sin(\omega t) \quad (2.8)$$

It is important to notice that this equation is not valid when the applied frequency, f , is close to the natural frequency, f_N . When this is the case, there is a resonance effect which makes the mass displacement, Δx peak. For Equation (2.8) to be valid, the applied frequency has to be $f < \frac{1}{2.5}f_N$. When the applied frequency is much larger than the natural frequency, the accelerometer is independent of the applied frequency and becomes measure of the vibration displacement, x_0 , instead. In this case, the seismic mass is stationary while the housing moves about the mass. Generally, this is said to yield when $f > 2.5 f_N$.

2.2 Considerations when choosing an accelerometer

When choosing an accelerometer, several considerations must be taken into account. In this section a brief overview and explanation of the different specifications will be given. Thompson (2000) is used as reference and also contains some additional information and examples.

Amplitude range

Select an accelerometer which is capable of reflecting the expected acceleration levels in its output. Furthermore, to be able to measure unexpectedly large accelerations, the expected acceleration levels should be within the lower 20% of the accelerometer's response range.

Shock limits

The shock limits explains how many g's of shock the accelerometer can withstand. Shocks that are much higher than the accelerometer is built for, can easily damage it and render it useless. It is important to treat the accelerometer very carefully since even a 5 cm drop onto a benchtop easily can create a spike of 2000 g.

Temperature range

Every accelerometer has an operating temperature, and it is important to make sure that it never is exposed to temperatures greater or lower than this. If so happens, the accelerometer can easily be damaged. Accelerometers can operate in temperatures up to 500°C, but normally the maximum operating temperature will be just under 300°C.

Base strain sensitivity

If the accelerometer is mounted on a concave surface, the base of the accelerometer is strained. This can alter its sensitivity. If the accelerometer is to be mounted on an uneven surface, it

would be a good idea to weld flat mounting-pads on the surface to avoid base strain. The mounting-pads should not alter the mechanical properties of the object it is welded onto significantly.

Transverse sensitivity

To achieve the specified accuracy, it is important that the accelerometer's axis is aligned perfectly with the direction of the acceleration that should be measured. If the accelerometer isn't perfectly aligned, it will produce errors when subject to lateral acceleration.

Frequency range

Every accelerometer has a frequency range in which it operates. If this range is exceeded, the accelerometer will give a faulty output and may be damaged. The frequency-response limits should be handled in the same manner as the amplitude limits described earlier, i.e. they should not be "overcrowded". Thompson (2000) suggests using only 20% of the accelerometer's response curve.

2.3 Accelerometer mounting considerations

In this section, a few important considerations when mounting the accelerometers are listed. It is largely based on information found in PCB Piezotronics (2005).

Frequency response

The mounting technique has a considerable effect on an accelerometer's accuracy of the usable frequency response. A direct coupling, stud mounted to a smooth surface, will generally give the broadest usable frequency range, i.e. it yields the highest mechanical resonant frequency. The addition of any mass to the accelerometer, such as adhesive or magnetic mounting base described later, lowers the usable frequency range and may affect the accuracy of the accelerometer. Compliant materials, such as a rubber interface pad, can also create a mechanical filtering effect which damps high-frequency signals.

Surface preparation

A smooth and flat machined surface where the accelerometer can be attached is very important when measuring at high frequencies. This will give good high-frequency transmissibility. A thin layer of silicon grease between the base and the mounting surface will give an even higher degree of intimate surface contact.

Stud mounting

For permanent installations stud mounting is recommended. First, the surface is prepared and a hole is drilled. Then the accelerometer with the mounting stud is installed. Silicone grease should be used to ensure high-frequency transmissibility.

Screw mounting

Screw mounting can be an acceptable way to secure an accelerometer when it is mounted on a thin-walled structure. However, the screw engagement length should always be checked to ensure that the screw doesn't bottom into the accelerometer base. Also in this case, silicone grease can be used to ensure high-frequency transmissibility.

Adhesive mounting

Adhesive mounting offers an alternative mounting method. It is recommended that a separate adhesive mounting base is used to prevent the adhesive from damaging the accelerometer. There are many different types of adhesives that can be used, based on the particular application. Dental cement, hot glues, instant glues and duct putty are examples on adhesives that have been used with success. This mounting method will tend to somewhat damp the higher frequency and lower the frequency response.

Magnetic mounting

Magnetic mounting bases can be used as a convenient, temporary attachment method to magnetic surfaces. When the surface is uneven or non-magnetic, steel pads can be welded in place. Magnets with high pull strength will offer the best high-frequency response. A layer of silicone grease between the accelerometer base and the magnetic mounting base will improve the high-frequency response further.

Cables and connections

If the cables aren't securely fastened, a phenomenon called triboelectric effect may occur. This is when cable whip introduces noise, especially in high-impedance signal paths. To avoid this, cables should be securely fastened with tape, a clamp, or some other adhesive. Securing the cables will also help minimizing connector strain which can lead to intermittent or broken connections and loss of data.

2.4 Capacitive accelerometer

The capacitive accelerometer is based upon the fact that the capacitance between two plates depends on the distance between them. The seismic mass is formed in such a way that it becomes the middle plate of three, which the capacitance is measured between. When subject to a load, the middle plate will shift either one way or the other. The distance it shifts can

be calculated by measuring the two capacitance values on each side of the middle plate. The capacitive accelerometer offers true static-load response, also called DC response. This means that the accelerometer can measure constant acceleration as well as dynamic acceleration. As will be seen later in this chapter, the piezoresistive and piezoelectric accelerometers lack this ability. Capacitive accelerometers can be made very small, and are very versatile. They operate well at almost every frequency except at very high frequencies.

2.5 MEMS accelerometer

Microelectromechanical system (MEMS) sensors have micromachined silicon mechanical components and integrated support electronics. Earlier versions of MEMS sensors used resistive elements, but in today's sensors, capacitive sensors are used. The use of capacitive sensors instead of resistive elements, allows the accelerometers to be very small and the MEMS accelerometer will give true static-load response as well. Typical areas of application for the MEMS sensors are widespread, including camcorders and digital cameras, advanced robotics, sensing for airbag control and active suspension.

The basic MEMS accelerometer consists of two parts: the sensor chip and the integrated electronics. The sensor chip is basically a micromachined capacitive accelerometer. Because the sensor chip only gives a very small capacitance reading (about 0.15 pF), the integrated electronics are needed to convert this small signal into a useful electrical signal. The integrated electronics can be constructed to produce either an analog or a digital output. In the digital case, the integrated electronics generate a pulse stream whose pulse density is proportional to the acceleration. The analog integrated electronics solution generates a differential voltage output proportional to the acceleration.

2.6 Piezoresistive accelerometer

The piezoresistive accelerometers use a piezoresistive material to measure the acceleration. A piezoresistive material reacts to a change in acceleration by changing its resistance. This change can be measured by using an input voltage on the accelerometer and measuring the current which will be proportional to the acceleration. A basic sketch of a piezoresistive accelerometer is given in figure 2.2. In this figure the beam acts as seismic mass.

2.7 Piezoelectric accelerometer

The piezoelectric effect was discovered in 1880 by Pierre and Jacques Curie. They discovered that certain crystals exhibit electrical charges when subject to mechanical stress, but saw no practical use of this effect. In the 1950s the piezoelectric effect was commercialized since it now was possible to amplify the signals from the piezoelectric crystals into a useful signal. Today, piezoelectric accelerometers are used in almost every area of modern technology and

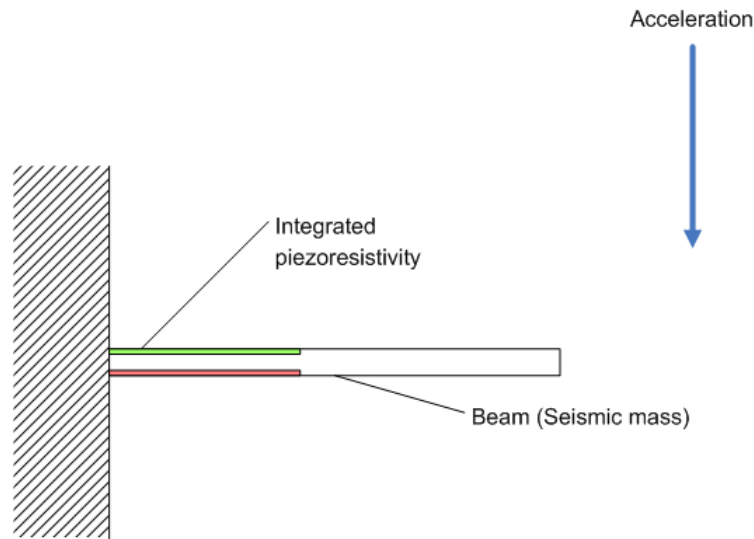


Figure 2.2: A piezoresistive accelerometer with a beam with integrated piezoresistivity

industry. Kulwanoski & Schnellinger (2004) and PCB Piezotronics (2005) has been used as references in this section.

The main difference between the piezoresistive and the piezoelectric accelerometer is that the latter can be regarded as "active" as opposed to the former which is "passive". With active, we mean that it doesn't need any input to give a signal. It merely gives an electrical charge when subject to a change in load, while passive means that we need to measure the change in resistance by using a voltage input.

2.7.1 High and low impedance accelerometers

There are two types of piezoelectric accelerometers; high and low impedance. High impedance units have a charge output which either needs a charge amplifier or an external charge-to-voltage converter. The low impedance units has a miniaturized charge-to-voltage converter incorporated in the unit. The piezoelectric sensing elements are the same in low- and high-impedance accelerometers, but based on size and preferred way of transfer (charge or voltage), the unit best suited for the particular case can be used. High impedance units are typically more versatile since the absence of built-in electronics means that it has a wider operating temperature. It is also easier to adjust the external charge amplifier so that the accelerometer can be tuned depending on the area of application. Low impedance units, however, are tailored to a specific application and are ideal when measuring frequency and temperature ranges are well defined. The low impedance units will generally be cheaper as well.

2.7.2 Piezoelectric materials

There are several piezoelectric materials available, but the preferred material in sensor design is quartz. The reason for this is that quartz have several useful properties such as (Kulwanoski & Schnellinger 2004):

- Material stress limit of 20000 psi
- Temperature resistance up to 500° C
- Very high rigidity, high linearity and negligible hysteresis
- Almost constant sensitivity over a wide temperature range
- Ultra-high insulation resistance (10¹⁴Ω), allowing low-frequency measurements (< 1 Hz)

The voltage sensitivity is high, making it ideal for voltage-amplified system. However, the charge sensitivity is low, making it less useful in charge-amplified systems. In this case ceramic materials can be used as the piezoelectric material. Ceramic materials are forced to become piezoelectric by a polarization process. Unfortunately, because this is not a natural state for the ceramic material, it will tend to reverse itself over time until it reaches a steady state. This is not the case with quartz since it is naturally piezoelectric. The ceramic material can be altered or destroyed by high temperatures and strong electrical fields as well.

2.7.3 Mechanical configurations

There is a variety of mechanical configurations available to measure acceleration from a piezoelectric material. Depending on the orientation and shape of the piezoelectric material, three piezoelectric effects can be distinguished. These three effects will be explained in the following subsections along with a few examples of mechanical configurations where they are used.

Shear effect

The shear effect is independent of the size and shape of the piezoelectric element, which minimizes mass loading effects on the test structure. If n elements are connected electrically and mechanically in series, the equation for the charge is as follows.

$$Q_x = 2 \times d_{11} \times F_x \times n \quad (2.9)$$

Where d_{11} is the piezoelectric coefficient, F is the applied force, n is the number of crystal plates and $_x$ denominates the direction of the force. The shear effect is utilized in the Shear Beam configuration as shown in figure 2.3. The preload ring is used to give a preload force so that a rigid linear structure is guaranteed. Since the piezoelectric materials are isolated from the base and housing, thermal-transient and base-bending effects are minimized.

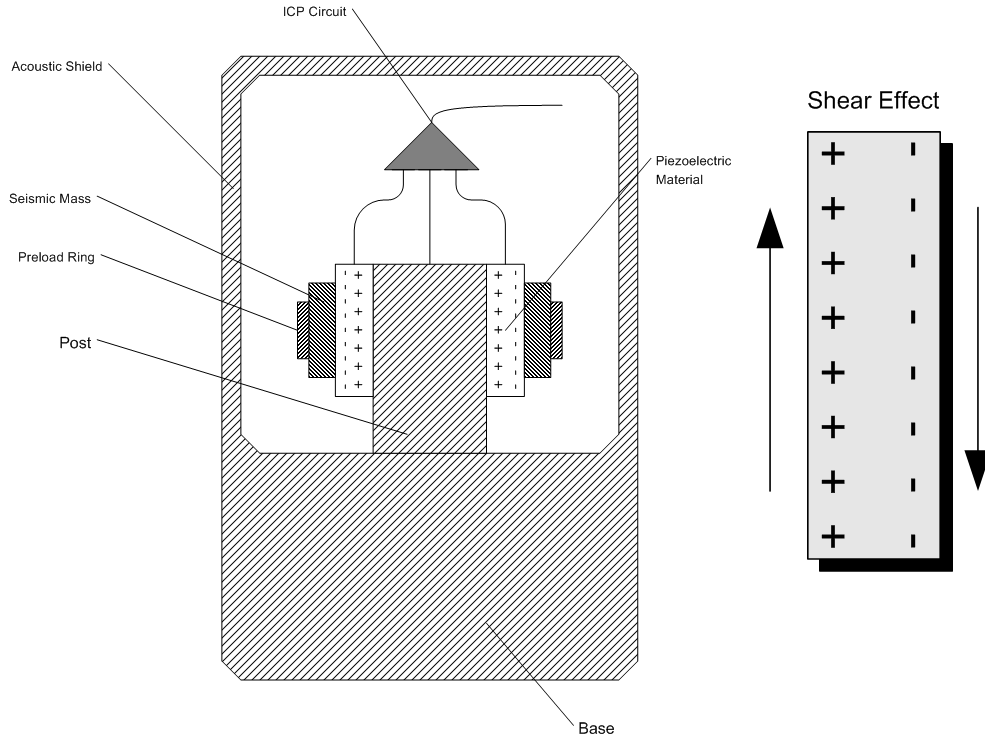


Figure 2.3: Shear Beam configuration and shear effect

Longitudinal effect

The longitudinal effect is independent of the size and shape of the piezoelectric element, i.e. that it is only dependant on the applied force. The charge can be increased by connecting several plates mechanically in series and electrically in parallel. The charge can be expressed as:

$$Q_x = d_{11} \times F_x \times n \quad (2.10)$$

where Q_x , d_{11} , F_x and n are the same as in Equation (2.9). A mechanical configuration which utilizes the longitudinal effect, is the Flexural Beam configuration shown in figure 2.4. This design offers a low profile, light weight, excellent thermal stability and an economical price. It is also insensitive to transverse motion.

Transverse effect

In contrast to the shear and longitudinal effects, the transverse effect is dependant on the geometrical dimensions of the piezoelectric element. The charge produced when the piezoelectric element is subject to a force, can be described as:

$$Q_y = -d_{11} \times F_y \times \frac{b}{a} \quad (2.11)$$

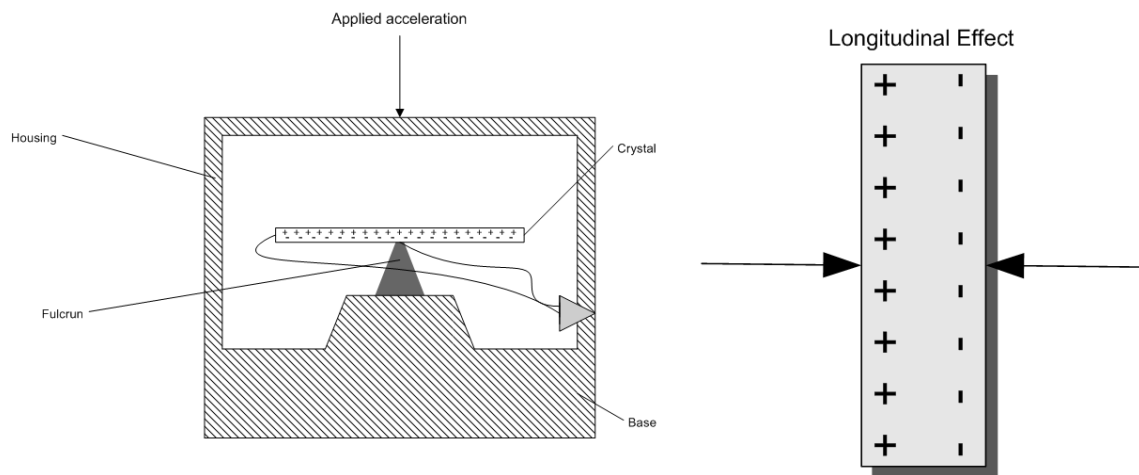


Figure 2.4: Flexural beam configuration and longitudinal effect

where a and b describe the dimensions of the piezoelectric element. This effect is not commonly used in accelerometer design, much because of the dependance of geometrical dimension of the piezoelectric element. An illustration of the effect can be seen in figure 2.5.

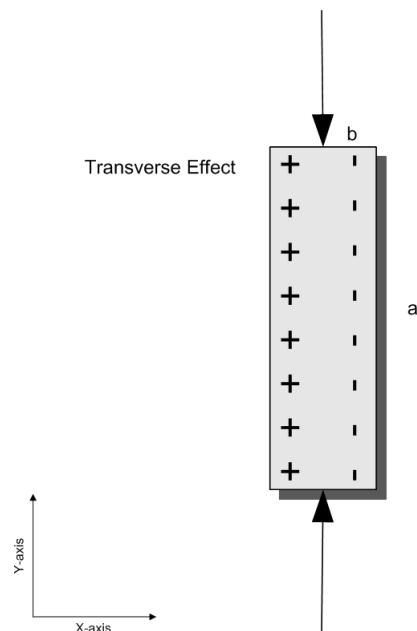


Figure 2.5: Transverse effect

Compression Mode

In addition to the shear and flexural beam configuration, compression mode is also quite common. Compression mode can be divided into three types of design: upright, inverted and isolated.

The *upright compression design* offers high resonant frequencies due to its stiff structure which results in a broad and accurate frequency response range. The design is rugged and capable of withstanding large acceleration values. However, it is also sensitive to the effects from base bending and temperature fluctuations because the piezoelectric crystals are in contact with the base which gives poorer isolation. Due to this sensitivity it is advised to desist from using accelerometers based on this design in thin, sheet-metal structures or in thermally unstable environments.

With *inverted compression design* the piezoelectric crystals are isolated while it retains the good qualities from the upright design. The inverted compression design is often used in reference standard calibration accelerometers.

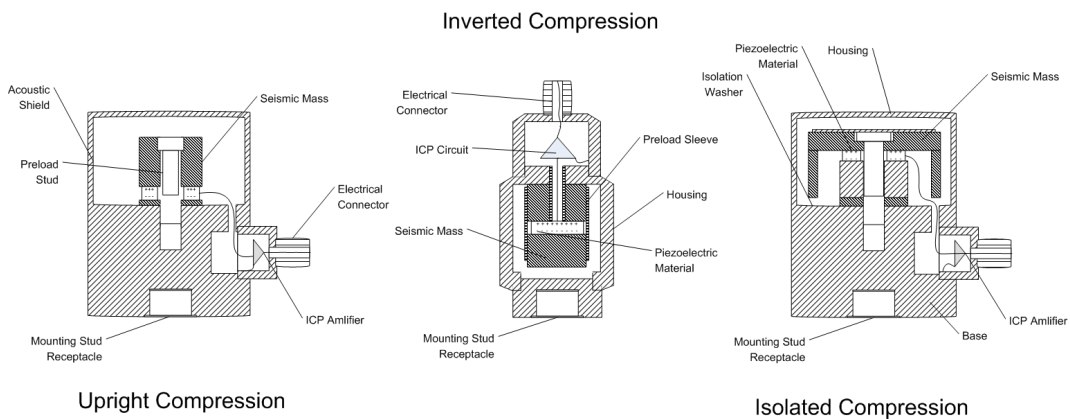


Figure 2.6: The three different compression modes (upright, inverted and isolated)

The *isolated compression design* reduces the errors from base strain and thermal transients by isolating the sensing crystals from the mounting base mechanically. In addition, the seismic mass acts as a thermal insulation barrier. This design allows a stable performance at low frequencies in thermal unstable environments. With other compression design a signal drift may occur under the same conditions. An illustration of the different compression modes can be seen in figure 2.6

2.8 Comparison of accelerometers

There are several manufacturers and the specifications for the different types of accelerometers vary from each one. To illustrate the basic properties of the different accelerometers, a single manufacturer which produces both capacitive, piezoresistive and piezoelectrical accelerometers is chosen. The manufacturer chosen is PCB Piezotronics and the accelerometers

are chosen based on their intended use, i.e. shock and vibration measurement. Because it is possible to mechanically filter out some of the high-frequency vibrations, a few accelerometers with lower frequency and measurement range are examined as well.

Specification (vibration)	Capacitive (650A10)
Sensitivity	1.02 mV/(m/s ²) ($\pm 5\%$)
Measurement range	± 1961 m/s ² pk
Frequency range ($\pm 5\%$)	0 to 800 Hz
Temperature range (Operating)	-40 to +85°C
Specification (no vibration)	Capacitive (3703D1FE50G)
Sensitivity	4.1 mV/(m/s ²) ($\pm 5\%$)
Measurement range	± 490 m/s ² pk
Frequency range ($\pm 5\%$)	0 to 450 Hz
Temperature range (Operating)	-40 to +85°C

Table 2.1: Specifications for capacitive accelerometers

Specification (vibration)	Piezoresistive (3901F3HB2000G)
Sensitivity	0.2 mV/(m/s ²) ($\pm 20\%$)
Measurement range	± 19620 m/s ² pk
Frequency range ($\pm 5\%$)	0 to 5000 Hz
Temperature range (Operating)	-18 to +66°C

Table 2.2: Specifications for a piezoresistive accelerometer

Some specifications for the capacitive, piezoresistive and piezoelectric accelerometers are given in tables 2.1, 2.2 and 2.3 respectively. It can be seen that for the purpose of shock/high frequency measurements, the capacitive accelerometer performs poorly. This is due to the relatively low measurement range of ± 1961 m/s² pk (200 g pk). It does, however, have other properties like true static acceleration measurements and very good sensitivity. If the vibrations can be filtered out, the capacitive accelerometers may be used in a crash test scenario. However, the frequency range is quite low and may not satisfy the recommendations in section 2.2.

The piezoresistive accelerometer has a much greater measurement range which consequently leads to a poorer sensitivity. The frequency range is from 0 to 5000 Hz which is very good, and it has true static load response.

The best accelerometer for high frequency measurements is the piezoelectric. The 352C23 has a measurement range of ± 1000 g and a frequency range up to 10 000 Hz. It lacks the ability to measure static load, but is able to respond to small changes in acceleration (2 Hz). In the extreme cases with g-forces up to 10 000 g's, the model 350B50 can be used. This accelerometer has a built-in 2nd degree low-pass filter which filters out the high-frequency

Specification (vibration)	Piezoelectric (352C23)
Sensitivity	0.5 mV/(m/s ²) ($\pm 20\%$)
Measurement range	± 9810 m/s ² pk
Frequency range ($\pm 5\%$)	2.0 to 10000 Hz
Temperature range (Operating)	-54 to +121°C
Specification (vibration)	Piezoelectric (350B50) ¹
Sensitivity	0.05 mV/(m/s ²) ($\pm 20\%$)
Measurement range	± 98000 m/s ² pk
Frequency range (± 1 dB)	3.0 to 10000 Hz
Temperature range (Operating)	-54 to +121°C
Specification (no vibration)	Piezoelectric (356A12)
Sensitivity	10.2 mV/(m/s ²) ($\pm 20\%$)
Measurement range	± 491 m/s ² pk
Frequency range ($\pm 5\%$)	0.5 to 5000 Hz
Temperature range (Operating)	-54 to +77°C

Table 2.3: Specifications for a piezoelectric accelerometer

vibrations. Because the measurement range is high, the sensitivity will suffer. A small phase lag will also be introduced as a consequence of the low-pass filter. If the vibrations are filtered out in advance, it will still be possible to find a piezoelectric accelerometer that performs very well. As can be seen with model 356A12 in table 2.3, the piezoelectric accelerometer has much better sensitivity than the capacitive and piezoresistive accelerometers.

It seems the best accelerometer type, no matter if the signal is filtered or not before measured, is the piezoelectric accelerometer. It has both better sensitivity, higher frequency range and larger measurement range. For full specification sheets, see Appendix E.

¹The 350B50 accelerometer has a built-in 2nd order low-pass filter.

Chapter 3

Theoretical background

In this chapter the theoretical background will be given. This includes an introduction to the fundamentals of impacts and energy absorption, and theory attended with the angular displacement. A mathematical model of the system will be presented, and a brief introduction to the Kalman filter will be given.

3.1 Impacts and energy absorption

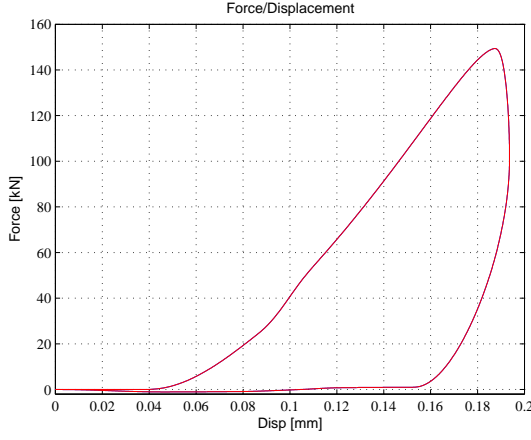
In this section, a brief introduction to the theoretical background of collisions is given. Tipler (1999) and Nyhus (2002) have been used as reference.

A force does work when it acts on an object that moves through a distance, and there is a component of the force along the line of motion. In equation form, this becomes:

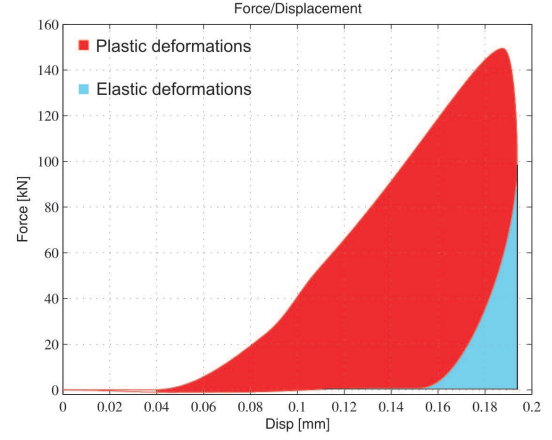
$$W = \int \mathbf{F} d\mathbf{x} \quad (3.1)$$

A load/displacement plot, which has the displacement (\mathbf{x}) along its x-axis and the force (\mathbf{F}) along its y-axis, will give valuable information about the work done during an impact. Work can be divided into dissipative and conservative forces. Conservative forces are forces that do no work over a closed cycle, while dissipative forces will go over to other energy forms like heat, friction and deformations. An example of a load/displacement plot is given in figure 3.1.

It can be seen in the figure how work is performed on the system up to the maximum displacement. The graph after maximum displacement describes the work done by conservative forces. The area inside the graph describes the work done by dissipative forces. For the bumper system case, this means that the area under the upper curve up to maximum displacement will be the total energy absorption of the system. The area inside the graph represents the energy absorption from plastic deformations, while the area under the lower curve represents work done by elastic deformations. Elastic deformation is a deformation of a body in which the applied stress isn't large enough to permanently alter the original dimension of the object after the stress is released. Plastic deformation is when the deformation remains after the stress is released.



(a) An example plot.



(b) Same plot with colours indicating plastic and elastic deformations

Figure 3.1: An example of a Load/Displacement plot.

The three most important mechanical forms of energy are kinetic energy, the potential energy resulting from elastic deformation and an object's positioning in the gravity-field. The equation describing kinetic energy is:

$$E_k = \frac{1}{2}mv^2 \quad (3.2)$$

while the equations describing potential energy are:

$$E_e = \frac{1}{2}kx^2 \quad (3.3)$$

$$E_g = mgh \quad (3.4)$$

associated with elastic deformation and positioning in the gravity field respectively.

When there is an impact where no energy dissipates, there will be a conservation of momentum. This means that the total momentum is equal before and after the impact. Momentum is defined as:

$$\mathbf{p} = m\mathbf{v} \quad (3.5)$$

For an impact between two objects, as illustrated in figure 3.2, the conservation of momentum yields the following equation:

$$m_1\mathbf{v}_{1b} + m_2\mathbf{v}_{2b} = m_1\mathbf{v}_{1a} + m_2\mathbf{v}_{2a} \quad (3.6)$$

During an impact, the two objects will at a point, t_c , have the same velocity \mathbf{v}_c . The momentum in t_c is equal the momentum in equation (3.6) which gives:

$$(m_1 + m_2)\mathbf{v}_c = m_1\mathbf{v}_{1b} + m_2\mathbf{v}_{2b} = m_1\mathbf{v}_{1a} + m_2\mathbf{v}_{2a} \quad (3.7)$$

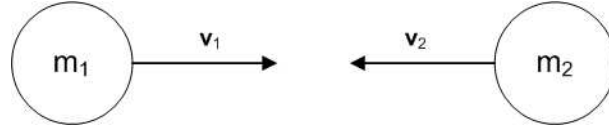


Figure 3.2: A simple impact with two objects.

The kinetic energy of the system before, during and after impact becomes as follows:

$$E_{k,b} = \frac{1}{2}(m_1 \mathbf{v}_{1b}^2 + m_2 \mathbf{v}_{2b}^2) \quad (3.8)$$

$$E_{k,c} = \frac{1}{2}(m_1 + m_2) \mathbf{v}_c^2 \quad (3.9)$$

$$E_{k,a} = \frac{1}{2}(m_1 \mathbf{v}_{1a}^2 + m_2 \mathbf{v}_{2a}^2) \quad (3.10)$$

If the impact is completely elastic, $E_{k,b}$, $E_{k,c}$ and $E_{k,a}$ will be equal. However, if the impact is plastic, that will not be the case. To help us describing how elastic or plastic an impact is, a coefficient of restitution is used. This coefficient is defined as

$$\epsilon^2 = \frac{E_{k,a} - E_{k,c}}{E_{k,b} - E_{k,c}} \leq 1 \quad (3.11)$$

If $\epsilon = 1$ it means that the impact is elastic and all the energy is conserved. The forces acting on the objects are strictly conservative in this case. If $\epsilon = 0$, the collision is perfectly plastic and the forces acting upon the objects are dissipative.

3.2 Accelerations tied to angular displacement

Consider a particle in a rigid body, and let r_i be the length from the rotation point. As the rigid body rotates with an angle θ , the particle moves through a circular arc of length

$$s_i = r_i |\theta| \quad (3.12)$$

where θ is measured in radians. The angle θ is the same for every particle in the rigid body, and is called angular displacement. The time rate of change of the angle, $\dot{\theta}$, is the same for every particle as well, and is called the angular velocity ω . The tangential velocity of a particle in the rigid body becomes:

$$v_{it} = r_i \omega \quad (3.13)$$

The time rate of change of angular velocity is called the angular acceleration α :

$$\alpha = \dot{\omega} = \ddot{\theta} \quad (3.14)$$

The tangential acceleration of a particle in the rigid body is

$$a_{it} = r_i \dot{\omega} = r_i \alpha \quad (3.15)$$

Each particle also has a radial acceleration, the centripetal acceleration, which points inward along the radial line.

$$a_{ic} = \frac{v_{it}^2}{r_i} = \frac{(r_i\omega)^2}{r_i} = r_i\omega^2 \quad (3.16)$$

In figure 3.3 the tangential and radial accelerations are shown together with the axes of the accelerometer.

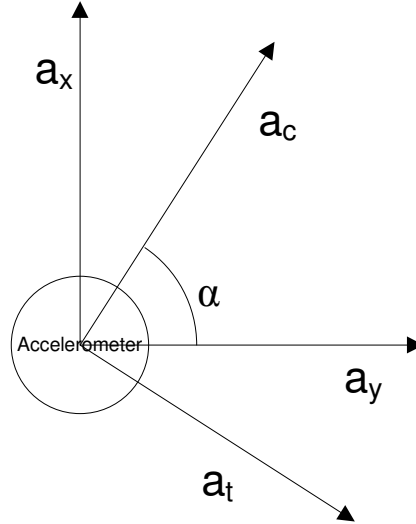


Figure 3.3: The two accelerations acting upon the accelerometer showed together with the accelerometer's axes.

3.3 Computing the rotation

The way the tests currently are performed and the data processed, gives no way of knowing if the test vehicle has rotated and ,if so, how much. If the accelerations can be measured precisely, it should be possible to calculate the test vehicle's rotation.

Since the current test procedures and data processing only use the acceleration in x-direction when performing calculations, there are two new movements that can be registered when utilizing the y-direction as well; the sideways drift and the rotation. The sideways drift will manifest itself as an acceleration in y-direction with the same force on all three accelerometers. The integral of this acceleration should be zero as the test vehicle will both start and end with zero velocity in y-direction. The rotation, however, will differ depending on the point of observation and where the rotation takes place, i.e. the different accelerometers will experience the rotation in different ways. As derived in section 3.2, the accelerometers will experience two acceleration forces as a result of the rotation. Assuming that the rotation takes place in point P in figure 3.4, the equations for the resulting accelerations becomes as follows:

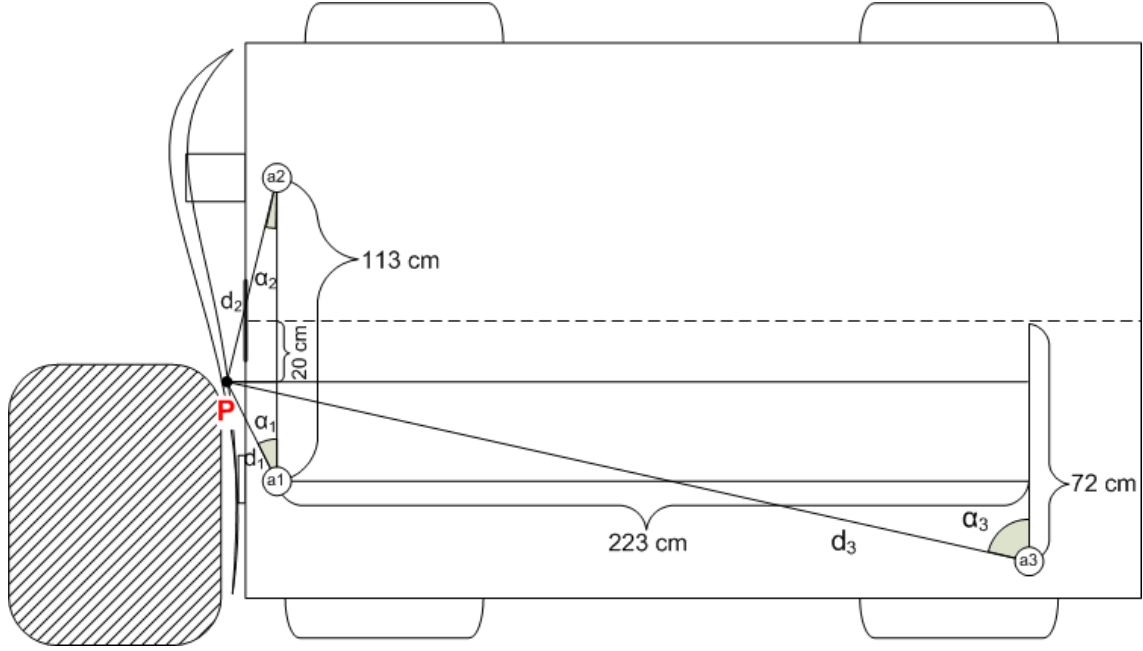


Figure 3.4: The parameters needed to calculate the rotation angle.

$$a1_x = -\dot{\omega} \cdot d_1 \cos \alpha_1 + \omega^2 \cdot d_1 \sin \alpha_1 \quad (3.17)$$

$$a1_y = \dot{\omega} \cdot d_1 \sin \alpha_1 + \omega^2 \cdot d_1 \cos \alpha_1 \quad (3.18)$$

$$a2_x = \dot{\omega} \cdot d_2 \cos \alpha_2 + \omega^2 \cdot d_2 \sin \alpha_2 \quad (3.19)$$

$$a2_y = \dot{\omega} \cdot d_2 \sin \alpha_2 - \omega^2 \cdot d_2 \cos \alpha_2 \quad (3.20)$$

$$a3_x = -\dot{\omega} \cdot d_3 \cos \alpha_3 + \omega^2 \cdot d_3 \sin \alpha_3 \quad (3.21)$$

$$a3_y = \dot{\omega} \cdot d_3 \sin \alpha_3 + \omega^2 \cdot d_3 \cos \alpha_3 \quad (3.22)$$

where a_x and a_y are the measured accelerations, $\dot{\omega}$ is the rotational acceleration, ω is the angular velocity and d is the distance from the rotation point P. Since the accelerometers measure large values in x-direction due to the crash, the most reliable source to compute $\dot{\omega}$ from, will probably be $a3_y$, i.e. equation (3.22).

The sideways drift can be found by looking at the readings of $a1_y$ and $a2_y$ and subtracting the acceleration components resulting from the rotation. The equations for finding the sideways drift is:

$$a_d = a1_y - \dot{\omega} \cdot d_1 \sin \alpha_1 - \omega^2 \cdot d_1 \cos \alpha_1 \quad (3.23)$$

$$a_d = a2_y - \dot{\omega} \cdot d_2 \sin \alpha_2 + \omega^2 \cdot d_2 \cos \alpha_2 \quad (3.24)$$

where only one of the equations is necessary to perform the calculation.

3.4 Mathematical modeling

In order to get a clearly set out model of the system, it is convenient to organize the system equations in matrix-form. In addition to the equations obtained in the previous chapter, the equations describing the relationship between position, velocity ($\dot{x} = v$) and acceleration ($\dot{v} = a$) are used to get a full description of the system. The resulting mathematical model becomes

$$\begin{bmatrix} \dot{\mathbf{x}} \\ \dot{\mathbf{v}} \\ \dot{\theta} \\ \dot{\omega} \\ \dot{\mathbf{a}} \\ \dot{\mathbf{b}} \end{bmatrix} = \begin{bmatrix} \mathbf{v} \\ \mathbf{a} - \mathbf{b} - \dot{\omega} \cdot \boldsymbol{\omega}_{konst} - \omega^2 \cdot \boldsymbol{\omega}_{konstC} \\ \omega \\ \frac{a_{3y} - a_d - d_3 \cos \alpha_3 \omega^2}{d_3 \sin \alpha_3} \\ \mathbf{w} \\ -T^{-1} \mathbf{b} + \mathbf{w} \end{bmatrix} \quad (3.25)$$

$$\boldsymbol{\omega}_{konst} = \begin{bmatrix} -d_1 \cos \alpha_1 \\ d_1 \sin \alpha_1 \\ d_2 \cos \alpha_2 \\ d_2 \sin \alpha_2 \\ -d_3 \cos \alpha_3 \\ d_3 \sin \alpha_3 \end{bmatrix}, \quad \boldsymbol{\omega}_{konstC} = \begin{bmatrix} d_1 \sin \alpha_1 \\ d_1 \cos \alpha_1 \\ d_2 \sin \alpha_2 \\ -d_2 \cos \alpha_2 \\ d_3 \sin \alpha_3 \\ d_3 \cos \alpha_3 \end{bmatrix} \quad (3.26)$$

where \mathbf{x} is the position in two dimensions, \mathbf{v} is the velocity in the same two dimensions, \mathbf{a} is the acceleration readings from the accelerometers and \mathbf{b} is a bias on the readings. $\dot{\omega}$ is found by rearranging equation (3.22). Since there are three accelerometers which measure in both x- and y-direction, \mathbf{x} , \mathbf{v} , \mathbf{a} and \mathbf{b} consists of six elements each. \mathbf{w} , θ and ω represent the white noise, angular displacement and angular velocity, respectively. The acceleration is modeled as a random walk and the bias is modeled as a 1st-order Markov model (Fossen 2002). Because there is a nonlinear element in the equation for $\dot{\mathbf{v}}$, the system needs to be linearized. Linearization around the working point $\omega = 0$ yields the following mathematical model:

$$\begin{bmatrix} \dot{\mathbf{x}} \\ \dot{\mathbf{v}} \\ \dot{\theta} \\ \dot{\omega} \\ \dot{\mathbf{a}} \\ \dot{\mathbf{b}} \end{bmatrix} = \begin{bmatrix} \mathbf{v} - \omega \cdot \boldsymbol{\omega}_{konst} \\ \mathbf{a} - \mathbf{b} \\ \omega \\ \frac{a_{3y} - a_d}{d_3 \sin \alpha_3} \\ \mathbf{w} \\ -T^{-1} \mathbf{b} + \mathbf{w} \end{bmatrix} \quad (3.27)$$

where $a_d = a_{1y} - \dot{\omega} \cdot d_1 \sin \alpha_1$ because of the linearization. \mathbf{v} will have component due to the rotation, but this can be subtracted later by using the calculated value of ω . Expressing the system on state form, we get

$$\dot{\mathbf{x}} = A\mathbf{x} + B\mathbf{u} + E\mathbf{w} \quad (3.28)$$

$$\mathbf{y} = C^T \mathbf{x} \quad (3.29)$$

where

$$A = \begin{bmatrix} \mathbf{0} & \mathbf{1} & 0 & -\boldsymbol{\omega}_{konst} & \mathbf{0} & \mathbf{0} \\ \mathbf{0} & \mathbf{0} & \vdots & 0 & \mathbf{1} & -\mathbf{1} \\ 0 & \dots & 0 & 1 & 0 \dots 0 & 0 \dots 0 \\ 0 & \dots & 0 & 0 & \mathbf{a}_\omega & 0 \dots 0 \\ \mathbf{0} & \mathbf{0} & \vdots & \vdots & \mathbf{0} & \mathbf{0} \\ \mathbf{0} & \mathbf{0} & 0 & 0 & \mathbf{0} & -\mathbf{T}^{-1} \end{bmatrix}, \quad \mathbf{a}_\omega = \begin{bmatrix} 0 \\ -\frac{1}{d_3 \cdot \sin \alpha_3} \\ 0 \\ 0 \\ 0 \\ \frac{1}{d_3 \cdot \sin \alpha_3} \end{bmatrix}^T \quad (3.30)$$

$$B = \begin{bmatrix} \mathbf{0} \\ \mathbf{0} \\ \mathbf{0} \\ \mathbf{0} \\ \mathbf{0} \\ \mathbf{0} \end{bmatrix}, \quad E = \begin{bmatrix} \mathbf{0} & \mathbf{0} & 0 & 0 & \mathbf{0} & \mathbf{0} \\ \mathbf{0} & \mathbf{0} & \vdots & \vdots & \mathbf{0} & \mathbf{0} \\ 0 \dots 0 & 0 \dots 0 \\ 0 \dots 0 & 0 \dots 0 \\ \mathbf{0} & \mathbf{0} & \vdots & \vdots & \mathbf{1} & \mathbf{0} \\ \mathbf{0} & \mathbf{0} & 0 & 0 & \mathbf{0} & \mathbf{1} \end{bmatrix} \quad (3.31)$$

and C^T describes which measurements are available.

3.5 The Kalman Filter

Because there is a redundancy in measurements, it can be a good idea to merge all these measurements in a Kalman filter and get an improved and more accurate reading. Kalman filtering can be described as an optimal state estimation in sense of minimum variance which allows the user to estimate the state \mathbf{x} of a dynamic system from a noise contaminated input-output pair (\mathbf{u}, \mathbf{y}) . The different sources can be weighted according to their expected variance and accuracy. The interested reader may consult Fossen (2002), Welch & Bishop (2004) and Farrell & Barth (1998) for more detailed information on the Kalman filter.

The Kalman filter will filter out the noise and give an estimate of the rotation angle originating from the offset impact. The quality of this estimate will be dependant on the quality of the readings. In order to utilize the Kalman filter, the system needs to be presented in state form as shown in equations (3.32) and (3.33).

$$\dot{\mathbf{x}} = \mathbf{A}\mathbf{x} + \mathbf{B}\mathbf{u} + \mathbf{E}\mathbf{w} \quad (3.32)$$

$$\mathbf{y} = \mathbf{H}\mathbf{x} + \mathbf{v} \quad (3.33)$$

The vector \mathbf{x} is the state vector, \mathbf{y} is the measurement vector, \mathbf{u} is the input, and \mathbf{w} and \mathbf{v} are zero mean Gaussian white noise processes. The matrices \mathbf{A} , \mathbf{B} and \mathbf{E} describes the system while \mathbf{H} is the measurement matrix. The Kalman filter equations are as follows:

$$\dot{\hat{\mathbf{x}}}(t) = \mathbf{A}(t)\hat{\mathbf{x}}(t) + \mathbf{B}(t)\mathbf{u}(t) + \mathbf{K}(t)[\mathbf{y}(t) - \mathbf{H}(t)\hat{\mathbf{x}}(t)] \quad (3.34)$$

$$\mathbf{K}(t) = \mathbf{P}(t)\mathbf{H}^T(t)\mathbf{R}^{-1}(t) \quad (3.35)$$

$$\dot{\mathbf{P}}(t) = \mathbf{A}(t)\mathbf{P}(t) + \mathbf{P}(t)\mathbf{A}^T(t) + \mathbf{E}(t)\mathbf{Q}(t)\mathbf{E}^T(t) \quad (3.36)$$

$$- \mathbf{P}(t)\mathbf{H}^T(t)\mathbf{R}^{-1}(t)\mathbf{P}(t), \mathbf{P}(t) = \mathbf{P}^T(t) > 0 \quad (3.37)$$

where $\mathbf{K}(t)$ is the Kalman gain matrix, $\dot{\hat{\mathbf{x}}}(t)$ is the state estimate propagation and $\dot{\mathbf{P}}(t)$ is the error covariance propagation. The matrices $\mathbf{R}(t) = \mathbf{R}^T(t) > 0$ and $\mathbf{Q}(t) = \mathbf{Q}^T(t) > 0$ are design matrices where $\mathbf{R}(t)$ represents the covariance in the measurements and $\mathbf{Q}(t)$ represents the process noise covariance.

$\mathbf{R}(t)$ can be found by computing the covariance of the measurements when the output is supposed to be zero, while $\mathbf{Q}(t)$ usually is found by trial and error.

Chapter 4

The Crash Test Lane

4.1 Test facility

The test facility is located at Hydro's premises in Raufoss, Norway. The components used in the barrier- and AZT-tests are presented in this section.

4.1.1 Barrier

The barrier is a concrete block with a steel-plate mounted on it. It is possible to attach different steel-objects for different tests, like the AZT-test where a barrier which covers 40% of the width is needed. As can be seen in figure 4.1(a) and 4.1(b), there are two range finders; one above and one below the barrier. The range finders measure the distance to the test vehicle during impact. A more thorough description of the range finders is given in section 4.2.2.



(a) Normal barrier.



(b) Pole barrier.

Figure 4.1: The barrier.

4.1.2 Test vehicle

In order to perform the different tests, a test vehicle, onto which the bumper system is mounted, is needed. Because we want as little energy absorption as possible in the car itself, the test vehicle is much stiffer than an ordinary car. This way, almost all the energy will be absorbed in the bumper system. Without any load, the test vehicle ways in at about 1000 kg, but it is possible to increase this to about 2000 kg by adding weight.

The test vehicle has three load-cells mounted behind both of the two crash boxes to measure the force acting on it. In addition it has three accelerometers which measure the acceleration in x- and y-direction. One of the accelerometers even measure the acceleration in z-direction. The location of the accelerometers can be seen in figure 4.2(c). The accelerometer in the rear of the test vehicle was temporary mounted on the far left during the test-series studied in this thesis. It will, however, be permanently mounted along the symmetry-axis in the future.

4.1.3 The winch

The current winch is a hydraulic one, capable of achieving impact speeds close to 20 km/h with a test vehicle of 2 tons. This winch will soon be replaced by a new electric winch which is capable of achieving velocities greater than 30 km/h. The electric winch is also more accurate with respect to producing the desired impact speed.

4.1.4 High-speed cameraes

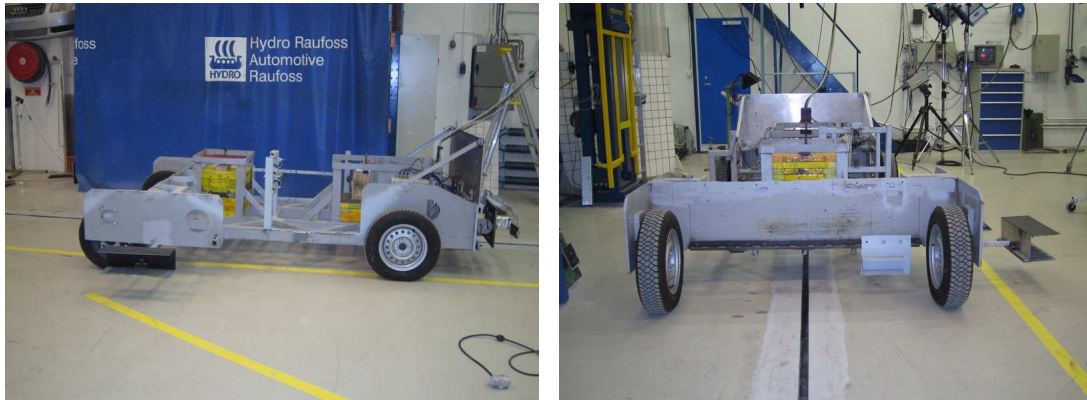
In order to capture the impact on film, two high-speed cameraes are used. One camera films top-down while the other films from the side. Usually the cameraes take 1000 pictures per minute, but it is also possible to take 2000 pictures per minute if this is desirable.

4.2 The instruments

In this section, a brief introduction to the different measuring instruments used in the AZT and barrier test will be given.

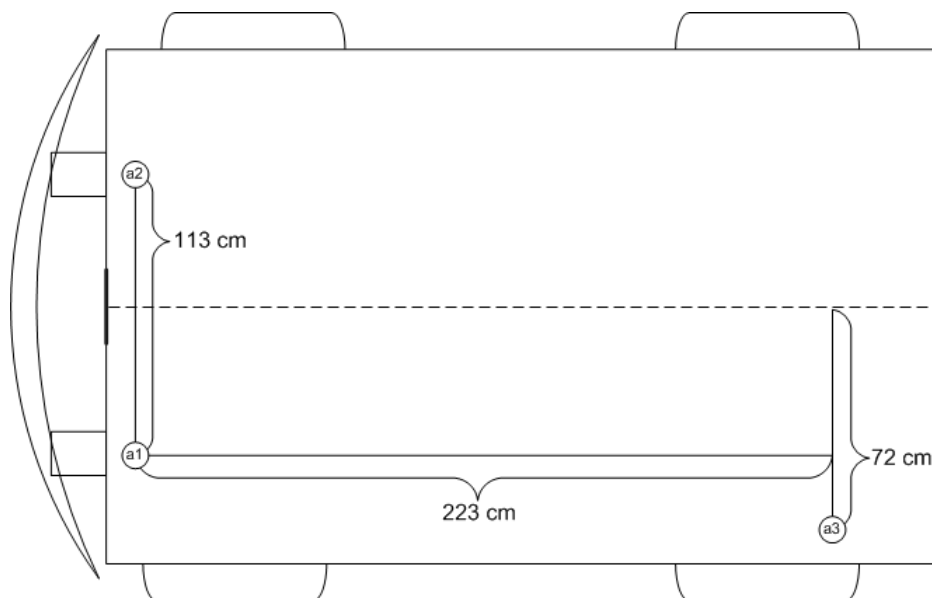
4.2.1 Speed measurements

The speed is measured by using a fixed laser beam on a grating attached to the moving vehicle. Each time a bar on the grating passes over the laser beam, a pulse is generated. When the distance between each bar on the grating is known along with the width of the bar, it is possible to calculate the impact speed. As can be seen in figure 4.3(b), there are two lasers on the device. The first laser merely acts as a trigger which tells the computer to start sampling data and the winch to stop pulling, while the second measures the velocity.



(a) From the side.

(b) From the back.



(c) Location of the accelerometers.

Figure 4.2: The test vehicle.

4.2.2 The laser (range finder)

The instrument used to measure the distance from the barrier to the test vehicle is a ODS 750 produced by DSE ApS. The instrument consists of a laser and a position detector. A focused laser beam forms a spot on the surface of the measuring object and the image of the spot is detected by the position detector. By utilizing the triangulation principle, the ODS is able to compute the distance to the object. The ODS 750 can work on either 500 Hz or 1000 Hz and has a measuring range between 400 - 1100 mm. The margin of error is ± 0.5 mm.

Before each test, the test vehicle is pulled up to the barrier so that the bumper touches

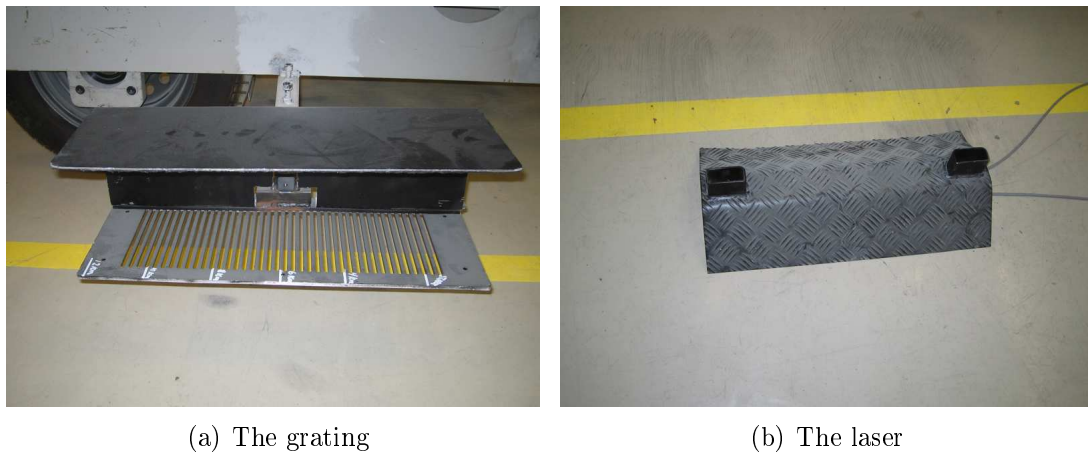


Figure 4.3: Speed measurement instruments

the barrier. The distance is then set to be zero before the test vehicle is pulled back to ready position. The distance the laser measures during the impact acts as a measurement of how much the bumper system is compressed.

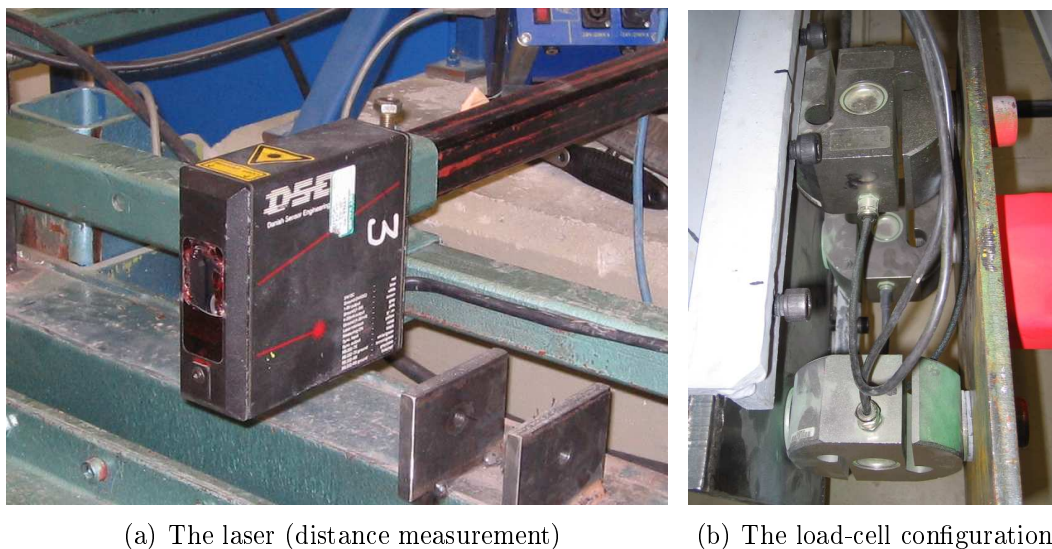


Figure 4.4: The laser and the load-cell configuration.

4.2.3 Load-cells

To measure the load acting on the car from the bumper system, three load-cells are mounted behind each crash box. The sum of all the six load-cells yields the total load acting on the test vehicle. The load-cells used are U4200 produced by Maywood Instruments which have

a measurement range of 100 kN each. They have a accuracy of ± 1 kN, have an overload capacity of 150% and a maximum sideload of 50%. The load-cells are mounted in such a way that the sideload is minimized (see figure 4.4(b)).

4.2.4 Acceleration

There are two types of accelerometers used; one type on the test vehicle and a different type on the barrier.

On the barrier there is only one accelerometer which is supposed to measure the barrier's acceleration in x-direction. The barrier will not actually move, but it will vibrate and that is what the accelerometer measures. The accelerometer has the model number 625B01 and is provided by IMI Sensors. It is a ceramic piezoelectric accelerometer with shear sensing geometry. The measurement range is ± 490 m/s² (± 50 g) and it can withstand shocks up to 49050 m/s² (5000 g).

On the test vehicle there are three accelerometers of the type 629A31, also provided by IMI Sensors. These are triaxial which means that they can measure accelerations in both x-, y- and z-direction. However, only one accelerometer measures acceleration in z-direction due to the amplifier only having eight channels. Like the 625B01, the 629A31 is also a ceramic piezoelectric accelerometer with shear sensing geometry. The measurement range is ± 490 m/s² (± 50 g) and the shock limit is 49050 m/s² (5000 g).

4.3 The test procedures

In this section the test procedures are briefly explained. Emphasis is laid on the description of the AZT-test since the testseries data used for analysis in Chapter 5 are collected from this test.

4.3.1 AZT test

The Allianz Zentrum für Technik (AZT) developed this test in the early 1980's and it has been adopted by the Research Council for Automobile Repairs (RCAR) as a standard for conducting low-speed crash tests. RCAR is an international organization that works towards reducing insurance costs by improving automotive damageability, reparability, safety and security (Research Council for Automobile Repairs 2002). The AZT test can be performed on both front and rear bumpers.

The frontal test is performed by letting the test vehicle crash into a barrier which is offset in such a way that it covers 40% of the test vehicle's width (see figure 4.5(a)). The speed at impact should be $15.0 \pm 1.0 - 0.0$ km/h.

In the rear collision test, the test vehicle stands still while a mobile barrier rams into it. As with the frontal test, the barrier is offset so that it covers 40% of the test vehicle's width. The mobile barrier has a mass of 1000 kg. An illustration of this test is given in figure 4.5(b)

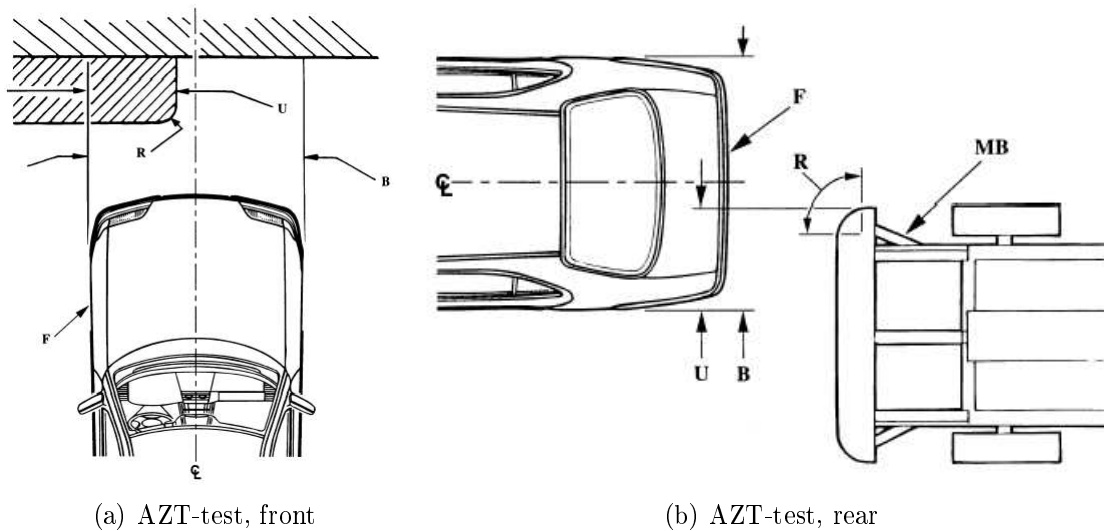


Figure 4.5: **MB** = Mobile barrier, **U** = Offset 40%, **B** = Overall width of vehicle, **R** = 150mm constant radius, **F** = Test vehicle (Research Council for Automobile Repairs 1999)

4.3.2 IIHS-test

The IIHS pole test is conducted with a nominal impact speed of about 8 km/s (5 mi/s). The pole test is intended to assess how well the bumper system protects against damage from a narrow object. The test vehicle's longitudinal centerline will, normally, be aligned with the test-pole in these tests. More information and specifications about this test can be found in Insurance Institute for Highway Safety (2002). Pole tests at higher impact speeds can also be carried out on demand from the car manufacturer.

4.3.3 Barrier test

In the barrier test, the test vehicle is rammed into a stiff barrier at a desired speed, usually around 16 km/h. The test vehicle is pulled towards the barrier using a wire. A laser sensor makes sure that the pull is disconnected before impact. This test is performed in order to observe the bumper system during impact as well as measuring the forces at work on the bumper system.

4.3.4 The pendulum test

The pendulum test is done by letting a pendulum of a specific weight hit the bumper system at a desired speed and location on the bumper. The point of impact can be adjusted in vertical direction by adjusting the pendulum up or down. Measured values during a pendulum test is the distance between the pendulum and the test vehicle, the speed of the pendulum and the contact force between the pendulum and the vehicle.

Chapter 5

Analysis

In this chapter, the results from the tests will be examined and comments will be given. There won't be made any attempts to correct the errors at this stage in the thesis, since the emphasis is on mapping the sources of error and determining their impact on the readings obtained.

5.1 Speed measuring unit

The speed measuring unit consists of a laser and a grating. The grating is attached to the test vehicle while the laser is standing on the ground. Each time a bar on the grating intersects the laser beam, a pulse is generated. Knowing the width of the bars in the grating and the distance between each bar it is possible to calculate the speed.

The most obvious source of error in this case is whether the actual bar width is the same as the one the calculations are carried out with. The algorithm used to calculate the speed, counts the number of sample periods between the pulses as long as the speed is nearly constant. The speed obtained with this algorithm, is the impact speed of the vehicle. The pulses generated can be seen in figure 5.1. If the same algorithm is used only on the pulses generated after the impact, it will produce the velocity of the vehicle as it rolls back from the barrier.

5.2 The lasers (range finders)

There are two range finders mounted on the barrier. One is mounted on the top of the barrier and the other stands on the ground. A picture showing the arrangement can be seen in figure 5.2. The range finders are reset to zero at the point where the bumper system meets the barrier.

There are two ways to interpret the results from the range finders. The first interpretation is that it is the test vehicle's position in x-direction that is being measured. The other interpretation is that the maximum in figure 5.3 shows how many millimeters the bumper system has been compressed.

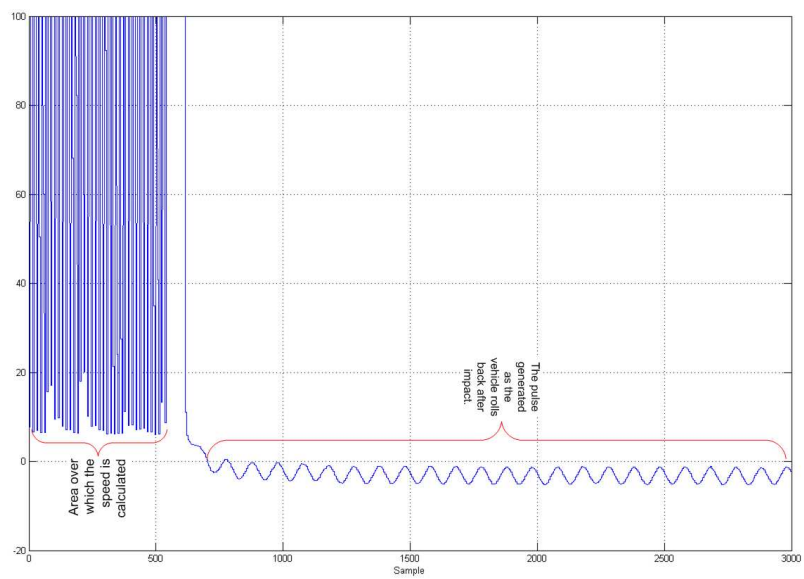


Figure 5.1: The pulse generated by the speed measuring unit(scaled).

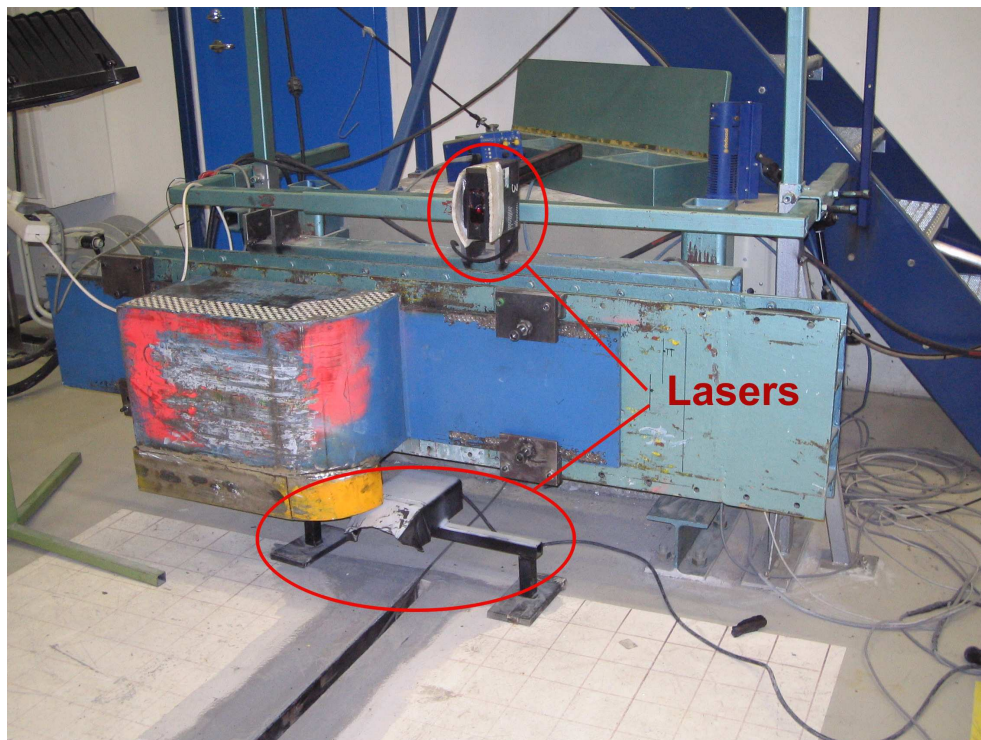


Figure 5.2: The range finder arrangement.

The two range finders should ideally yield the same result, but this is not the case as can be seen in figure 5.3. It can also be noticed that one of the range finders very often has a upturn at about 1400 samples.

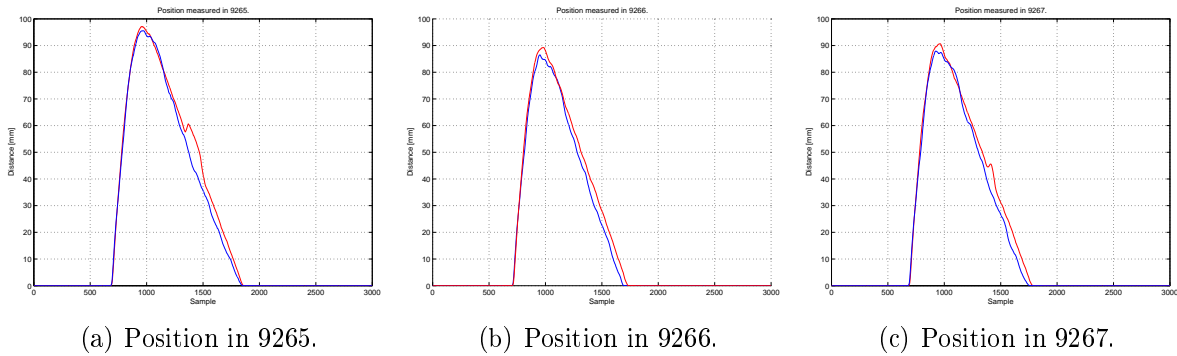


Figure 5.3: The test vehicle's position in x-direction during impact.

The reason for the deviation in the two measurements can be explained by consideration of their placing. The range finder which measures the largest values is mounted on top of the barrier, while the one producing the slightly lower and smoother readings, is the one on the ground. As explained earlier in chapter 6.1.2, the test vehicle will rotate slightly when performing the AZT-test. The upturn experienced in the upper range finder can be explained by considering this rotation. As the test vehicle rotates, it will move closer to the upper range finder which is placed closer to the center of the vehicle than the lower. This will result in the upturn observed in figure 5.3. In addition it can be seen from the high-speed cameras that the plate which the lasers are aimed at, vibrate quite a lot during impact. These vibration are much more violent at the top of the plate than on the lower part. This means that the upper range finder has much more vibration noise than the lower one.

Taking into account all these sources of error, it can be concluded that the lower range finder probably yields the most accurate result, but the upper one may be able to help indicate whether there is a rotation. However, since there is no routine on where the upper laser is placed, it is difficult to say anything on how large the rotation is.

5.3 Load-cells

There are three load-cells behind each crash box. They measure the forces which acts upon the test vehicle during impact. The load-cells filter their signals before they are sent to the computer. Because of this filtering, there will be a time delay in the region of a few samples on the signals from the load-cells. The load-cells are accurate down to ± 1 kN which gives a total insecurity of ± 6 kN.

It can be seen from figure 5.4 that the load-cells don't settle at zero after impact, but rather seem to have an approximately constant value. This is due to distortions in the bumper system which act upon the sensors with a constant force after impact. This is

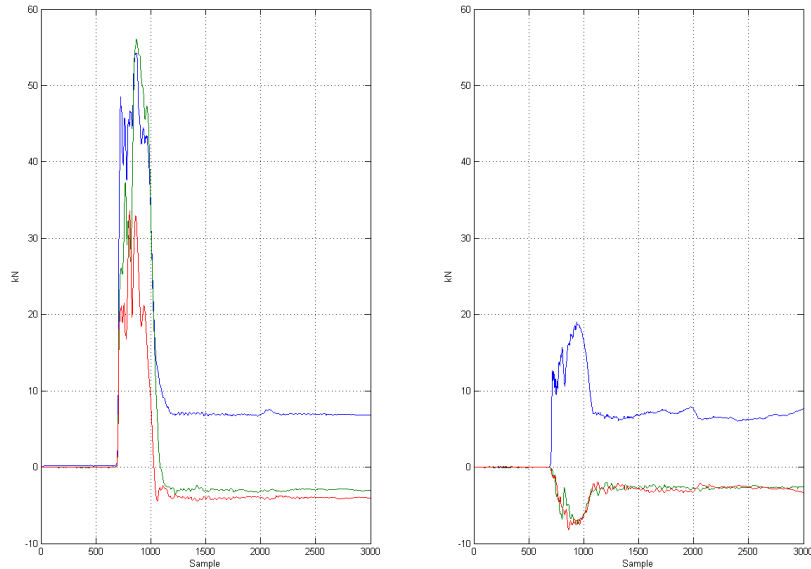


Figure 5.4: Measurements from the individual load-cells. Left side load-cells on the left and right side load-cells on the right.

supported by an observation in figure 5.5 where it can be seen that the total force on the three sensors behind each crash-box is close to zero, which is as suspected when there no longer is an external force acting upon the bumper system.

The forces measured on the right side of the test vehicle are much smaller than the ones on the left side. The reason for this is quite obvious since the crash test involves an offset barrier.

5.4 Accelerometers

The readings from accelerometer 1, 2 and 3 are given in figures 5.6, 5.7 and 5.8 respectively. Accelerometer 1 measures acceleration in z-direction in addition to x- and y-direction. It is clear that there is a lot of noise on the signal from the accelerometers, and quite often the accelerometers measure the maximum value of 50 g's in both x- and y-direction, which is clearly erroneous. The accelerometers also yield readings with a mean value different from zero after the test vehicle is clear of the barrier. Except from a small positive acceleration in x-direction due to friction in the wheels, the mean value should be zero after impact. There would still be vibrations in the vehicle.

In figure 5.9 the mean values of the measured values before, during and after impact are given. Before impact the mean value of the measured acceleration in x-direction is close to zero, while the measurements in y-direction clearly have a bias. This bias is even larger with accelerometer 1 (about 1 g) than with accelerometer 3 which is used in figure 5.9.

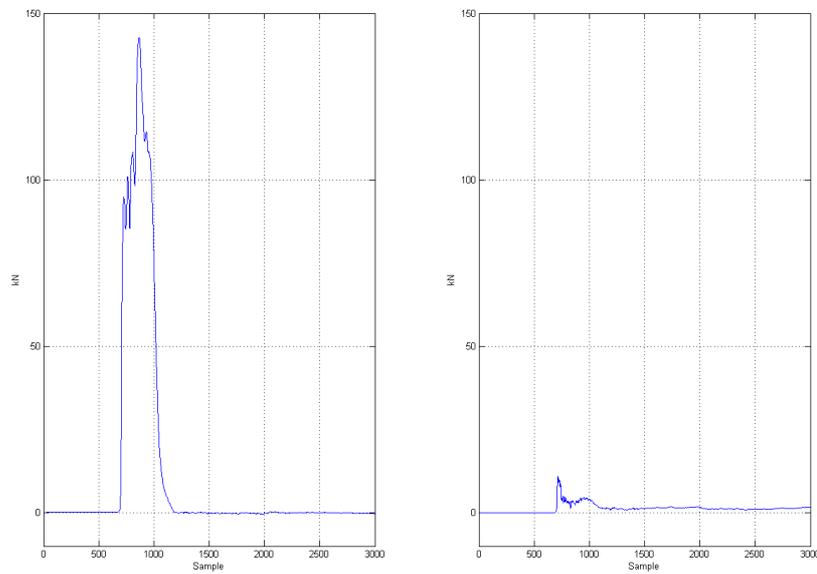


Figure 5.5: The total load on the left and right side of the bumper system.

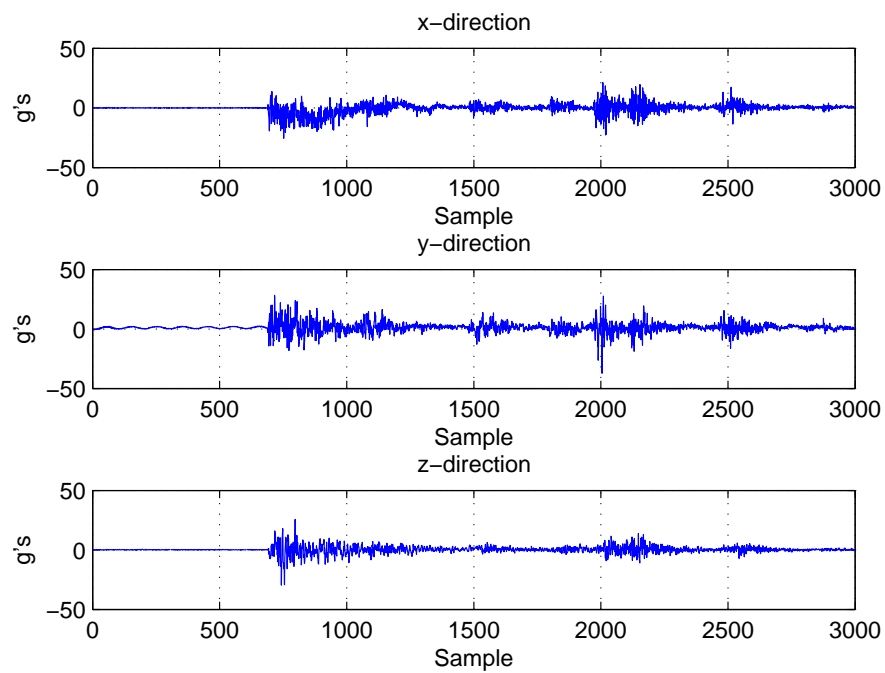


Figure 5.6: The readings from accelerometer 1.

The high-frequency noise is due to vibrations in the test vehicle and measurement noise. The vibrations also have a very high frequency which may introduce errors in the accelerometer readings. It is likely that the post-impact accelerations are because of malfunctions in the instruments due to the high g-forces or the high frequency vibrations during impact. The bias experienced in y-direction may be a result of incorrect mounting and calibration of the accelerometers.

Accelerometer 1 also has a sine wave-form output in y-direction before impact. The reason for this behavior may be the fact that the pull from the winch isn't on the center of the test vehicle, but rather with an off-set of 20 cm. This may lead to some vibrations in the vehicle which result in the behavior observed. The reason for the offset pull, is that it is convenient in order to obtain the 40% impact needed in the AZT-test described earlier.

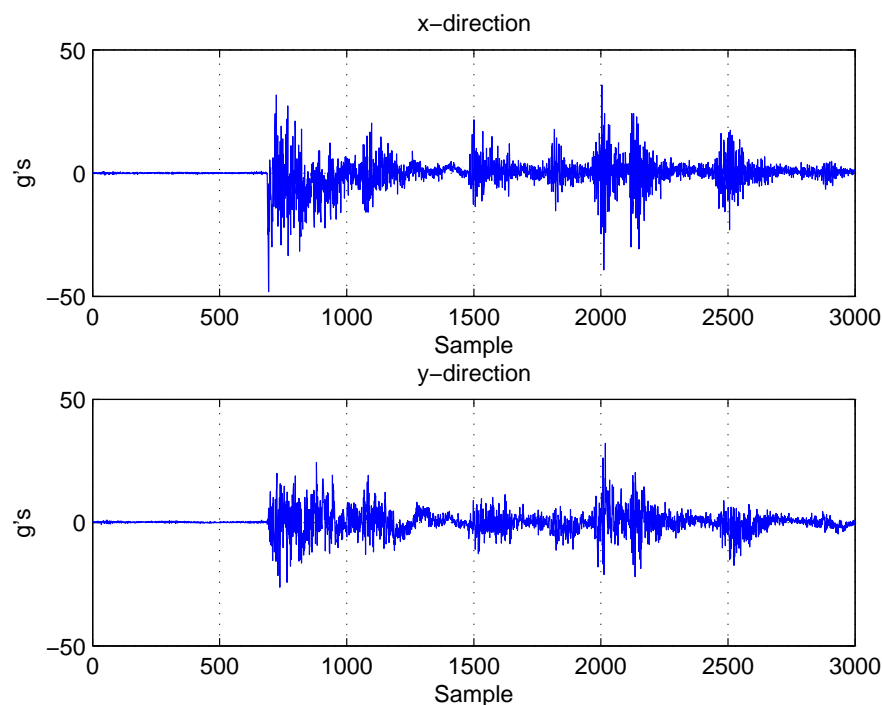


Figure 5.7: The readings from accelerometer 2.

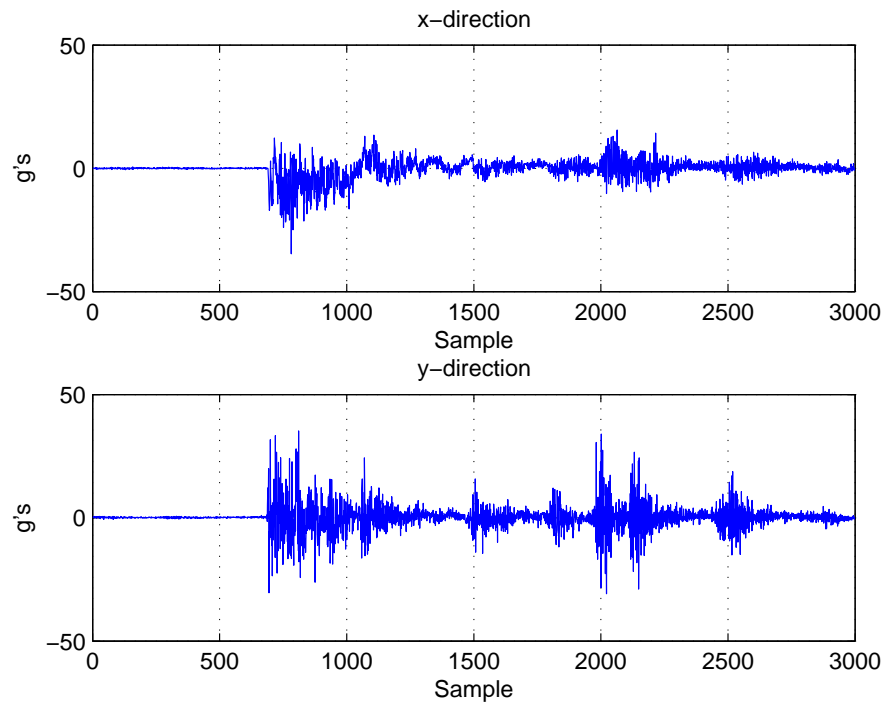


Figure 5.8: The readings from accelerometer 3.

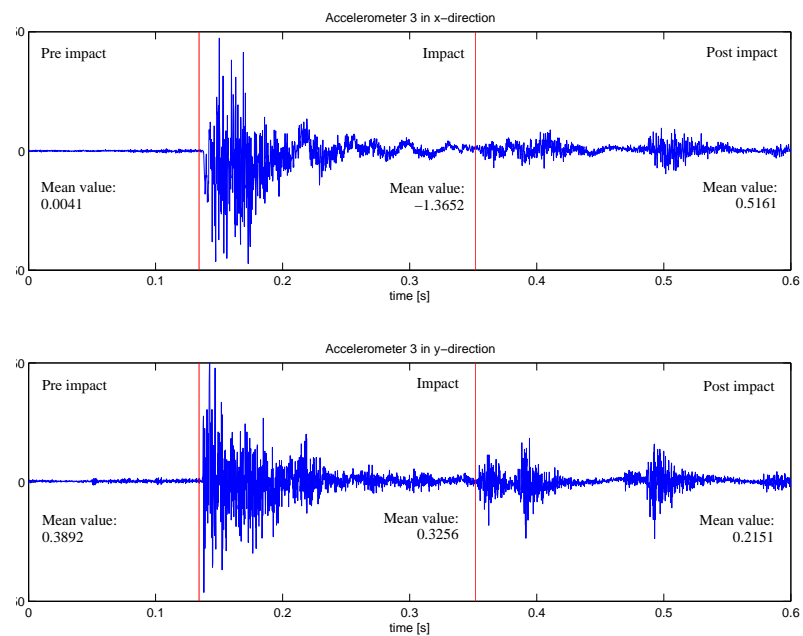


Figure 5.9: The mean values during the different phases.

Chapter 6

Implementation of possible improvements

6.1 The problems

In this section, a brief introduction to the different problems encountered during the crash test series is given.

6.1.1 Displacement

When performing the barrier tests with an offset barrier (the AZT-test), the test vehicle tends to rotate slightly because of the uneven force distribution. The rotation exposes the bumper system to transverse forces. Because the bumper system mainly is built to absorb energy in the longitudinal direction, the transverse forces make the crash-boxes fold differently than intended and, consequently, absorb less energy. The rotation also causes the conformity with computer simulations to be poorer. The rotation is illustrated in figure 6.1.

6.1.2 The distance/compression measurement

The compression of the bumper is measured by measuring the distance to the test vehicle. This is done with a laser which measures the distance to a metal plate mounted on the front of the vehicle. The laser is an accurate instrument, but when the test vehicle is rotated, it will produce an error. This error is due to the fact that the metal plate will rotate with the car which in turn gives the impression that the car is closer than it actually is. Figure 6.2 illustrates this problem.

6.1.3 Time delay

The load-cells have a built-in low-pass filter to remove the high frequency noise during impact. This filter introduces a time delay and is not possible to deactivate. This is not a problem when the measurements from the load-cells are considered by themselves, but when

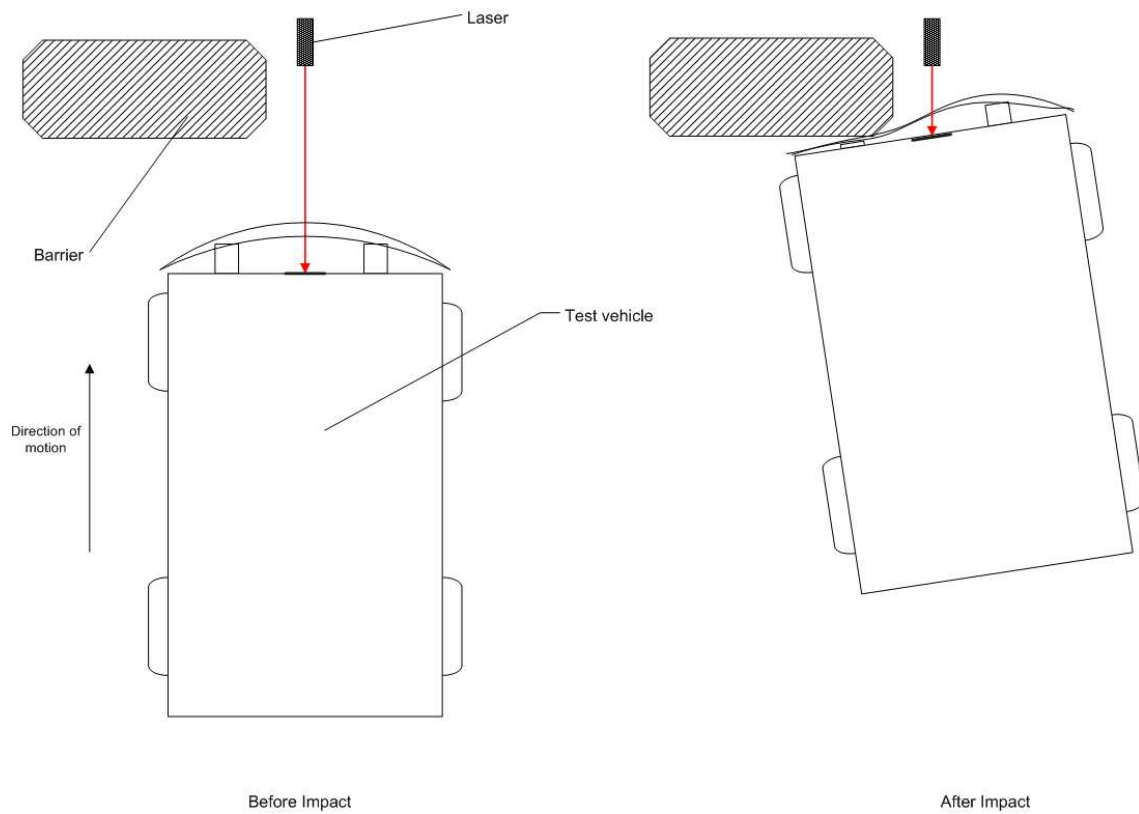


Figure 6.1: Rotation of the test vehicle when performing the barrier test with an offset barrier.

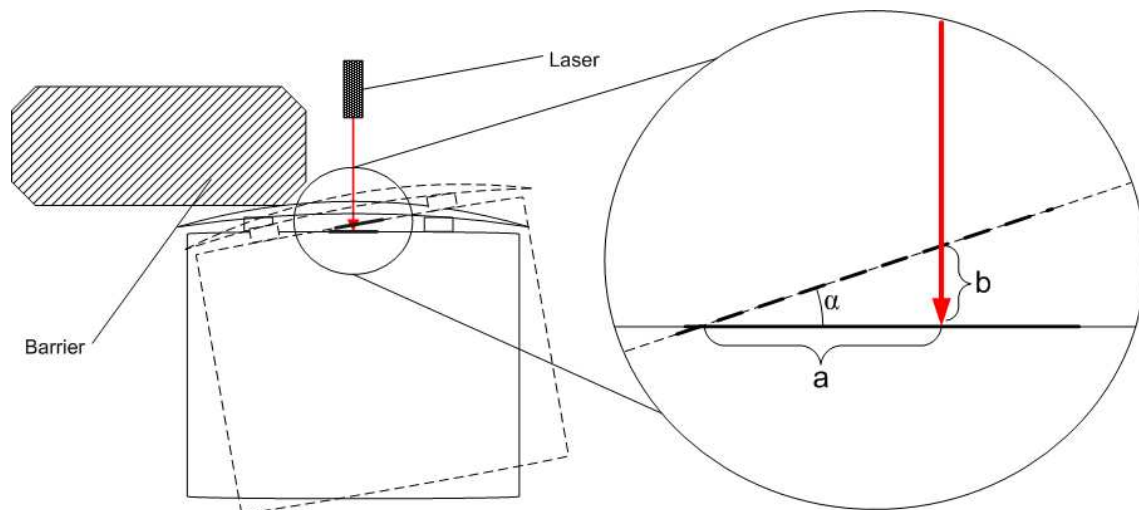


Figure 6.2: The compression error as a result of the rotation. a is the distance from the rotation point to where the laser hits, b is the error in the distance measurement and α is the rotation angle.

they are used in combination with other sensors, problems may occur. When compared to other sensors (like the accelerometer which has virtually no time delay), the readings from the load-cells will be delayed and consequently have to be corrected by the corresponding value if they are to give correct results. Observations indicate that the time delay is close to 14 samples, which is about 2.8 ms.

6.2 The different phases of the impact

The impact can be divided into three different phases; the pre-impact phase, the impact phase and the post-impact phase. In this section a brief description of each phase will be given along with an overview of which sensors are available during the different phases.

The pre-impact phase

The sampling of data begins roughly at 130 milliseconds prior to the impact. In this phase the available sensors are the speed measuring unit, the accelerometers and the load-cells. The range finders won't produce an output because they are preset to measure compression during the impact. The speed measuring unit will only give us the mean value of the speed, but since the time span is very short and the forces acting in the direction of the movement are relatively small, this is a good estimate. The accelerometer measurements should be very close to zero in this phase because of the constant speed, but during tests it is seen that they give a significant output. Consequently, these readings will be treated as a bias error by which we will try to correct the accelerometer readings in the succeeding phase.

The impact phase

This phase is the period from when the bumper system first makes contact with the barrier until it is freed from it. The phase lasts for about 300 milliseconds. Sensors available during impact are the accelerometers, the load-cells and the range finders. There is no velocity measurement available during this phase. After studying crash test high-speed videos, it seems probable that the rotation occurs during this phase. The accelerometer measurements are considered the least reliable of the sensors available. The reason for this is that the outputs have a considerable amount of noise caused by vibrations in the vehicle. The same vibrations also cause the accelerometers to experience accelerations greater than their measuring limit which in turn may lead to large bias errors. The load-cells and range finders, on the other hand, are considered to be more reliable sensors.

The post-impact phase

The post-impact phase is when the test vehicle rolls away from the barrier after impact. This phase is somewhat similar to the pre-impact phase with the exception that there still are vibrations from the crash present in the vehicle and the velocity is smaller and in negative direction. The available sensors are the same as in the pre-impact phase. In order to obtain

a more realistic result with the Kalman filter, two assumptions are made in this phase. The first assumption is that the velocity in y-direction (sideways velocity) is zero. The second one is that there is no rotation, i.e. the angular velocity is zero. Both assumptions should hold since there are no forces acting upon the test vehicle except from friction.

Identifying the three phases

A method for identifying the three different phases described in the sections above is needed. To do this, the range finder outputs are studied since they provide a positive output during the impact. The impact phase is defined to be when the output from PGB3 (the lower range finder) is larger than zero. After defining the impact phase, finding the pre- and post-impact phase is a simple task.

6.3 Kalman filter

The system has a great redundancy of sensors. A Kalman filter is able to use a variety of measurements and predict the states of a process using a mathematical model. The two matrices \mathbf{Q} and \mathbf{R} are the tuning parameters and represents the process noise covariance and measurement noise covariance respectively. By tuning these, the Kalman filter will weight the measurements differently according to the amount of noise on the measurements and the reliability of the mathematical model.

Since there are different measurements available in different phases of the crash test, it might be a good idea to use a different Kalman filter for each phase. The states of the system at the end of one phase will be used as the initial conditions of the Kalman filter in the succeeding phase. Because there are three acceleration sensors, the model will yield three different velocities and positions. The simulink diagram can be seen in figure 6.3. The detailed filter can be found in Appendix A.

6.3.1 Accelerometer measurement

To begin with, the effect of the Kalman filter will be studied with only the accelerometer readings as input. In this case, the Kalman filter will have a behavior close to that of a low-pass filter, but with the distinction that the filtering is based on knowledge about the measurement noise rather than blocking out certain frequencies. In order to find what the \mathbf{R} matrix should be, the covariance from the signal from accelerometer 1 in x-direction (forward direction) before the impact is calculated. This choice is made because the three measurements in x-direction have about the same covariance, while the measurements in y-direction have a considerable bias in addition which makes finding the covariance more complicated. All measurements from the accelerometer should have roughly the same covariance, since the same hardware (accelerometers and cabling) is used with each accelerometer. For that reason, it is assumed that all three accelerometers have the same covariance.

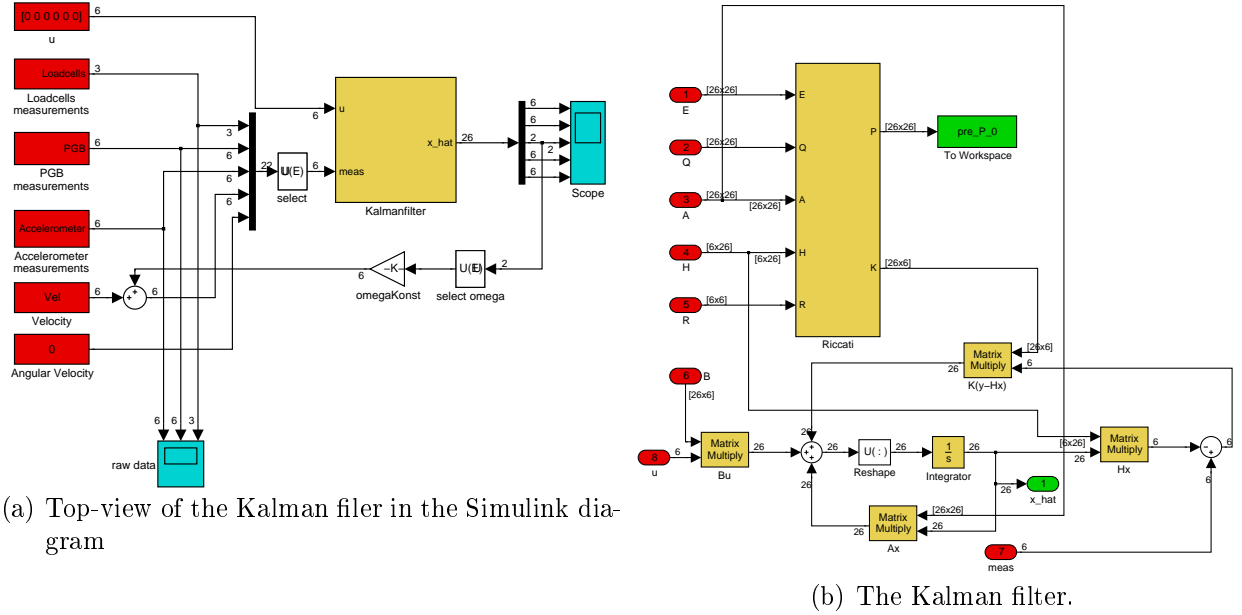


Figure 6.3: The Simulink model of the Kalman filter.

6.3.2 Accelerometer, load-cells, position and velocity measurement

In order to improve the results from the previous subsection, the load-cells and velocity measurement are used as input to the Kalman filter in addition to the accelerometers.

In the pre-impact phase, the velocity in y -direction and the acceleration in both y - and x -direction are close to zero. For that reason, the state equation derived in section 3.4 describing the acceleration ($\dot{\mathbf{a}} = \mathbf{w}$) is changed to $\dot{\mathbf{a}} = \mathbf{0}$. The velocity input becomes as follows:

$$\mathbf{v} = [v1_x \ v1_y \ v2_x \ v2_y \ v3_x \ v3_y]^T = [v_{meas} \ 0 \ v_{meas} \ 0 \ v_{meas} \ 0]^T \quad (6.1)$$

where v_{meas} is the impact velocity found by the velocity measuring unit. $v1$, $v2$ and $v3$ are the velocities related to $a1$, $a2$ and $a3$ respectively.

In the impact phase, the bias needs to be initialized. It is especially important to have good initial conditions for the bias in y -direction, since there are no other measurements in y -direction except the accelerometer input in this phase. There are two possible approaches to this. The first is to look at the accelerometer output in the pre-impact phase and have the initial values based upon them. A sensible approach in this case, is to take the mean value of the accelerometer output and use them as initial conditions for the respective biases. The problem with this approach is that the bias error changes on impact and often grows much larger than in the pre-impact phase. Therefore, a second approach where we can use the knowledge of future bias is desirable. Future bias is available since the estimation doesn't take place in real time. The method used in this report takes the mean value of the accelerometer outputs in y -direction during and after the impact and uses this value as the

initial bias values. The reason for doing this, is that the mean value on the accelerometer outputs in y-direction should be zero since it has the same velocity before and after the impact. Therefore, a nonzero value here, represents a bias error. In x-direction, the same procedure is used, but the mean value has to be taken over the last 200 samples if we are to expect a value close to zero. The sensors used in this phase are the accelerometers, range finders and load-cells. The output from the load-cells are divided by the test vehicle's mass and used as a acceleration measurement.

In the post-impact phase, the inputs to the Kalman filter are as follows: accelerometer, velocity and rotation angle. The last one is not an actual measurement, but rather a constant equal to zero. This to illustrate that there is no rotation in this phase of the impact, which is a reasonable assumption. The rotation angle input to the Kalman filter should be removed when unbiased readings are achieved. The velocity input is the same as in the pre-impact phase with the distinction that the algorithm used to find the impact velocity is used only on the samples in the post-impact phase, thus producing the velocity of the test vehicle rolling back after impact.

6.3.3 Manufactured test data

Since the accelerometer outputs are so erroneous, a test data set is created in order to test the Kalman filter on a set without the bias error. This is first done with the accelerometer as the only measurement and then with the accelerometers, velocity measuring unit and range finders as sensors.

The acceleration signal is generated in the Matlab file `generateSignal.m` and then used as input in the simulink model `fabrication.mdl` to generate the range finder measurements. The simulation is done with a considerable amount of noise on the sensor readings in order to observe how well the Kalman filter performs.

6.4 Finding the rotation angle using the lasers

Another way of finding the rotation angle is to use the two range finders and some simple geometry. If the distance between the range finders is known, the rotation angle can easily be found by considering the difference in their output. The matlab file `rotFromPGB.m` computes the rotation angle using information from the range finders. Figure 6.4 illustrates this solution where h is the difference in the output from the range finders, d is the distance between them and θ is the rotation angle.

6.5 Force/Displacement plot

The force/displacement plots, as described in section 3.1, are usually used to indicate how much energy the bumper system absorbs and how much of this energy is plastic or elastic. Since this is an essential plot in analyzing the crash tests, it may be of interest to look into

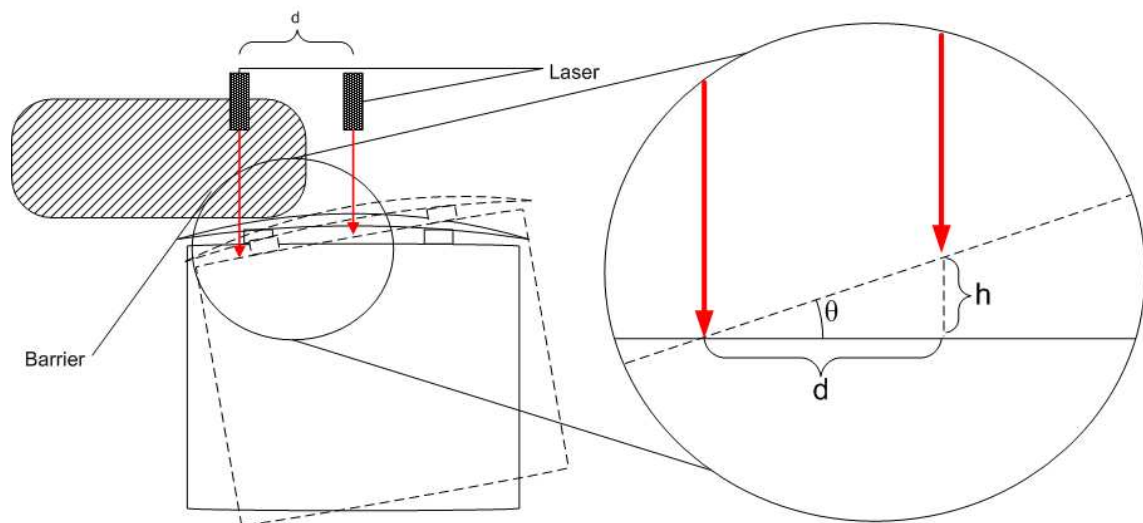


Figure 6.4: Calculation of the rotation angle using PGB3 and PGB4.

the influence, if any, the problems identified earlier in this chapter have on these plots. The force/displacement plots will be found using range finder measurements, load-cells, and the estimated values for acceleration and position.

Chapter 7

Results and discussion

In this chapter the results of the tests described in the previous chapter are presented and discussed. The performance of the instruments are evaluated as well.

7.1 Accelerometer measurements

The output from the accelerometers can be seen in figure 7.1(c). It is seen that there's a lot of noise in the signal and a bias error after impact. On the measurements in y-direction, there's a bias error prior to the impact as well. The vibration noise is filtered out well, but the bias error is not possible to counter since there are no other measurements. This bias error leads to great errors when estimating velocity and position because of the integrations needed to obtain these estimations. In series 9266 the bias errors are particularly large. The results for series 9266 can be seen in appendix C.1.

As can be seen in figures 7.2(a), 7.2(b) and 7.2(c), the rotation estimates are very poor. During the test series the rotation angle was measured with a protractor to be between 5-6 degrees.

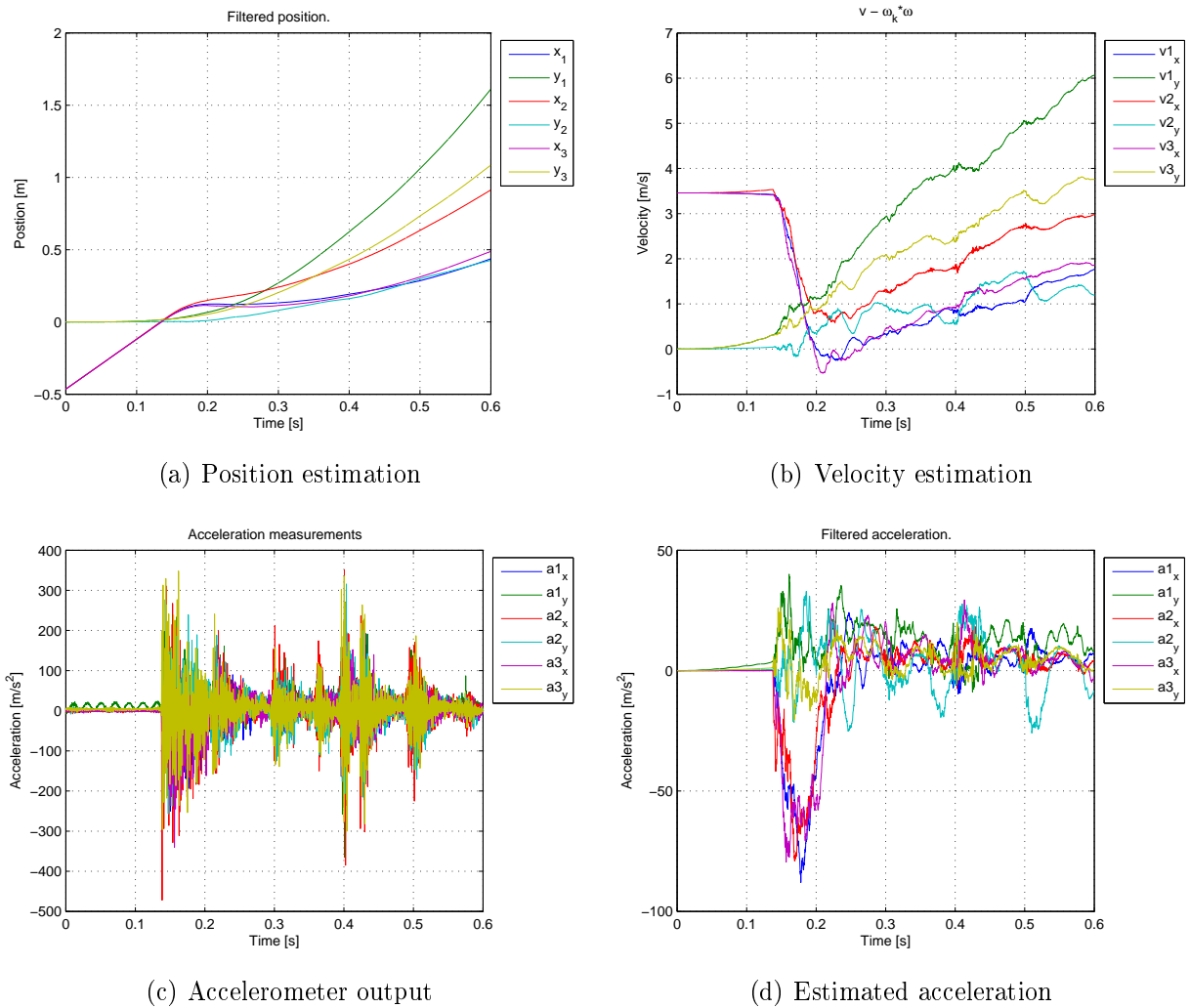
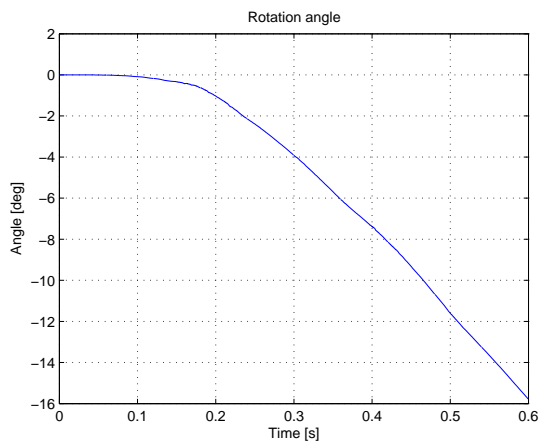
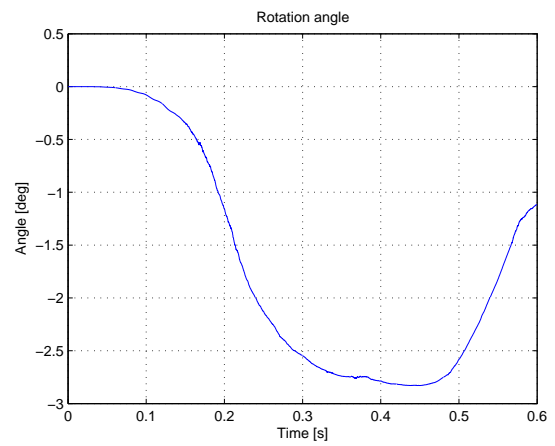


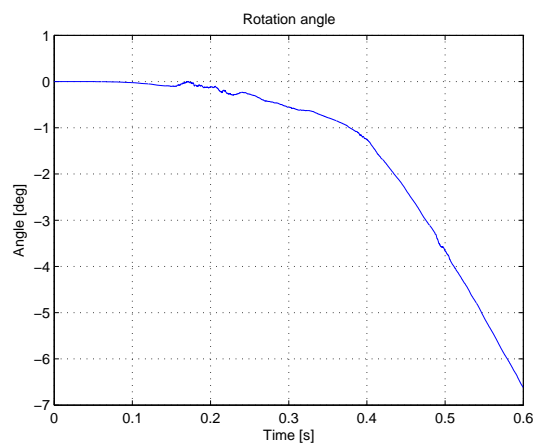
Figure 7.1: Results from series 9265



(a) Estimated rotation angle (9265)



(b) Estimated rotation angle (9266)



(c) Estimated rotation angle (9267)

Figure 7.2: Rotation angle estimation in series 9265-9267

7.2 Accelerometer, load-cells, velocity and position measurements

With the use of more sensors, the results are significantly better. Since the extra sensors all measure in x-direction we don't get any improvements in the y-direction, which is the one of importance with respect to finding the rotation angle. However, the $\mathbf{v}_y = \mathbf{0}$ in the post-impact phase, prevents the drift in velocity and position in y-direction. When observing

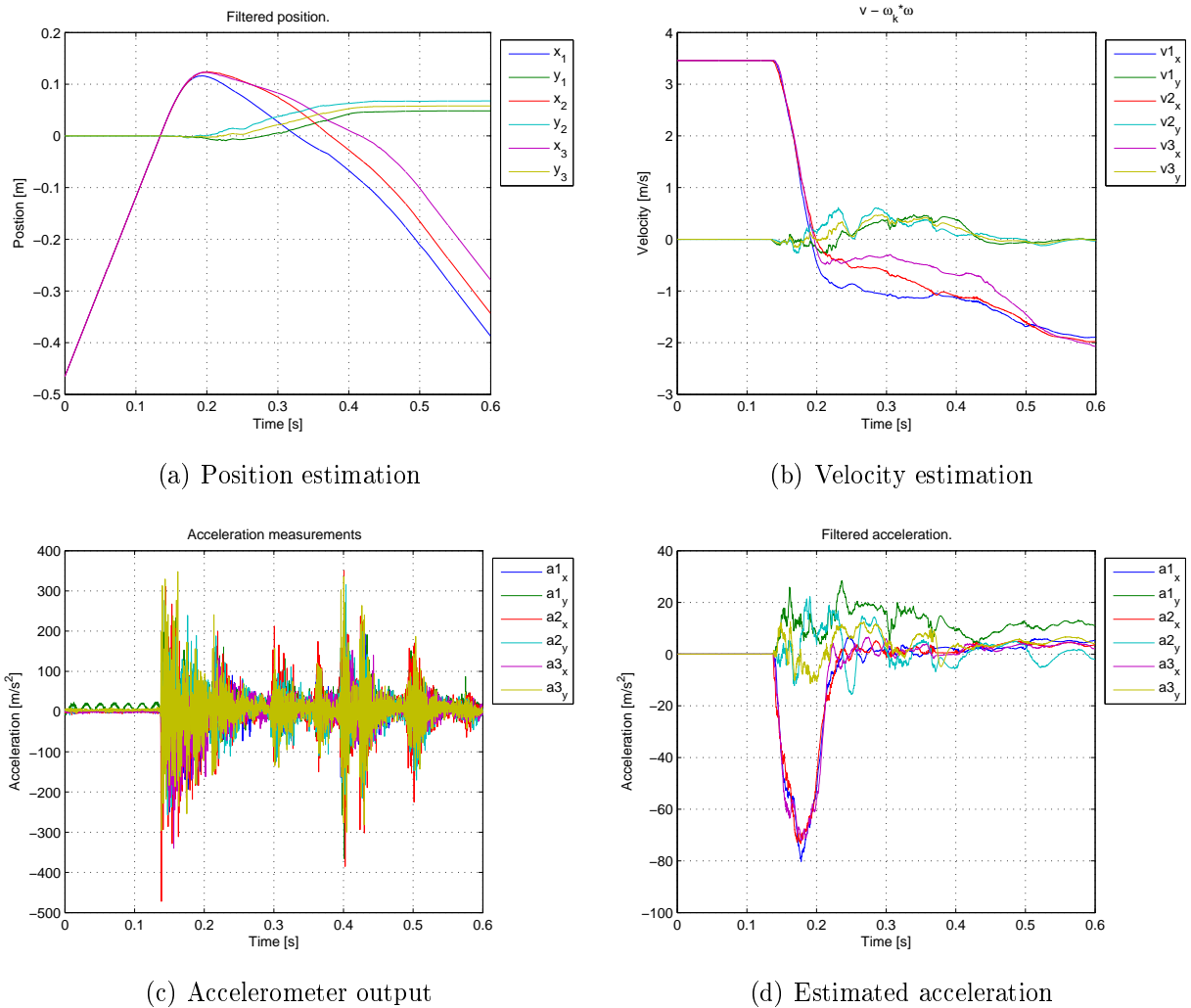
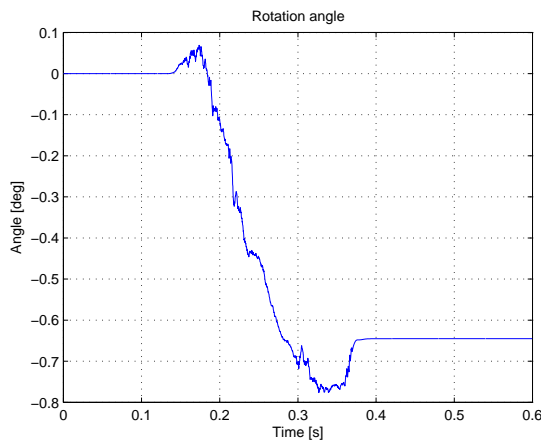


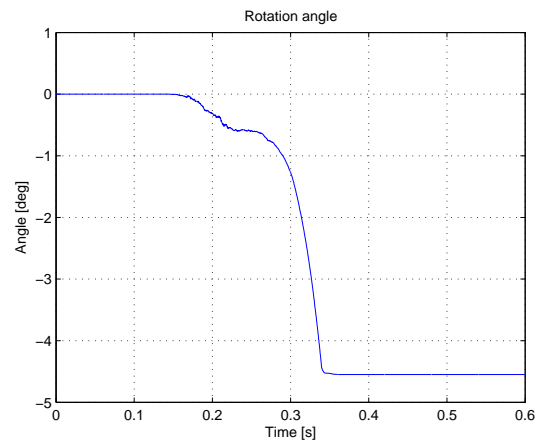
Figure 7.3: Results from series 9265

the estimated rotation angles in figure 7.4, they seem random and are poor estimates. The main difference from the estimates in figure 7.2 is that the angular velocity is set to zero after the impact, forcing the rotation angle to stabilize. Also, a change in the tuning parameters, \mathbf{R} and \mathbf{Q} , contribute to a slight change in the estimation. The velocity in y-direction is

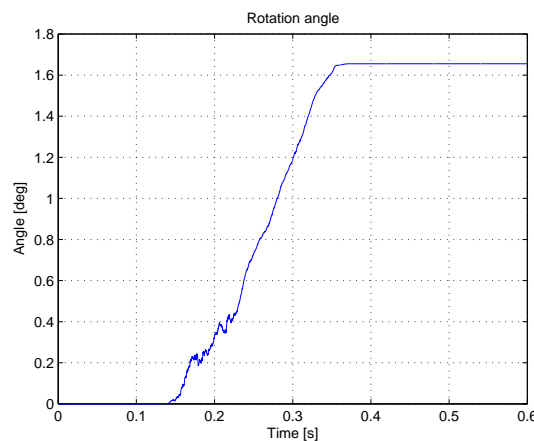
also set to zero in the post-impact phase, which prohibits the position from drifting and the acceleration from having an offset error.



(a) Estimated rotation angle (9265)



(b) Estimated rotation angle (9266)



(c) Estimated rotation angle (9267)

Figure 7.4: Rotation angle estimation in series 9265-9267

The estimations in figure C.4 are quite good, but still suffer from the large biases on the accelerometer outputs. If these are eliminated, the Kalman filter will most likely produce very good estimates. The best way to eliminate the bias error would be to make sure that the accelerometers don't become subject to the large amplitude vibrations caused by the impact. This can be done by protecting the accelerometers mechanically by using compliant materials, such as a rubber interface pad, when mounting them. A rubber interface pad will create a mechanical filtering effect by isolating and damping high-frequency transmissibility. If it turns out to be difficult to eliminate these errors, additional sensors measuring the movement in y-direction are needed. They will help the Kalman filter estimate the bias error. The accelerometers should, however, be replaced by new ones with a larger measuring

range if the vibrations can't be mechanically filtered out.

Another severe problem is that the estimation of the rotation angle depends heavily on that the actual rotation point is very close to the one assumed in the computations. If the assumed rotation point is far off, the angles α_{1x} , α_{1y} , α_{2x} , α_{2y} , α_{3x} and α_{3y} computed in section 3.3 will be wrong. The rotation point can roughly be found by observation of several crash tests.

7.3 Manufactured test data

In figure 7.5 it can be seen that there is a small deviation in the estimation of position and velocity after the rotation occurs. This deviation is a result of the linearization made in section 3.4. When more sensors are available, this deviation will decrease and the estimations will be very good. However, if the rotation occurs in a different point than where is assumed, the estimations will grow worse. The error connected with this, depends on the distance from the actual rotation point to the assumed one.

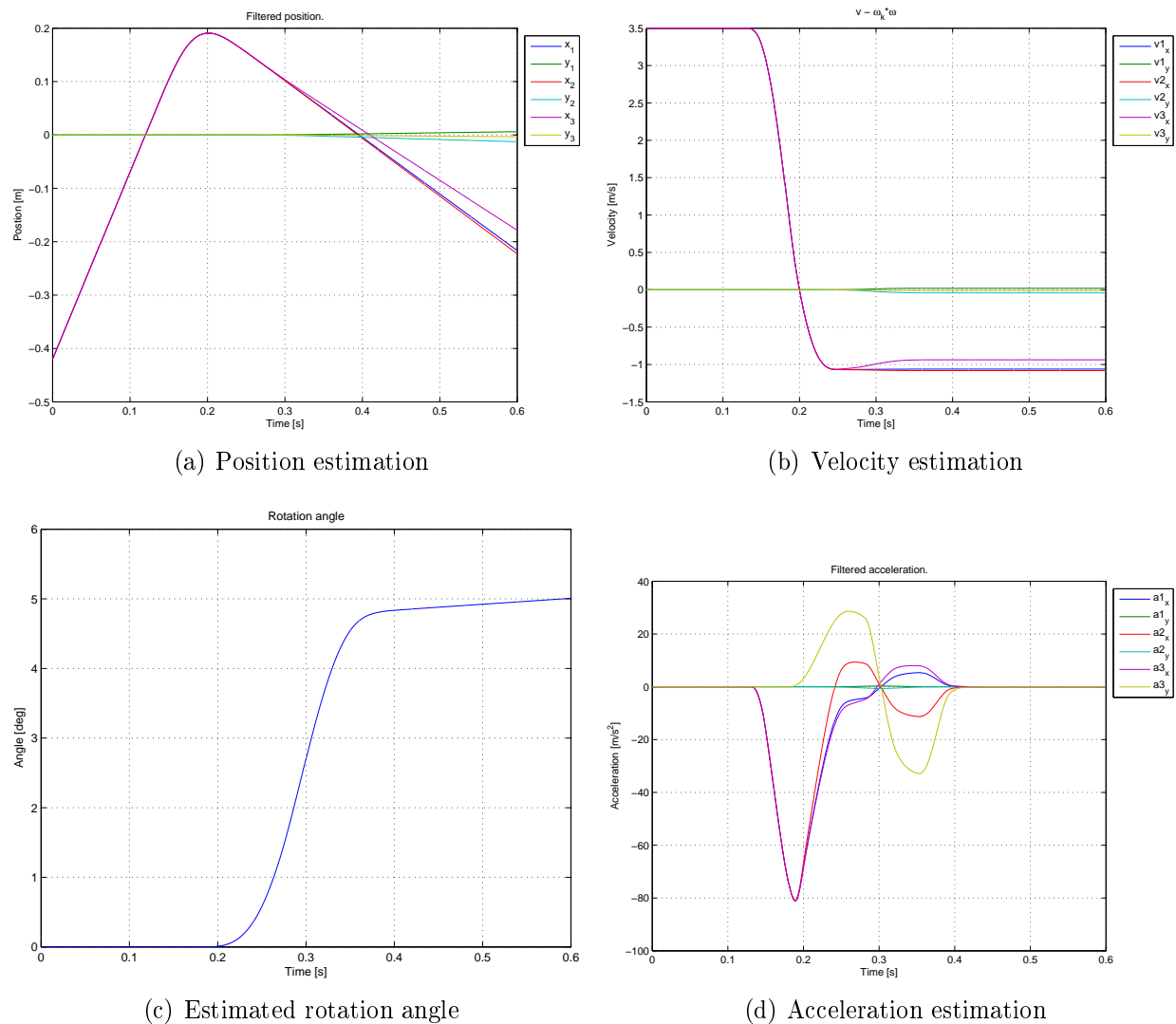
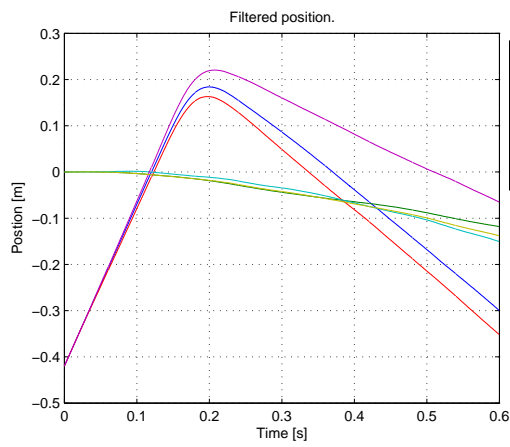


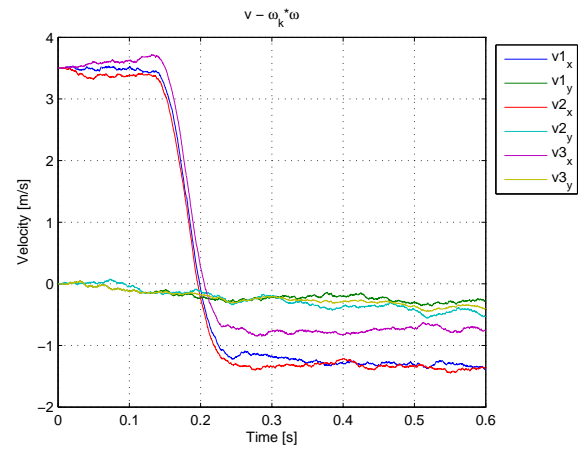
Figure 7.5: Results from the fabricated series without noise and the accelerometers as the only sensors.

In figure 7.6 it is seen that even with a considerable amount of noise, the Kalman filter still yields fairly good estimates. Because the only available measurement is acceleration, a small

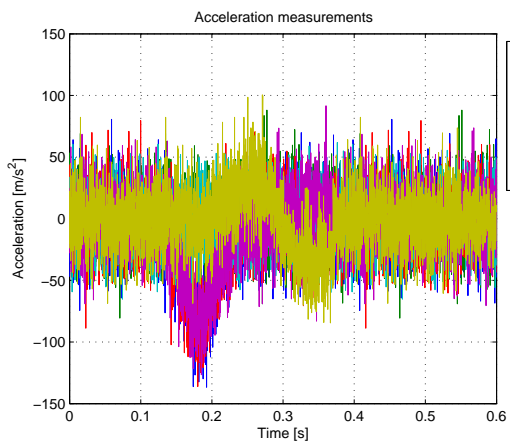
error in this estimation will give large errors in velocity and position estimates. If the range finders and velocity measurements are used in addition, the estimates improve considerably. This can be seen by investigating figure 7.7 where the noise have an amplitude of about 150 m/s². Even though the position, velocity and acceleration estimates all have improved, the rotation angle estimation has deteriorated. This is because there are no additional sensors in y-direction. There is, however, one additional assumption; the velocity in y-direction. This will contribute to the error since the rotation hasn't come to a complete stop in the post-impact phase. This argues that when the noise is within an acceptable level, this assumption shouldn't be made.



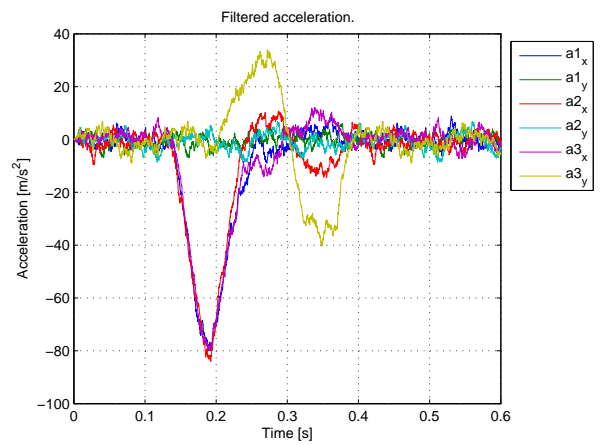
(a) Position estimation



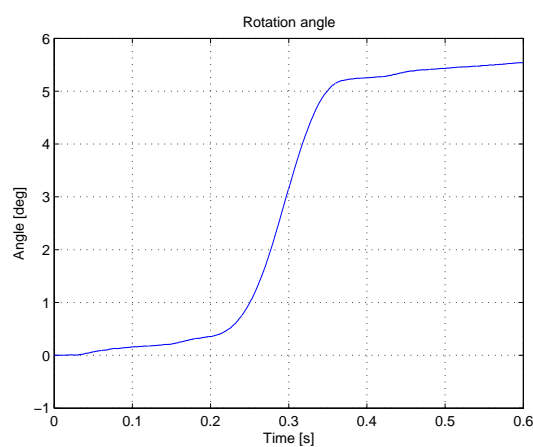
(b) Velocity estimation



(c) Accelerometer output

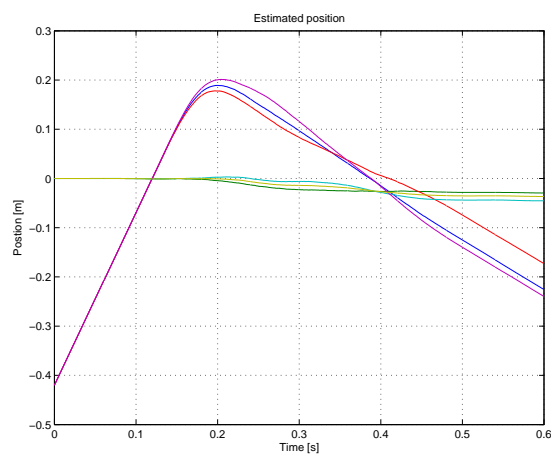


(d) Acceleration estimation

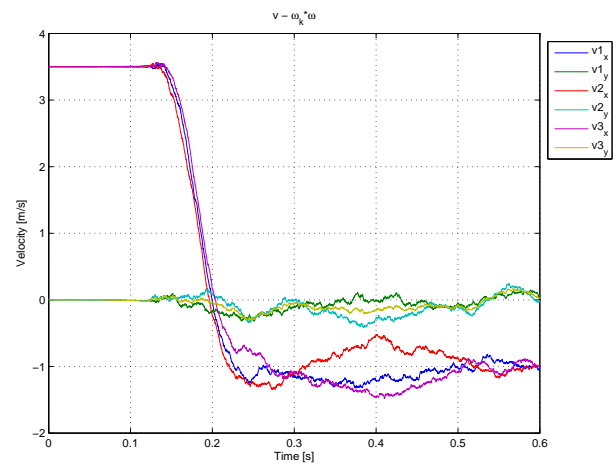


(e) Estimated rotation angle

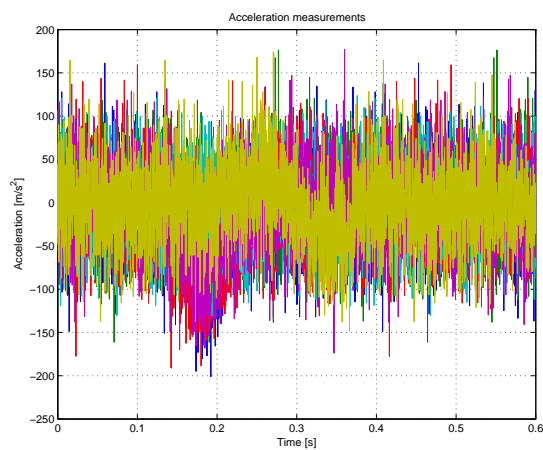
Figure 7.6: Results from the fabricated series with noise and the accelerometers as the only sensors.



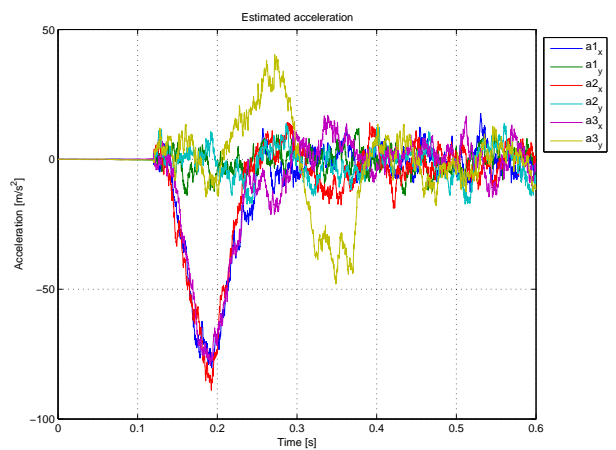
(a) Position estimation



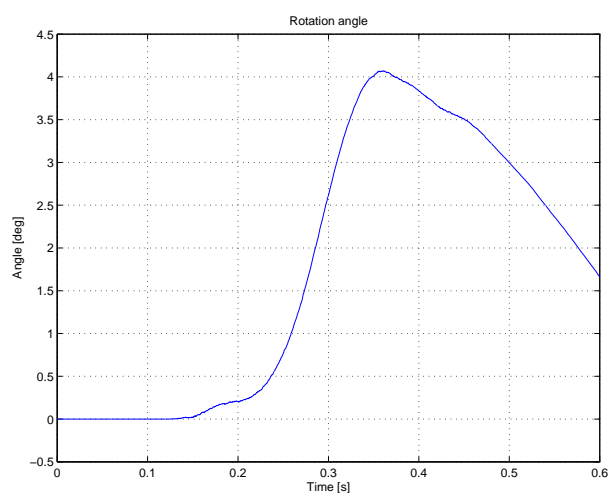
(b) Velocity estimation



(c) Accelerometer output



(d) Acceleration estimation



(e) Estimated rotation angle

Figure 7.7: Results from the fabricated series with noise and the accelerometers, range finders and velocity measurement.

7.4 Finding the rotation angle using the lasers

The matlab function `rotFromPGB.m` is used to plot the rotation angle based on the difference in the two range finder measurements. The function is applied on each of the three series considered and the resulting plots can be seen in figure 7.8. If the angle is read a few samples before the first range finder goes back to showing zero, an estimate of the rotation angle can be found. In the series 9265 - 9267, the results were 2.85° , 5.78° and 5.72° respectively.

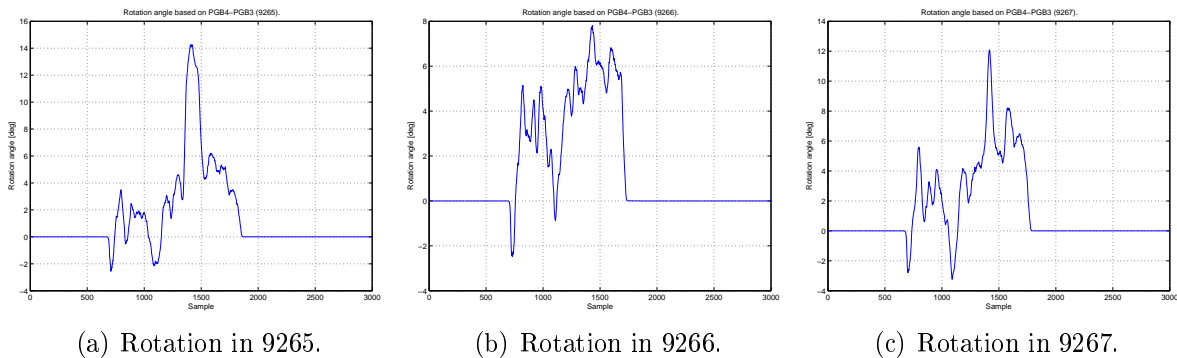


Figure 7.8: Rotation estimation based on range finder data.

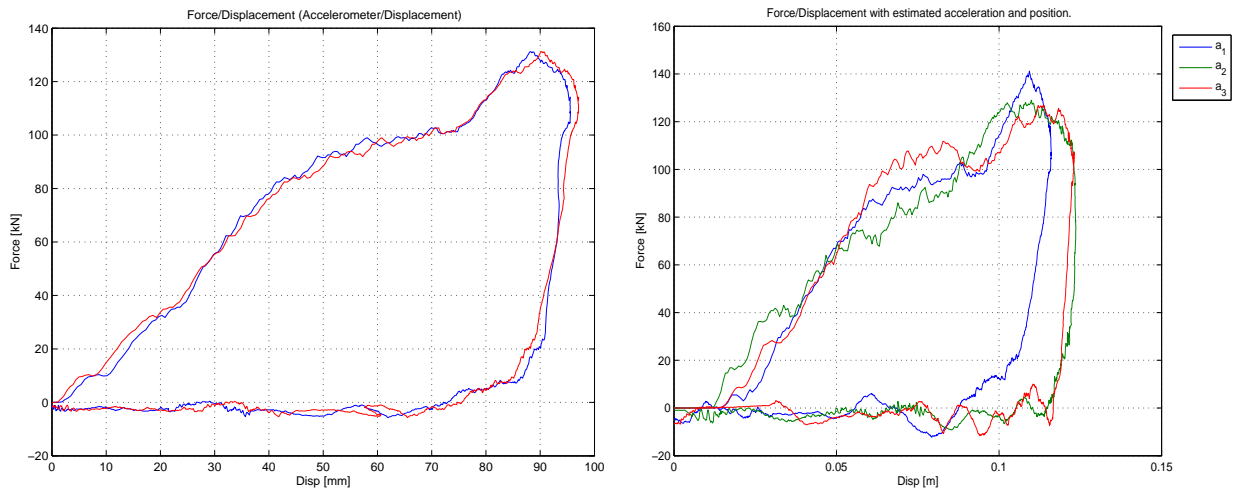
There are several sources of error in the measurements leading to the rotation angle estimate. Because the plate that the lasers are pointed at vibrates vigorously during impact, the data need to be filtered. With sensible filtering, this will not be a big problem. The plate will always vibrate at its own resonance frequency and a filter can be designed to filter out this particular frequency. Since there is no data of interest in the frequency range over the resonance frequency, this can be done by using a Butterworth filter or a simple low-pass filter. The Butterworth filter is outlined in Appendix D. If the vibrations could be removed, or at least reduced, the range finders will produce readings with a good margins of error (± 0.5 mm).

Another possible problem occurs when one of the range finders is placed on the floor beneath the barrier. In some cases, it can be knocked out of position by the test vehicle during a crash test and yield an erroneous output. The horizontal distance between the two lasers should also be measured carefully.

During the test-series 9265-9267, the distance between the range finders were unknown. In order to obtain the estimate, a guess based on figure 5.2 is made. A data set of three test-series is also not enough to determine if the algorithm is effective, although, it gives indications that it might work satisfactory. If the range finders are to be used in the rotation angle estimation, it is advised that a device with two lasers mounted on it is built. That way the distance between them will stay constant and the laser beams will be parallel. The laser should be pointed at the area of the vehicle's front-plate where the vibrations are least, i.e. the lower part.

7.5 Force/Displacement plot

The force/displacement plots from crash test series 9265 are shown in figures 7.9 and 7.10. In figure 7.9(a) the mean value of the three estimated acceleration measurements are used together with the range finder measurements. The blue plot uses the lower range finder, while the red uses the upper. In figure 7.9(b) the estimated position is used together with the estimated acceleration. Each acceleration measurement is plotted together with its respective position estimate. In order to find the force from the acceleration measurements, Newton's 2nd law is used, i.e. the vehicle's mass is multiplied with the acceleration measurements.



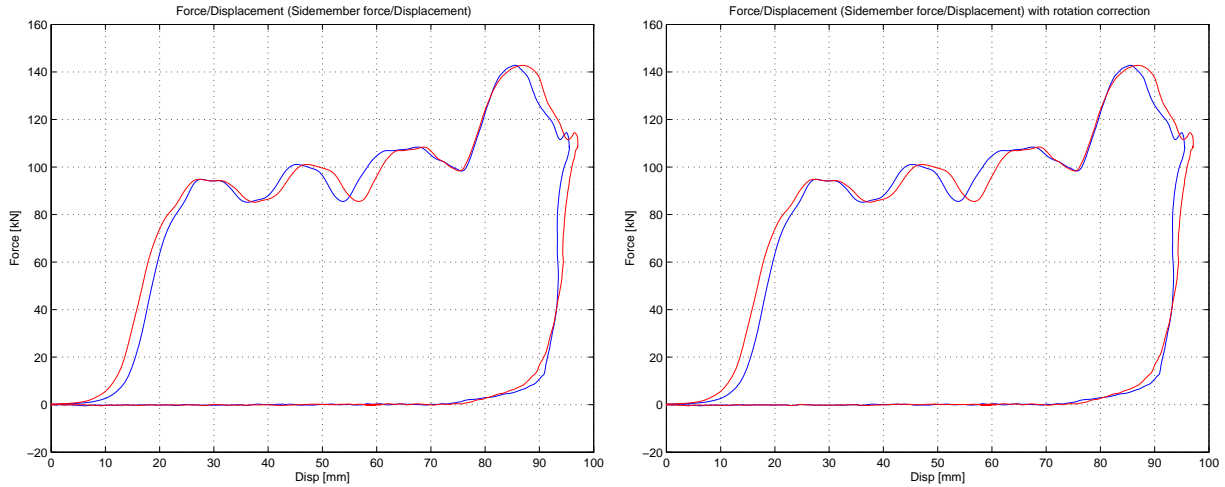
(a) Force/displacement plot using estimated acceleration and range finder measurements. (b) Force/displacement plot using estimated mean acceleration and position measurements.

Figure 7.9: Force/displacement plots using different measurements.

In figure 7.10 the range finder measurements together with the load-cell measurements are used in the plots. As in figure 7.9(a), the blue plot represents the lower range finder, while the red one represents the upper. In figure 7.10(b) the error in the upper range finder measurement has been tried corrected using the method described in section 6.1.2. It can be seen from these plots that the rotation has very little impact on the appearance of the force/displacement plots. The reason for this, is that the rotation doesn't take place before after the impact is finished, and the force is close to zero. The difference between the red and the blue plot in figures 7.9(a), 7.10(a) and 7.10(b) is a result of the difference in the two range finder's measurements.

The time delay in the load-cells have been taken into account by adjusting their measurements 15 samples relative to the position measurements. Observations of the load-cells have suggested that this is roughly the value of the time delay.

It is seen from the figures that the estimated acceleration and load-cells measurements gives two clearly different plots. However, the maximum value is about the same in all plots, and the total energy is very close as well. The most distinctive plot is figure 7.9(b) where



(a) Force/displacement plot using load-cell and range finder measurements. (b) Force/displacement plot using load-cell and range finder measurements with rotation correction.

Figure 7.10: The effect of the rotation on the force/displacement plot.

the displacement is significantly larger than in the other plots. This is due to the estimation error in the position estimate.

Because the accelerometer measurements are the ones with the most noise and bias error, it is probable that the plots in figure 7.10 are the most correct ones. However, if the improvements suggested in section 7.2 are implemented, the estimated values will provide a much more trustworthy force/displacement plot.

7.6 Evaluation of the sensors and possible improvements in hardware

Accelerometer

It can be seen from figure C.4(c) that the frequency of the measurements are at least 5000 Hz. It may be larger, but that cannot be decided since the sample rate is 5000 Hz. The accelerometers have a frequency range up to 5000 ($\pm 10\%$) Hz, which is too little. As mentioned in section 2.2, only the lower 20% of the frequency range should be used for accurate measurements.

The amplitude of the signal is also too high. The same recommendations as for frequency range apply for the measurement range, i.e. use only the lower 20% of the measurement range. In this case this is not satisfactory as the measurements frequently exceed the accelerometers' maximum measuring value of 50 g's.

If, however, the high-frequency vibrations can be damped before they reach the accelerometer, the existing accelerometers comply with the recommendations stated in section 2.2. This can be done by using an adhesive mounting base or a rubber interface pad. If

this is not possible, the existing accelerometers should be replaced by new ones that can withstand signals with higher frequencies and amplitudes.

Load cells

Except from the time lag, the load cells perform very well. When it comes to measurement range and overload capacity, they are accurate and well within the safety-margins. No changes need to be done.

Velocity measuring unit

The velocity measuring unit only measures the impact speed, but seems to do this well. From inspecting figure 5.1, it seems that the pulses are coming very closely before the impact, which may lead to some problems when computing the velocity at great speeds. However, it has been giving consistent results and seems to be working properly at the speeds under which the tests has been performed. If the test-facility at Raufoss in the future plans to run tests at greater speeds, it might be a good idea to modify the velocity measuring unit. To achieve greater accuracy at both low and high speeds, increasing the update-rate from the laser will be a good solution. A cheaper and just as good a solution, might be to change the distance between the bars in the grating. By doing this, a problem that occurs when the speed requires an update rate close to 5000 Hz, is avoided. This problem will arise very quickly as we only have 5 measurements of one pulse at 5000 Hz if the speed is 18 km/h.

Range finders

The range finders work satisfactory for their present purpose, but if they are to be used in the solution presented in section 6.4, some modifications need to be done. First off, there should be two range finders mounted on a common platform which preferably is mounted on the floor. If it's mounted on the barrier, vibrations from the impact may interfere with the measurement. The distance between them should not be too short. If it is, the estimation will depend much more on the accuracy of the range finders rather than the measured distance between them.

Chapter 8

Conclusions and recommendations

In this chapter, the results from the crash tests are summarized and suggestions for future work are made.

8.1 Conclusion

Because the vibrations in the test vehicle most likely have frequencies larger than the accelerometers' frequency range, they will introduce errors. The amplitude of these vibrations are also close to what the accelerometers are capable of measuring. These vibrations should be filtered out mechanically before they reach the accelerometers by using an adhesive mounting base or a rubber interface pad. If they can't be filtered, the accelerometers need to be replaced with new ones with greater measurement and frequency range.

It is shown that the Kalman filter's estimations improve considerably when more sensors are used. Unfortunately, none of the additional sensors measure in y-direction, which is the important direction with respect to estimating the rotation angle. With the current data, the Kalman filter yield poor results. The manufactured data set shows that the Kalman filter performs well with white-noise signals and that the linearized model performs satisfactory. Since the Kalman filter is a software solution, it will be cheap to implement. However, some improvements need to be done with the accelerometers in order to use the it.

The rotation angle can also be found by using two range finders. This method is very straightforward and needs little software implementation. The two range finders should be mounted on a rigid device for best performance.

It is also shown that the angular displacement has little effect on the force/displacement plots. The reason for this, is that the rotation occurs after the impact has finished.

The remaining sensors perform satisfactory, but the time delay in the load-cell measurements need to be compensated for. Indications suggesting that the velocity measuring unit might have problems computing high velocities, are also found.

8.2 Future work

It is recommended that the accelerometers are mechanically damped, either by using some kind of mounting base or a rubber interface pad. Then the Kalman filter should be utilized to see if it provides satisfactory estimates. The solution using range finders to identify the angular displacement should also be implemented and tested. This is an easy-to-understand solution which probably will provide good results.

The consequences of the angular displacement should be properly mapped so that the insecurity it introduces can be accounted for.

The algorithm used by the velocity measuring unit to calculate the velocities, should also be looked closer into to make sure it copes with calculating the velocity after impact. It performed well on the test-series available during the writing of this thesis, but since its primary objective is to calculate the impact speed, it would be wise to check the validity in the post-impact phase.

It is recommended that the range finder solution is implemented and the Kalman filter is tested again after the vibration problem is solved.

References

- Farrell, J. A. & Barth, M. (1998), *The Global Positioning System & Inertial Navigation*, McGraw-Hill.
- Fossen, T. I. (2002), *Marine Control Systems*, Tapir Trykk.
- Insurance Institute for Highway Safety (2002), *Low-Speed Crash Test Protocol (Version V)*, 1005 North Glebe road Arlington, VA 22201.
- Johnson, C. D. (1997), *Process Control Instrumentation Technology*, Prentice Hall PTR.
- Kulwanoski, G. & Schnellinger, J. (2004), 'The principles of piezoelectric accelerometers', *Sensor Magazine* .
- Nyhus, A. (2002), Kollisjonsmotstand til støtfangersystem: Korrelasjon mellom eksperimentelle og numeriske resultater, Master's thesis, NTNU. Restricted.
- PCB Piezotronics (2005), 'Introduction to piezoelectric accelerometers', http://www.pcb.com/techsupport/tech_accel.aspx. Last accessed 27.1.2005.
- Research Council for Automobile Repairs (1999), 'Rcar, the procedure for conducting a low speed 15 km/h offset insurance crash test to determine the damageability and repairability features of motor vehicles'.
- Research Council for Automobile Repairs (2002), 'Rcar homepage', <http://www.rcar.org/index.htm>. Last accessed 11.2.2005.
- Thompson, B. J. (2000), 'A guide to accelerometer specifications', *Test & Measurement World* .
- Tipler, P. A. (1999), *Physics for scientists and engineers.*, W.H. Freeman and Company.
- Welch, G. & Bishop, G. (2004), 'An introduction to the kalman filter'.

Appendix A

Simulink models

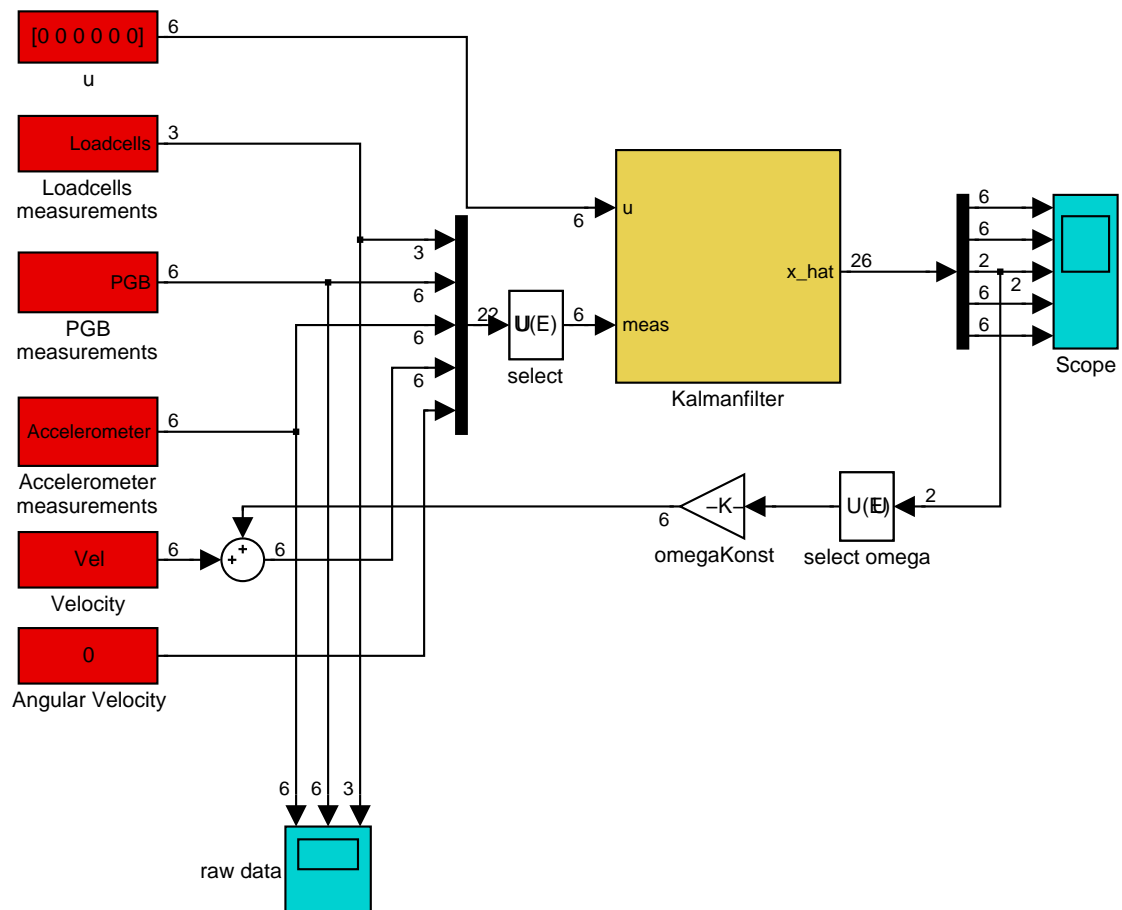


Figure A.1: Top-view of the Kalman filter in the Simulink diagram.

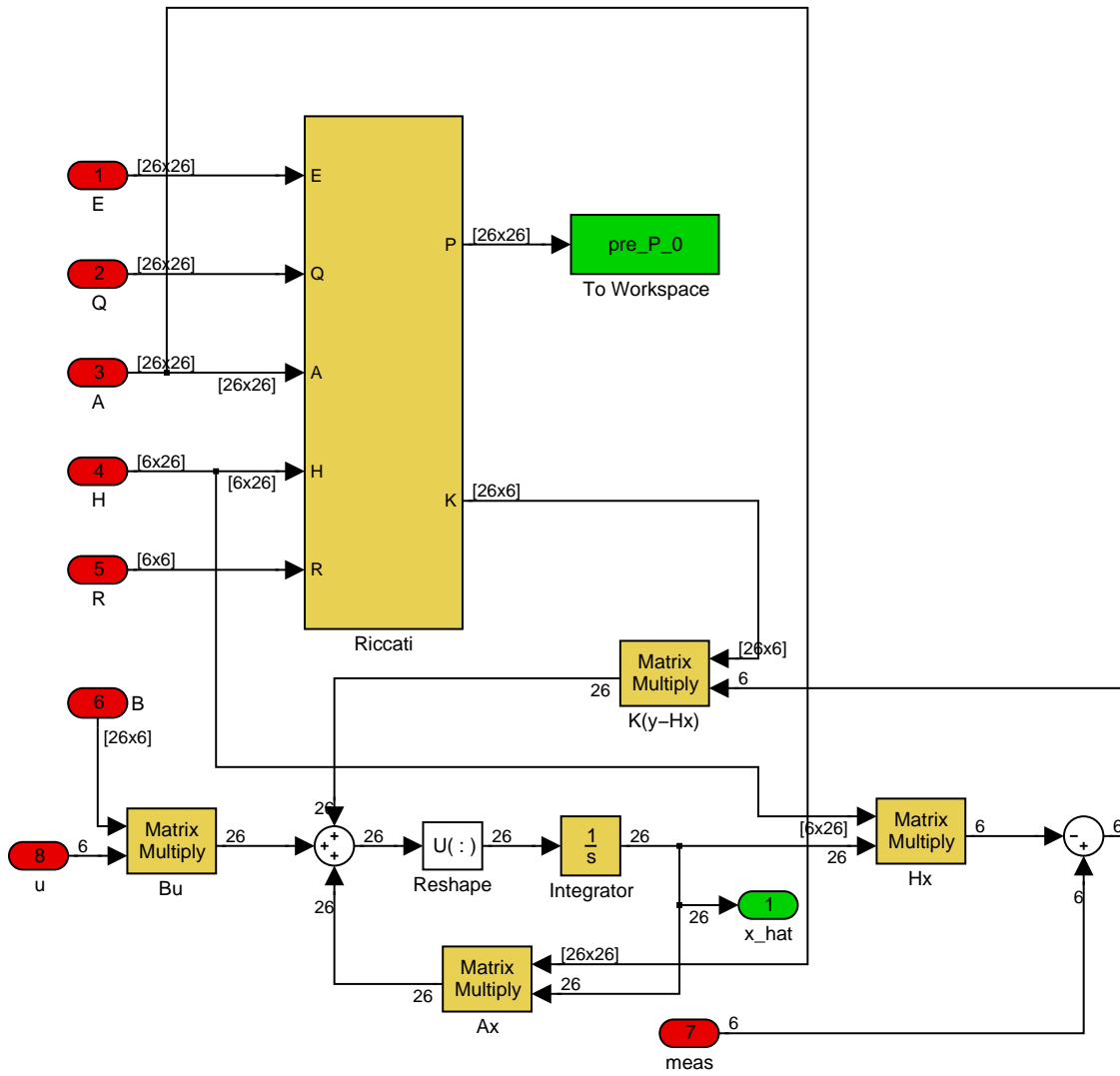


Figure A.2: The Kalman filter.

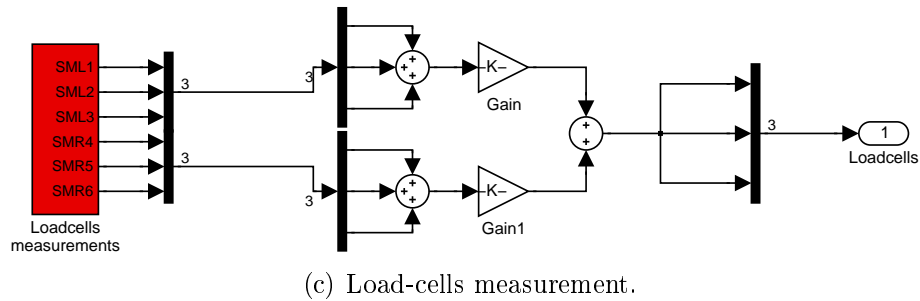
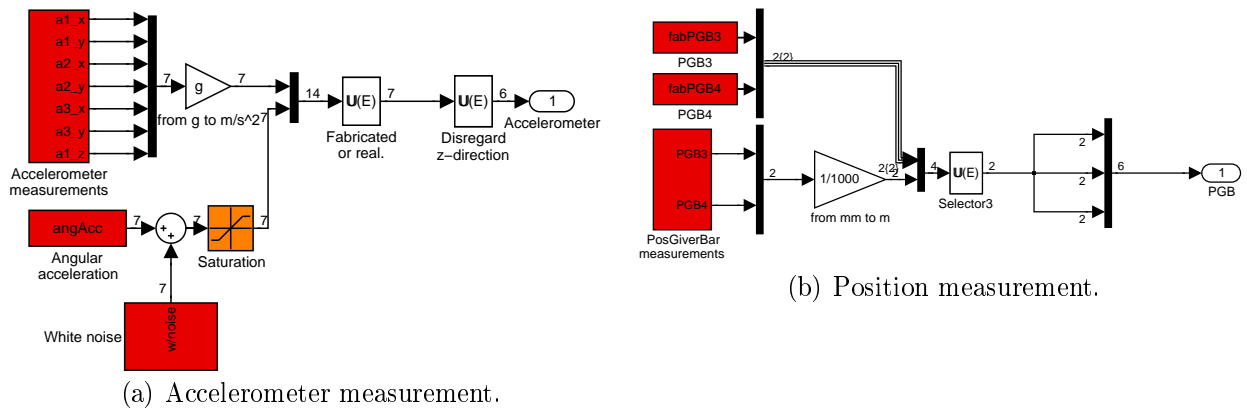


Figure A.3: The sensors in simulink. They get their data from *.mat files.

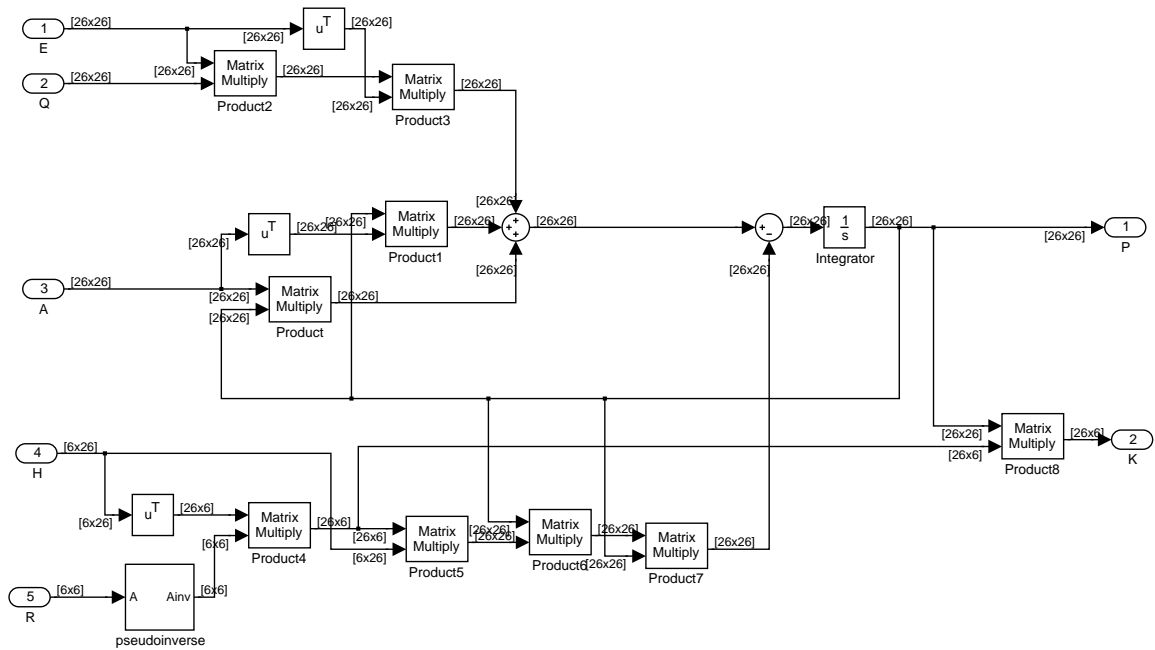


Figure A.4: The Kalman Riccati equation.

Appendix B

Comparison of test-series.

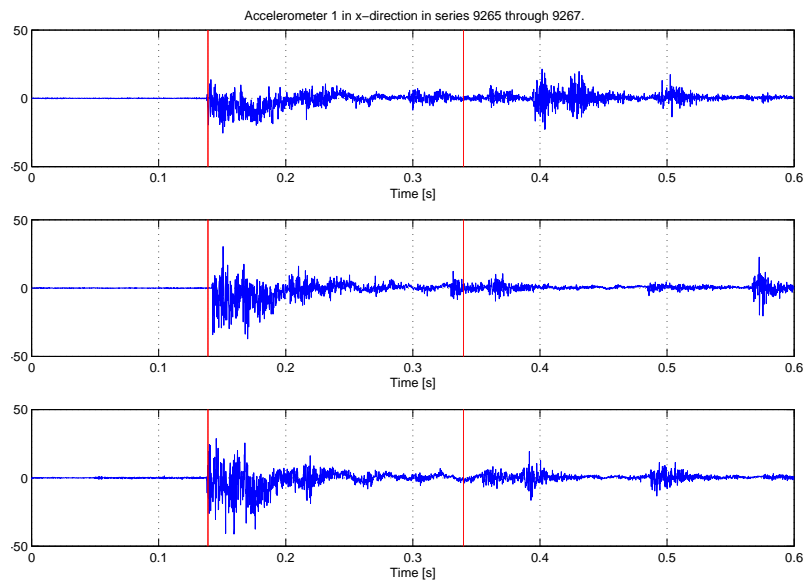


Figure B.1: Comparison of the acceleration measured in x-direction with accelerometer 1. The red lines indicate where the impact starts and ends.

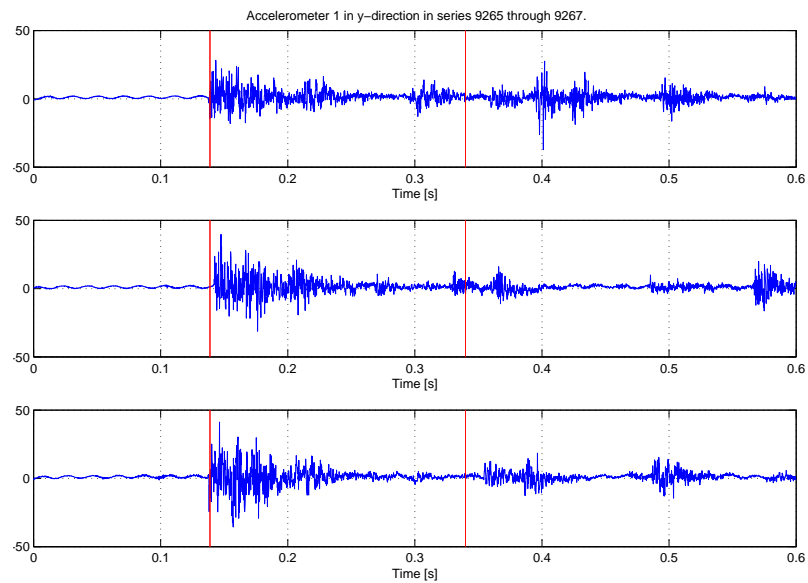


Figure B.2: Comparison of the acceleration measured in y-direction with accelerometer 1. The red lines indicate where the impact starts and ends.

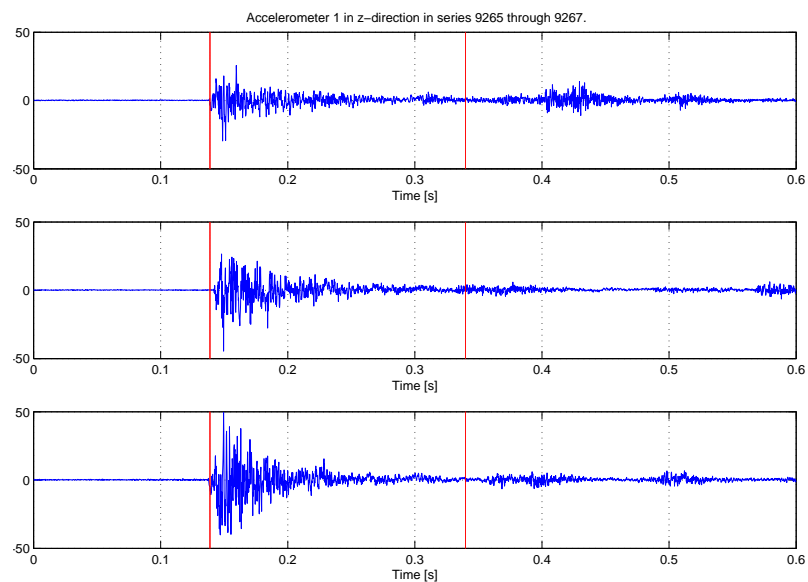


Figure B.3: Comparison of the acceleration measured in z-direction with accelerometer 1. The red lines indicate where the impact starts and ends.

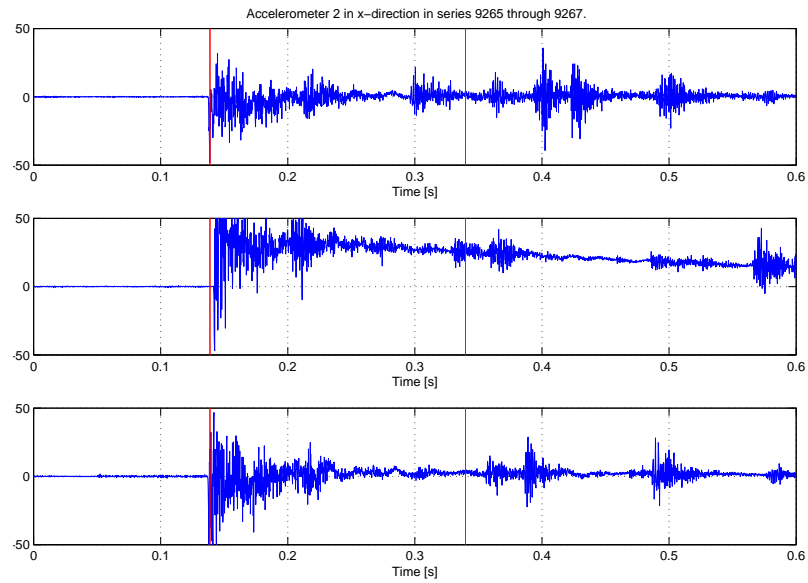


Figure B.4: Comparison of the acceleration measured in x-direction with accelerometer 2. The red lines indicate where the impact starts and ends.

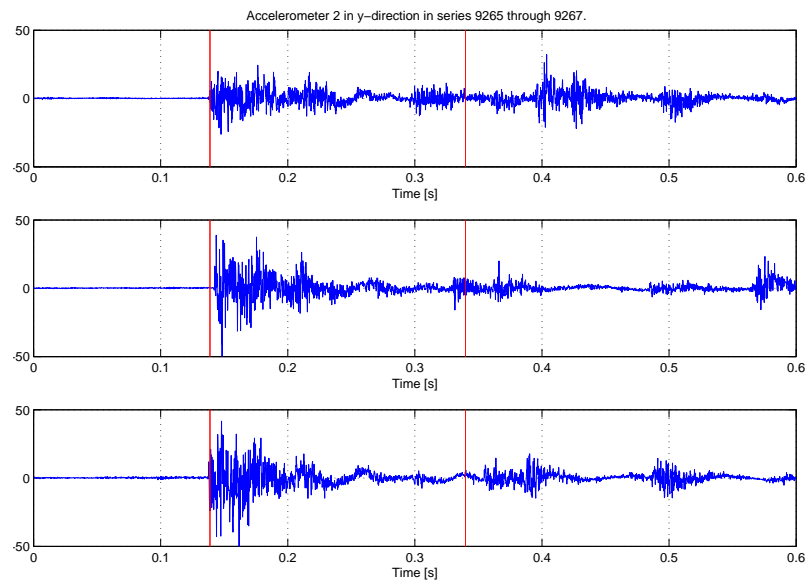


Figure B.5: Comparison of the acceleration measured in y-direction with accelerometer 2. The red lines indicate where the impact starts and ends.

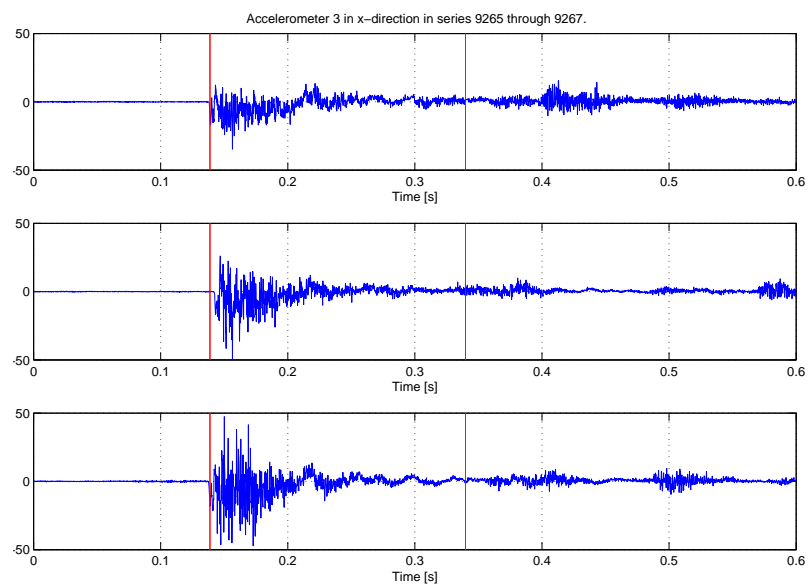


Figure B.6: Comparison of the acceleration measured in x-direction with accelerometer 3. The red lines indicate where the impact starts and ends.

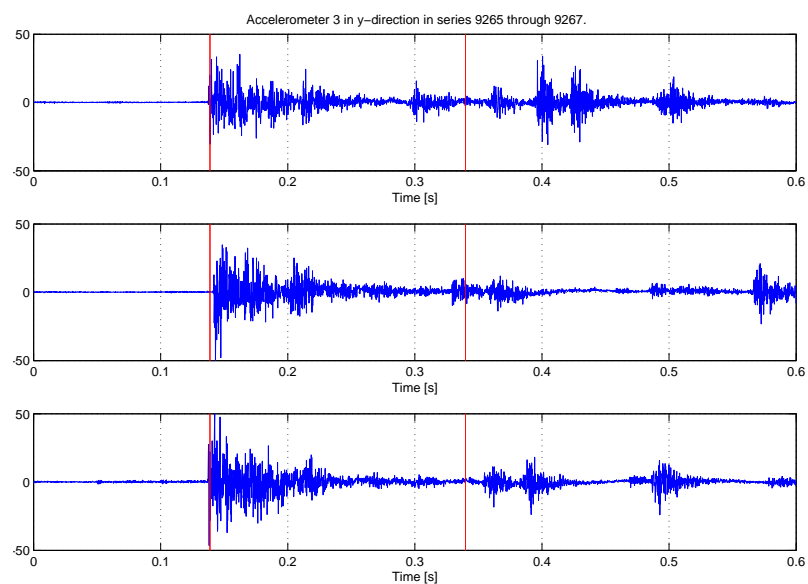
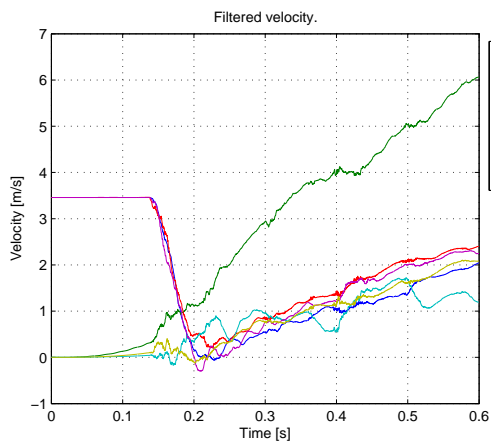


Figure B.7: Comparison of the acceleration measured in y-direction with accelerometer 3. The red lines indicate where the impact starts and ends.

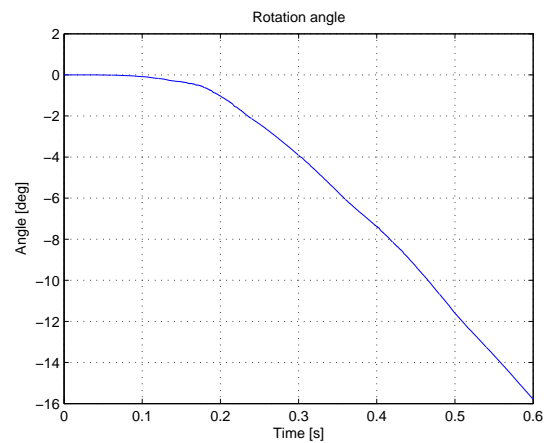
Appendix C

Plots from the results

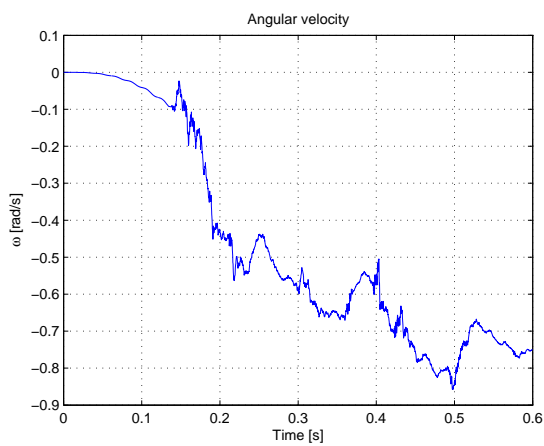
C.1 w/ only accelerometer



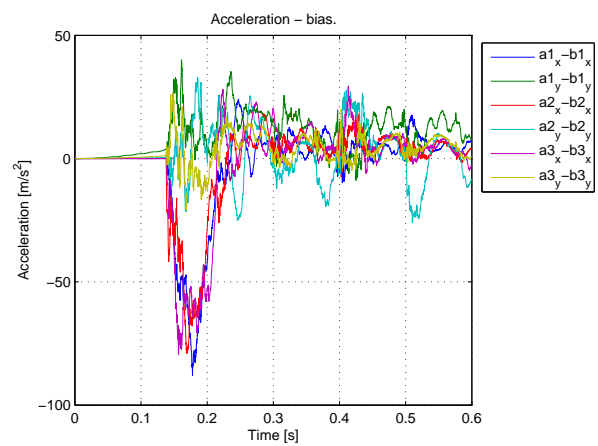
(a) Estimated velocity.



(b) Estimated rotation angle.

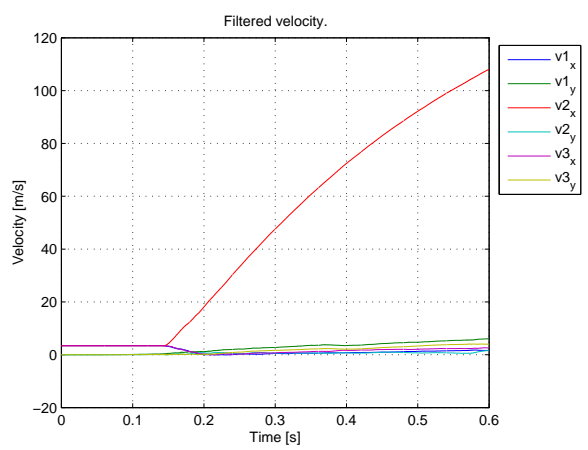


(c) Estimated angular velocity.

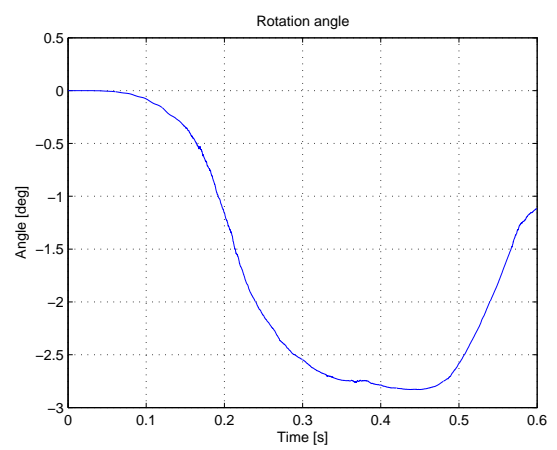


(d) Estimated acceleration minus bias.

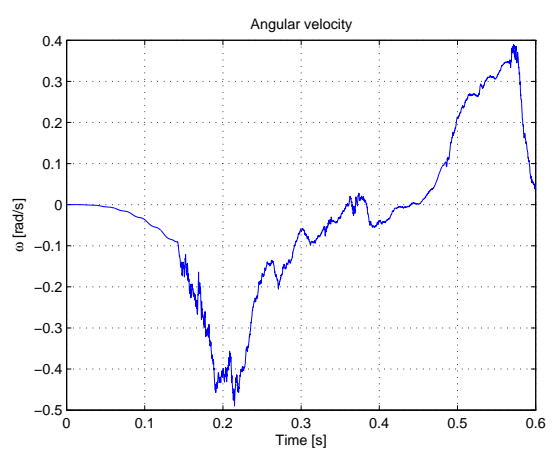
Figure C.1: Results from series 9265



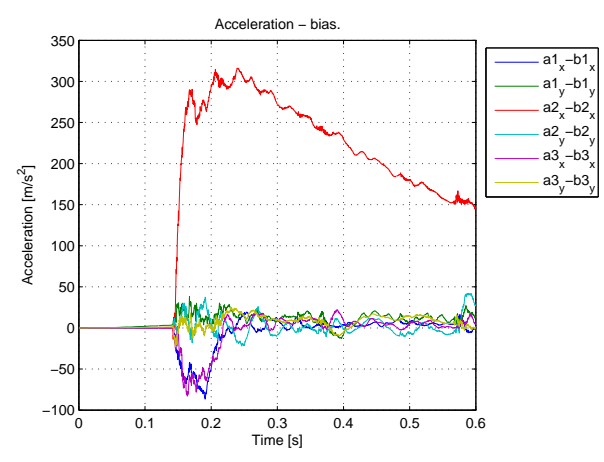
(a) Estimated velocity.



(b) Estimated rotation angle.

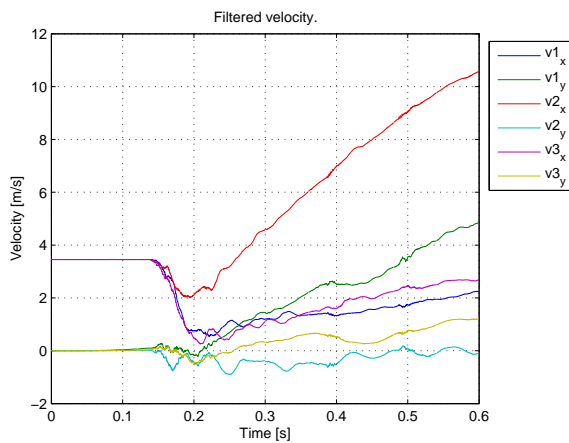


(c) Estimated angular velocity.

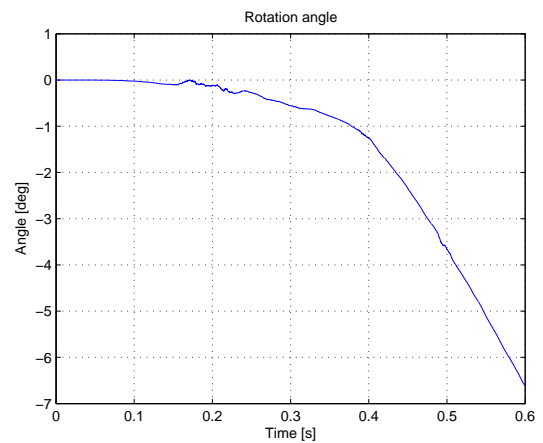


(d) Estimated acceleration minus bias.

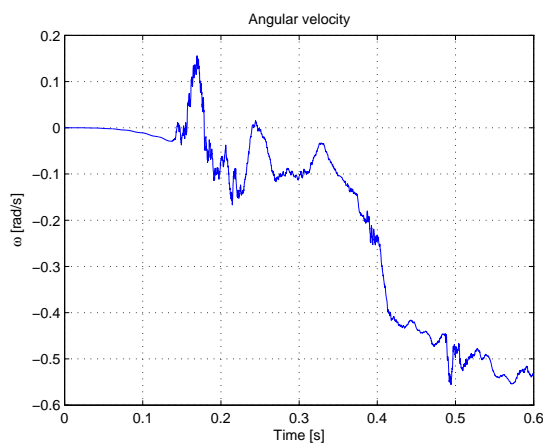
Figure C.2: Results from series 9266



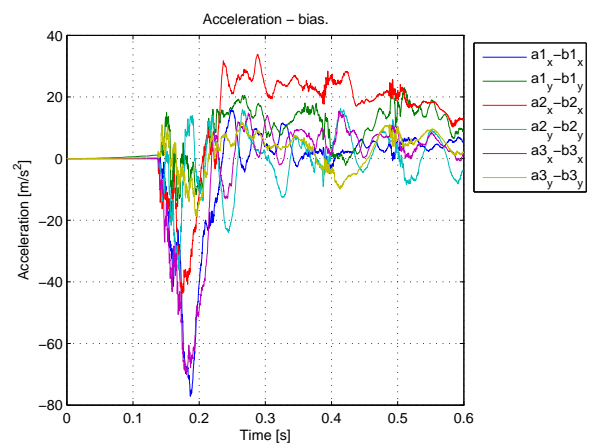
(a) Estimated velocity.



(b) Estimated rotation angle.



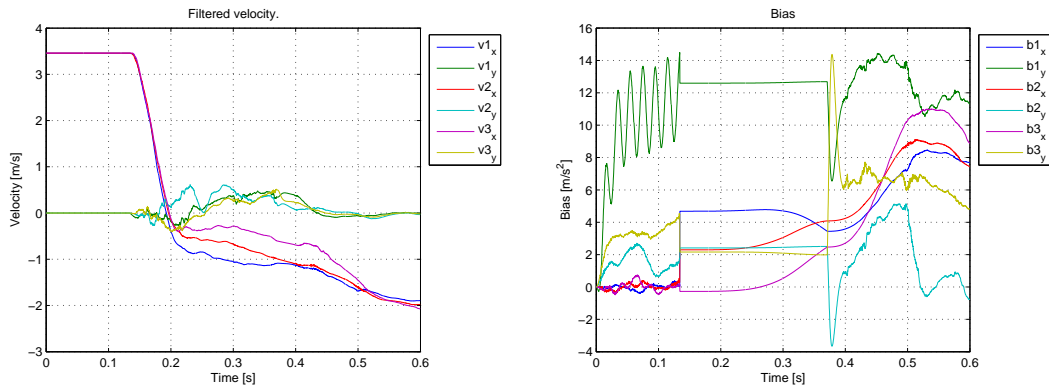
(c) Estimated angular velocity.



(d) Estimated acceleration minus bias.

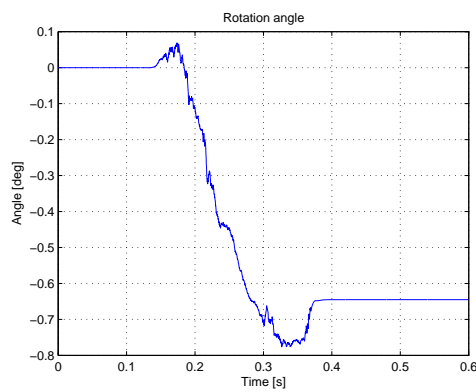
Figure C.3: Results from series 9267

C.2 w/ accelerometer, load-cells, position and velocity sensors

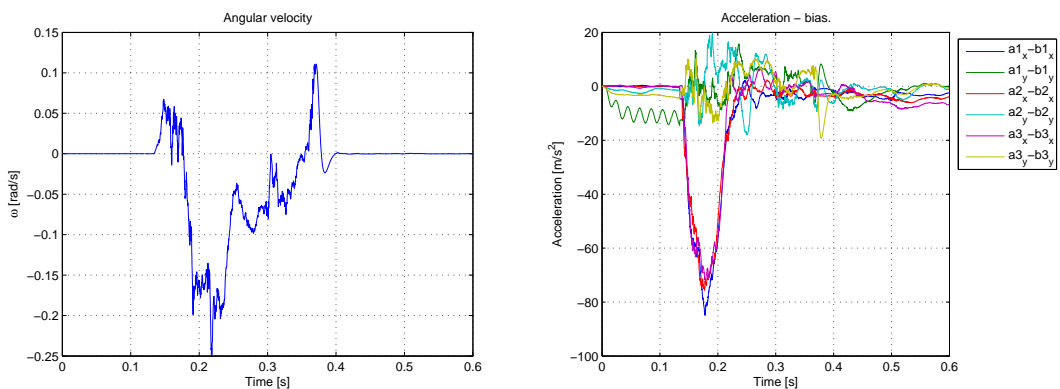


(a) Estimated velocity.

(b) Bias



(c) Estimated rotation angle.



(d) Estimated angular velocity.

(e) Estimated acceleration minus bias.

Figure C.4: Results from series 9265

Appendix D

Butterworth filter

The n -th order Butterworth filter is (Fossen 2002):

$$(n = 1) \quad h_{lp}(s) = \frac{1}{1 + s/\omega_f} \quad (\text{D.1})$$

$$(n = 2) \quad h_{lp}(s) = \frac{\omega_f^2}{s^2 + 2\zeta\omega_f s + \omega_f^2}; \quad \zeta = \sin(45^\circ) \quad (\text{D.2})$$

$$(n = 3) \quad h_{lp}(s) = \frac{\omega_f^2}{s^2 + 2\zeta\omega_f s + \omega_f^2} \cdot \frac{1}{1 + s/\omega_f}; \quad \zeta = \sin(30^\circ) \quad (\text{D.3})$$

$$(n = 4) \quad h_{lp}(s) = \prod_{i=1}^2 \frac{\omega_f^2}{s^2 + 2\zeta_i\omega_f s + \omega_f^2} \quad \zeta_1 = \sin(22.5^\circ), \quad \zeta_2 = \sin(67.5^\circ) \quad (\text{D.4})$$

where n denotes the order of the filter while ω_f is the cut-off frequency. A higher-order low-pass filter implies better disturbance suppression of the price of phase lag.

Appendix E

Data sheets

Model Number 625B01		INDUSTRIAL ICP® ACCELEROMETER		Revision G ECN #: 14824	
Performance		ENGLISH	SI	Optional Versions (Optional versions have identical specifications and accessories as listed for standard model except where noted below. More than one option may be used.)	
Sensitivity (±5 %)	100 mV/g	10.2 mV/(m/s ²)	±490 m/s ²	CS - Canadian Standards Association Approved Intrinsically Safe [7]	
Measurement Range	±50 g	30 to 3900000 cpm	0.5 to 6500 Hz	FM - Factory Mutual Certification - Intrinsically Safe [8]	
Frequency Range (±5 %)	22 to 450000 cpm	12 to 630000 cpm	0.2 to 10500 Hz	LB - Low Bias Voltage	6 to 8 VDC
Frequency Range (±10 %)	1500 kcpm	50 µg	25 kHz	Output Bias Voltage	12 to 28 VDC
Resonant Frequency	±1 %	±1 %	491 µm/s ²	Excitation Voltage	±343 m/s ²
Broadband Resolution (1 to 10000 Hz)	±1 %	±1 %	±1 %	Measurement Range	
Non-Linearity	±1 %	±1 %	±1 %	M - Metric Mount	
Transverse Sensitivity	±5 %	±5 %	±5 %	TO - Temperature Output	
Environmental		5000 g pk	49050 m/s ² pk	Temperature Output Range	+36 to +250 °F
Overload Limit (Shock)	-65 to +250 °F	See Graph	See Graph	Temperature Scale Factor	5.56 mV/°F + 32
Temperature Range	IP68			Electrical Connector	3-Pin
Temperature Response				Electrical Connections (Pin A)	Acceleration
Enclosure Rating				Electrical Connections (Pin B)	Output
Electrical				Electrical Connections (Pin C)	Ground
Settling Time (within 1% of bias)	≤8.0 sec	≤8.0 sec	≤8.0 sec	Temperature	Temperature
Discharge Time Constant	≥1.0 sec	18 to 28 VDC	18 to 28 VDC	Output	Output
Excitation Voltage	2 to 20 mA	<100 ohm	<100 ohm	Ground	Ground
Constant Current Excitation	8 to 12 VDC	24.5 (µm/s ²)/Hz	24.5 (µm/s ²)/Hz	Temperature	Temperature
Output Impedance	2.5 µg/Hz	0.8 µg/Hz	0.8 µg/Hz	Output	Output
Output Bias Voltage	0.5 µg/Hz	>10 ⁶ ohm	>10 ⁶ ohm	Ground	Ground
Spectral Noise (10 Hz)	Electrical Protection	RFI/ESD	RFI/ESD	Temperature	Temperature
Spectral Noise (100 Hz)	Physical			Output	Output
Spectral Noise (1 kHz)	Size (Diameter x Height)	1.36 in x 1.13 in	35.1 mm x 28.7 mm	Ground	Ground
Electrical Isolation (Case)	Weight	5.1 oz	145 gm	Temperature	Temperature
Electrical Protection	Mounting	Through Hole	Through Hole	Output	Output
Physical	Mounting Thread	1/4-28 Male	Not Applicable	Ground	Ground
Size (Diameter x Height)	Mounting Torque	2 to 5 ft-lb	2.7 to 6.8 N-m	Temperature	Temperature
Weight	Sensing Element	Ceramic	Ceramic	Output	Output
Mounting	Sensing Geometry	Shear	Shear	Ground	Ground
Mounting Thread	Housing Material	Stainless Steel	Stainless Steel	Temperature	Temperature
Mounting Torque	Sealing	Welded Hermetic	Welded Hermetic	Output	Output
Sensing Element	Electrical Connector	2-Pin MIL-C-5015	2-Pin MIL-C-5015	Ground	Ground
Sensing Geometry	Electrical Connection Position	Side	Side	Temperature	Temperature
Housing Material				Output	Output
Sealing				Ground	Ground
Electrical Connector				Temperature	Temperature
Electrical Connection Position				Output	Output
				Ground	Ground
				Temperature	Temperature
				Output	Output
				Ground	Ground
				Temperature	Temperature
				Output	Output
				Ground	Ground
				Temperature	Temperature
				Output	Output
				Ground	Ground
				Temperature	Temperature
				Output	Output
				Ground	Ground
				Temperature	Temperature
				Output	Output
				Ground	Ground
				Temperature	Temperature
				Output	Output
				Ground	Ground
				Temperature	Temperature
				Output	Output
				Ground	Ground
				Temperature	Temperature
				Output	Output
				Ground	Ground
				Temperature	Temperature
				Output	Output
				Ground	Ground
				Temperature	Temperature
				Output	Output
				Ground	Ground
				Temperature	Temperature
				Output	Output
				Ground	Ground
				Temperature	Temperature
				Output	Output
				Ground	Ground
				Temperature	Temperature
				Output	Output
				Ground	Ground
				Temperature	Temperature
				Output	Output
				Ground	Ground
				Temperature	Temperature
				Output	Output
				Ground	Ground
				Temperature	Temperature
				Output	Output
				Ground	Ground
				Temperature	Temperature
				Output	Output
				Ground	Ground
				Temperature	Temperature
				Output	Output
				Ground	Ground
				Temperature	Temperature
				Output	Output
				Ground	Ground
				Temperature	Temperature
				Output	Output
				Ground	Ground
				Temperature	Temperature
				Output	Output
				Ground	Ground
				Temperature	Temperature
				Output	Output
				Ground	Ground
				Temperature	Temperature
				Output	Output
				Ground	Ground
				Temperature	Temperature
				Output	Output
				Ground	Ground
				Temperature	Temperature
				Output	Output
				Ground	Ground
				Temperature	Temperature
				Output	Output
				Ground	Ground
				Temperature	Temperature
				Output	Output
				Ground	Ground
				Temperature	Temperature
				Output	Output
				Ground	Ground
				Temperature	Temperature
				Output	Output
				Ground	Ground
				Temperature	Temperature
				Output	Output
				Ground	Ground
				Temperature	Temperature
				Output	Output
				Ground	Ground
				Temperature	Temperature
				Output	Output
				Ground	Ground
				Temperature	Temperature
				Output	Output
				Ground	Ground
				Temperature	Temperature
				Output	Output
				Ground	Ground
				Temperature	Temperature
				Output	Output
				Ground	Ground
				Temperature	Temperature
				Output	Output
				Ground	Ground
				Temperature	Temperature
				Output	Output
				Ground	Ground
				Temperature	Temperature
				Output	Output
				Ground	Ground
				Temperature	Temperature
				Output	Output
				Ground	Ground
				Temperature	Temperature
				Output	Output
				Ground	Ground
				Temperature	Temperature
				Output	Output
				Ground	Ground
				Temperature	Temperature
				Output	Output
				Ground	Ground
				Temperature	Temperature
				Output	Output
				Ground	Ground
				Temperature	Temperature
				Output	Output
				Ground	Ground
				Temperature	Temperature
				Output	Output
				Ground	Ground
				Temperature	Temperature
				Output	Output
				Ground	Ground
				Temperature	Temperature
				Output	Output
				Ground	Ground
				Temperature	Temperature
				Output	Output
				Ground	Ground
				Temperature	Temperature
				Output	Output
				Ground	Ground
				Temperature	Temperature
				Output	Output
				Ground	Ground
				Temperature	Temperature
				Output	Output
				Ground	Ground
				Temperature	Temperature
				Output	Output
				Ground	Ground
				Temperature	Temperature
				Output	Output
				Ground	Ground
				Temperature	Temperature
				Output	Output
				Ground	Ground
				Temperature	Temperature
				Output	Output
				Ground	Ground
				Temperature	Temperature
				Output	Output
				Ground	Ground
				Temperature	Temperature
				Output	Output
				Ground	Ground
				Temperature	Temperature
				Output	Output
				Ground	Ground
				Temperature	Temperature
				Output	Output
				Ground	Ground
				Temperature	Temperature
				Output	Output
				Ground	Ground
				Temperature	Temperature
				Output	Output
				Ground	Ground
				Temperature	Temperature
				Output	Output
				Ground	Ground
				Temperature	Temperature
				Output	Output
				Ground	Ground
				Temperature	Temperature
				Output	Output
				Ground	Ground
				Temperature	Temperature
				Output	Output
				Ground	Ground
				Temperature	Temperature
				Output	Output
				Ground	Ground
				Temperature	Temperature
				Output	Output
				Ground	Ground
				Temperature	Temperature
				Output	Output
				Ground	Ground
				Temperature	Temperature
				Output	Output
				Ground	Ground
				Temperature	Temperature
				Output	Output
				Ground	Ground
				Temperature	Temperature
				Output	Output
				Ground	Ground
				Temperature	Temperature
				Output	Output
				Ground	Ground
				Temperature	Temperature
				Output	Output
				Ground	Ground
				Temperature	Temperature
				Output	Output
				Ground	Ground
				Temperature	Temperature
				Output	Output
				Ground	Ground
				Temperature	Temperature
				Output	Output
				Ground	Ground
				Temperature	Temperature
				Output	Output
				Ground	Ground
				Temperature	Temperature
				Output	Output
				Ground	Ground
				Temperature	Temperature
				Output	

Model Number 629A31		INDUSTRIAL ICP® ACCELEROMETER		ECN #: 10509
DYNAMIC Sensitivity (±5%) Measurement Range Frequency Range: (±5%) (±10%) (±3 dB) Mounted Resonant Frequency Amplitude Linearity Transverse Sensitivity	ENGLISH 100 mV/g ±50 g 144 - 120,000 cpm 102 - 300,000 cpm 48 - 480,000 cpm 1,200 kcpm ±1% ±5%	SI 10.2 mV/(m/s ²) ±490 m/s ² 144 - 120 000 cpm 102 - 300 000 cpm 48 - 480 000 cpm 1 200 kcpm ±1% ±5%	OPTIONAL VERSIONS Optional versions have identical specifications and accessories as listed for the standard model except where noted below. More than one option may be used. LB - Low Bias Output Bias Excitation Voltage Measurement Range	6 to 8 VDC 12 to 28 VDC ±343 m/s ² ±35 g
ENVIRONMENTAL Shock Limit Temperature Range Temperature Response	5,000 g pk -65 to +250 °F See Graph	49 050 m/s ² pk -54 to +121 °C See Graph	M - Metric Supplied Accessories: M081A59 Captive Mounting Bolt replaces 081A56	
ELECTRICAL Settling Time (within 1% of bias) Discharge Time Constant Excitation Voltage Constant Current Output Impedance Output Bias Broadband Electrical Noise (1-10 kHz) Spectral Noise: (10 Hz) (100 Hz) (1 kHz)	≤3.0 sec ≥0.2 sec 18 to 28 VDC 2 to 20 mA <100 ohms 8 to 12 VDC 100 µg 7.0 µg/√Hz 2.8 µg/√Hz 1.0 µg/√Hz >10 ⁶ ohms RFI/ESD	≤3.0 sec ≥0.2 sec 18 to 28 VDC 2 to 20 mA <100 ohms 8 to 12 VDC 981 µm/s ² 68.7 (µm/s ²)/√Hz 27.5 (µm/s ²)/√Hz 9.8 (µm/s ²)/√Hz >10 ⁶ ohms RFI/ESD	NOTES: [1] Conversion Factor 1g = 9.81 m/s ² . [2] 1 Hz = 60 cpm (cycles per minute). [3] The high frequency tolerance is accurate within 10% of the specified frequency. [4] Typical value. [5] Zero-based, least-squares, straight line method. [6] 1/4-28 has no equivalent in S.I. units.	
Case Isolation Protection MECHANICAL Size (length x width x height) Weight Mounting Thread Mounting Torque Sensing Element/Geometry Case Material Sealing Connector Type (4-pin)/Position Sensing Axis/Pin	1.5 x 1.5 x 0.82 in 4.9 oz 1/4-28 UNF-2A Ceramic/Shear Stainless Steel Welded Hermetic Mil-C-26482/Side X/A, Y/B, Z/C, Ground/D	38.1 x 38.1 x 20.8 mm 139 gm Not Applicable 2.7 to 6.8 N-m Ceramic/Shear Stainless Steel Welded Hermetic Mil-C-26482/Side X/A, Y/B, Z/C, Ground/D	SUPPLIED ACCESSORIES: Calibration Certificate (600 to 120,000 cpm) Model 081A56 Captive Mounting Bolt	
CE	<p style="text-align: center;">All specifications are at room temperature unless otherwise specified.</p> <p>ICP® is a registered trademark of PCB Piezotronics, Inc. In the interest of constant product improvement, we reserve the right to change specifications without notice.</p>			
	Form DD030 Rev.F 2/23/99			
	Date: <u>6/3/99</u> Engineer: <u>MWS</u> Sales: <u>SJD</u> Approved: <u>N.F.</u> Spec Number: <u>8317</u>	Date: <u>6/3/99</u> Date: <u>6/1/99</u>	E-Mail: imisales@pcb.com Fax (716) 684-3823 800-959-4464 3425 Walden Avenue, Depew, NY 14043	

Figure E.2: Data Sheet of the accelerometer 629A31.

S P E C I F I C A T I O N S

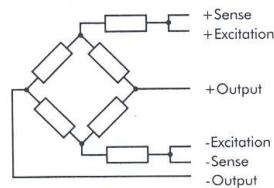
PARAMETER		
Standard Ranges U4000	N	10, 25, 50, 100, 250, 500,
	kN	1, 2, 5, 10, 15, 25, 50
Standard Ranges U4100	N	50, 100, 250, 500
Standard Ranges U4200	kN	5, 10, 25, 50, 100, 200
Recommended Excitation Voltage	VDC	10
Maximum Excitation Voltage	VDC	15
Full Scale Output (FSO) U4000	mV/V	2.7 nominal
Full Scale Output (FSO) U4100	mV/V	2.0 nominal
Full Scale Output (FSO) U4200	mV/V	2.0 ± 0.1
Non Linearity	%FSO	<±0.03 (±0.05 U4100) (±0.04 U4200)
Zero Return	%FSO	<±0.015
Operating Temperature Range	°C	-20 to +80
Compensated Temperature Range	°C	0 to +60
Thermal Zero Shift	%FSO/°C	<±0.002 (<±0.02 U4100)
Thermal Sensitivity Shift	% reading /°C	<±0.002 (<±0.005 U4100)
Input Resistance	Ω	375 nominal
Output Resistance	Ω	350 nominal
Overload Capacity	%FSO	150
Maximum Side load	%FSO	50
Barometric Effect		None
Environmental Protection Level U4000 & U4100	IEC 529	IP51 (IP65 available on U4000≥ 500N)
Environmental Protection Level U4200	IEC 529	IP67
Documentation		Individual Calibration Certificate supplied

Continuous product development may result in minor specification changes without notice. All dimensions shown in millimetres.
 Note: Drawings shown are for general guidance only. Detailed installation drawings are available on request.

OPTIONS

- Spherical rod end bearings
- Base plate and spherical load button
- High performance version
- Dual bridge version
- Integral mechanical overload stops

Other Special Versions may be available on request.



NOTES

Cable screen not connected to load cell body
 The sense wires are provided for precision measurements
 Polarity shown when configured for tension operation

ORDERING INFORMATION

Order by specifying type No., range and options e.g. U4000-50N

mi Maywood
Instruments

THAMES SIDE-MAYWOOD LIMITED
 17 Stadium Way, Tilehurst,
 Reading, Berkshire, RG30 6BX UK.
 Tel: +44 (0)118 945 8200
 Fax: +44 (0)118 945 8225

A
HALMA
GROUP
COMPANY

Figure E.3: Data Sheet of the load-cells. The one used on the test facilities is U4200.



Model 350B50

Product Type: Accelerometer, Vibration Sensor

High amplitude, shock, triaxial ICP® accel., 0.5 mV/g, 10k g range, w/built-in 2nd order low-pass filter (-3dB at 20 kHz)

PERFORMANCE	ENGLISH	SI
Sensitivity ($\pm 30\%$)	0.5 mV/g	0.05 mV/(m/s ²)
Measurement Range	$\pm 10,000$ g pk	$\pm 98,000$ m/s ² pk
Frequency Range (± 1 dB)	3 to 10,000 Hz	3 to 10,000 Hz
(-3 dB)	1.5 to 20,000 Hz	1.5 to 20,000 Hz [2]
Resonant Frequency	≥ 60 kHz	≥ 60 kHz
Broadband Resolution (1 to 10,000 Hz)	0.03 g rms	0.29 m/s ² rms [1]
Non-Linearity	$\leq 2\%$	$\leq 2\%$ [3]
Transverse Sensitivity	$\leq 5\%$	$\leq 5\%$
ENVIRONMENTAL		
Overload Limit (Shock)	$\pm 25,000$ g pk	$\pm 245,000$ m/s ² pk
Temperature Range (Operating)	-65 to +250 °F	-54 to +121 °C
Temperature Response	See Graph	See Graph [1]
ELECTRICAL		
Excitation Voltage	18 to 30 VDC	18 to 30 VDC
Constant Current Excitation	2 to 20 mA	2 to 20 mA
Output Impedance	≤ 100 ohm	≤ 100 ohm
Output Bias Voltage	8 to 12 VDC	8 to 12 VDC
Discharge Time Constant	0.5 to 1.0 sec	0.5 to 1.0 sec
Settling Time (within 10% of bias)	<5 sec	<5 sec
Electrical Isolation (Base)	$>10^8$ ohm	$>10^8$ ohm
PHYSICAL		
Sensing Element	Ceramic	Ceramic
Sensing Geometry	Shear	Shear
Housing Material	Titanium	Titanium
Sealing	Hermetic	Hermetic
Size (Height x Length x Width)	0.33 in x 0.69 in x 0.69 in	8.4 mm x 17.5 mm x 17.5 mm
Weight (without cable)	0.3 oz	8.6 gm [1]
Electrical Connector	Integral Cable	Integral Cable
Electrical Connection Position	Side	Side
Cable Termination	1/4-28 4-Pin Jack	1/4-28 4-Pin Jack
Cable Length	5.0 ft	1.52 m
Cable Type	034 4-cond Shielded	034 4-cond Shielded
Mounting	Through Hole	Through Hole
SUPPLIED ACCESSORIES:		
Model 034G05 4-cond. shielded cable, 5 ft (1.5M), 4-pin plug to (3) BNC plugs (1)		
Model 080A197 MOUNTING BASE FOR 350B50 (1)		
Model 081M158 6-32 MOUNTING SCREW (4)		
Model ACS-22 NIST Traceable frequency response (100Hz to ± 1 dB point) (1)		

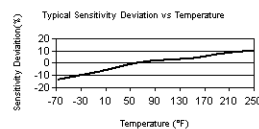
All specifications are at room temperature unless otherwise specified.

NOTES:

[1] Typical.

[2] Electrical filter is a second order filter.

[3] Zero-based, least-squares, straight line method.



In the interest of constant product improvement, we reserve the right to change specifications without notice.

Figure E.4: Model 350B50 Spec Sheet.

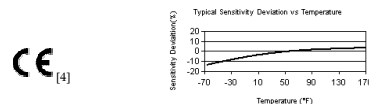


Model 356A12
Product Type: Accelerometer, Vibration Sensor
 Triaxial, mini (5 gm) high sensitivity ICP® accel., 100 mV/g, 0.5 Hz to 5 kHz (+/- 5%), 5 ft attached cable

PERFORMANCE	ENGLISH	SI
Sensitivity (± 10 %)	100 mV/g	10.2 mV/(m/s ²)
Measurement Range	± 50 g pk	± 491 m/s ² pk
Frequency Range (± 5 %)	0.5 to 5000 Hz	0.5 to 5000 Hz
(± 5 %)	0.5 to 5000 Hz	0.5 to 5000 Hz
(± 10 %)	0.4 to 6000 Hz	0.4 to 6000 Hz
(± 10 %)	0.4 to 6000 Hz	0.4 to 6000 Hz
Resonant Frequency	≥ 25 kHz	≥ 25 kHz
Broadband Resolution (1 to 10,000 Hz)	0.0002 g rms	0.002 m/s ² rms [1]
Non-Linearity	≤ 1 %	≤ 1 % [2]
Transverse Sensitivity	≤ 5 %	≤ 5 %
ENVIRONMENTAL		
Overload Limit (Shock)	± 5000 g pk	± 49,050 m/s ² pk
Temperature Range (Operating)	-65 to +170 °F	-54 to +77 °C
Temperature Response	See Graph	See Graph [1]
Base Strain Sensitivity	0.001 g/µε	0.01 (m/s ²)/µε [1]
ELECTRICAL		
Excitation Voltage	18 to 30 VDC	18 to 30 VDC
Constant Current Excitation	2 to 20 mA	2 to 20 mA
Output Impedance	≤ 200 ohm	≤ 200 ohm
Output Bias Voltage	8 to 12 VDC	8 to 12 VDC
Discharge Time Constant	1 to 3 sec	1 to 3 sec
Settling Time (within 10% of bias)	<10 sec	<10 sec
Spectral Noise (1 Hz)	50 µg/√Hz	490 (µm/s ²)/√Hz [1]
(10 Hz)	20 µg/√Hz	196 (µm/s ²)/√Hz [1]
(100 Hz)	5 µg/√Hz	49 (µm/s ²)/√Hz [1]
(1 kHz)	2 µg/√Hz	19.8 (µm/s ²)/√Hz [1]
(10 kHz)	1 µg/√Hz	9.8 (µm/s ²)/√Hz [1]
PHYSICAL		
Sensing Element	Ceramic	Ceramic
Sensing Geometry	Shear	Shear
Housing Material	Titanium	Titanium
Sealing	Hermetic	Hermetic
Size (Height x Length x Width)	0.45 in x 0.45 in x 0.45 in	11.4 mm x 11.4 mm x 11.4 mm
Weight (without cable)	0.19 oz	5.4 gm [1]
Electrical Connector	Integral Cable	Integral Cable
Electrical Connection Position	Side	Side
Cable Termination	1/4-28 4-Pin Jack	1/4-28 4-Pin Jack
Cable Length	5 ft	1.5 m
Cable Type	034 4-cond Shielded	034 4-cond Shielded
Mounting Thread	5-40 Female	5-40 Female
Mounting Torque	4 to 5	45 to 55
SUPPLIED ACCESSORIES:		
Model 034G05 4-cond. shielded cable, 5 ft (1.5M), 4-pin plug to (3) BNC plugs (1)		
Model 080A Adhesive Mounting Base (1)		
Model 080A109 Petro Wax (1)		
Model 081A27 Mounting Stud (5-40 to 5-40) (1)		
Model 081A90 Mounting stud, 10-32 to 5-40 (1)		
Model ACS-1T NIST traceable triaxial amplitude response, 10 Hz to upper 5% frequency. (1)		
Model M081A27 Metric mounting stud, 5-40 to M3 x 0.50 long (1)		

All specifications are at room temperature unless otherwise specified.

- NOTES:
 [1] Typical.
 [2] Zero-based, least-squares, straight line method.
 [3] TEDS Capable Digital Memory and Communication, compliant with IEEE P1451.4
 [4] See PCB Declaration of Conformance PS023 for details.



In the interest of constant product improvement, we reserve the right to change specifications without notice.

Figure E.5: Model 356A12 Spec Sheet.



Model 352C23

Product Type: Vibration Sensor, Accelerometer

Miniature, lightweight (0.2 gm), ceramic shear ICP® accel., 5 mV/g, 2 to 10k Hz, 10-ft detachable cable

PERFORMANCE	ENGLISH	SI
Sensitivity ($\pm 20\%$)	5 mV/g	0.5 mV/(m/s ²)
Measurement Range	± 1000 g pk	± 9810 m/s ² pk
Frequency Range ($\pm 5\%$)	2.0 to 10,000 Hz	2.0 to 10,000 Hz
($\pm 10\%$)	1.5 to 15,000 Hz	1.5 to 15,000 Hz
(± 3 dB)	0.7 to 25,000 Hz	0.7 to 25,000 Hz
Resonant Frequency	≥ 70 kHz	≥ 70 kHz
Broadband Resolution (1 to 10,000 Hz)	0.003 g rms	0.03 m/s ² rms [1]
Non-Linearity	$\leq 1\%$	$\leq 1\%$ [2]
Transverse Sensitivity	$\leq 5\%$	$\leq 5\%$
ENVIRONMENTAL		
Overload Limit (Shock)	$\pm 10,000$ g pk	$\pm 98,000$ m/s ² pk
Temperature Range (Operating)	-65 to +250 °F	-54 to +121 °C
Temperature Response	See Graph	See Graph [1]
ELECTRICAL		
Excitation Voltage	18 to 30 VDC	18 to 30 VDC
Constant Current Excitation	2 to 20 mA	2 to 20 mA
Output Impedance	≤ 200 ohm	≤ 200 ohm
Output Bias Voltage	7 to 11 VDC	7 to 11 VDC
Discharge Time Constant	0.1 to 1.0 sec	0.1 to 1.0 sec
Settling Time (within 10% of bias)	<3 sec	<3 sec
Spectral Noise (1 Hz)	1500 $\mu\text{g}/\sqrt{\text{Hz}}$	14,715 ($\mu\text{m}/\text{s}^2$)/ $\sqrt{\text{Hz}}$ [1]
(10 Hz)	400 $\mu\text{g}/\sqrt{\text{Hz}}$	3924 ($\mu\text{m}/\text{s}^2$)/ $\sqrt{\text{Hz}}$ [1]
(100 Hz)	120 $\mu\text{g}/\sqrt{\text{Hz}}$	1177 ($\mu\text{m}/\text{s}^2$)/ $\sqrt{\text{Hz}}$ [1]
(1 kHz)	30 $\mu\text{g}/\sqrt{\text{Hz}}$	294 ($\mu\text{m}/\text{s}^2$)/ $\sqrt{\text{Hz}}$ [1]
(10 kHz)	20 $\mu\text{g}/\sqrt{\text{Hz}}$	196 ($\mu\text{m}/\text{s}^2$)/ $\sqrt{\text{Hz}}$ [1]
Electrical Isolation (Base)	$>10^8$ ohm	$>10^8$ ohm
PHYSICAL		
Sensing Element	Ceramic	Ceramic
Sensing Geometry	Shear	Shear
Housing Material	Anodized Aluminum	Anodized Aluminum
Sealing	Epoxy	Epoxy
Size (Height x Length x Width)	.11 in x 0.34 in x 0.16 in	2.8 mm x 8.6 mm x 4.1 mm
Weight	0.007 oz	0.2 gm [1]
Electrical Connector	3-56 Coaxial Jack	3-56 Coaxial Jack
Electrical Connection Position	Side	Side
Mounting	Adhesive	Adhesive
SUPPLIED ACCESSORIES:		
Model 030A10 Coax Cable, 10 ft (3 m), 3-56 plug to 10-32 plug. (1)		
Model 039A26 Removal Tool (1)		
Model 080A109 Petro Wax (1)		
Model ACS-1 NIST traceable frequency response (10 Hz to upper 5% point). (1)		

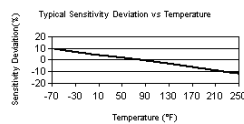
All specifications are at room temperature unless otherwise specified.

NOTES:

- [1] Typical.
 [2] Zero-based, least-squares, straight line method.
 [3] TEDS Capable Digital Memory and Communication, compliant with IEEE P1451.4
 [4] See PCB Declaration of Conformance PS023 for details.



[4]



In the interest of constant product improvement,
 we reserve the right to change specifications without notice.

Figure E.6: Model 352C23 Spec Sheet.



Model 3901F3HB2000G

Product Type: Accelerometer, Vibration Sensor

Piezoresistive accel., 0.2 mV/g, full active bridge design, w/4-cond., 25-ft integral cable

PERFORMANCE	ENGLISH	SI
Sensitivity ($\pm 20\%$)	0.2 mV/g	0.02 mV/(m/s ²)
Measurement Range	± 2000 g pk	$\pm 19,620$ m/s ² pk
Frequency Range ($\pm 5\%$)	0 to 5000 Hz	0 to 5000 Hz
(± 1 dB)	0 to 7000 Hz	0 to 7000 Hz
Resonant Frequency	>25 kHz	>25 kHz
Non-Linearity	$\leq 2.0\%$	$\leq 2.0\%$ [3]
Transverse Sensitivity	$\leq 5\%$	$\leq 5\%$ [4]
ENVIRONMENTAL		
Overload Limit (Shock)	$\pm 10,000$ g pk	$\pm 98,100$ m/s ² pk [2]
Temperature Range (Operating)	0 to 150 °F	-18 to 66 °C
(Storage)	-65 to 250 °F	-54 to 121 °C
Temperature Coefficient of Sensitivity	$\pm 0.06\%$ /°F	$\pm 0.107\%$ /°C [1]
Zero g Offset Temperature Shift	± 25 mV	± 25 mV [1]
ELECTRICAL		
Excitation Voltage	10.0 VDC	10.0 VDC
Current Consumption	20 mA	20 mA [1]
Input Resistance (± 50)	2000 ohm	2000 ohm [1]
Output Resistance (± 50)	1000 ohm	1000 ohm [1]
Offset Voltage	± 50 mVDC	± 50 mVDC
Electrical Isolation (Base)	$\geq 10^8$ ohm	$\geq 10^8$ ohm
PHYSICAL		
Housing Material	Anodized Aluminum	Anodized Aluminum
Sealing	Epoxy	Epoxy
Size (Height x Length x Width)	0.205 in x 0.400 in x 0.400 in	5.21 mm x 10.16 mm x 10.16 mm
Weight	0.07 oz	2.0 gm [1]
Electrical Connector	Integral Cable	Integral Cable
Electrical Connection Position	Side	Side
Cable Type	036 4-cond silicone jacket	036 4-cond silicone jacket
Cable Length	25 ft	7.62 m
Mounting	Through Holes (2)	Through Holes (2)
SUPPLIED ACCESSORIES:		
Model 039A30 Allen wrench, 0.050 hex (1)		
Model 080A191 Skt hd cap screw, 0-80x3/16" with washer (2)		
Model ACS-29 Calibration of Piezoresistive Accelerometers		

All specifications are at room temperature unless otherwise specified.

NOTES:

[1] Typical.

[2] Half-sine pulse duration, ≥ 200 μ sec.

[3] Zero-based, least-squares, straight line method.

[4] Transverse sensitivity is typically $\leq 3\%$.

**In the interest of constant product improvement,
we reserve the right to change specifications without notice.**

Figure E.7: Model 3901F3HB2000G Spec Sheet.



Model 3703D1FE50G

Product Type: Vibration Sensor, Accelerometer

Triaxial capacitive accel., 40 mV/g, +/- 50 g, 5-30 VDC excitation voltage, 10-ft integral cable

View [photo](#) and [drawing](#).

PERFORMANCE	ENGLISH	SI	
Sensitivity ($\pm 5\%$)	40 mV/g	4.1 mV/(m/s ²)	[4]
Measurement Range	± 50 g pk	± 490 m/s ² pk	
Frequency Range ($\pm 5\%$)	0 to 450 Hz	0 to 450 Hz	
($\pm 10\%$)	0 to 600 Hz	0 to 600 Hz	
Resonant Frequency	>1.5 kHz	>1.5 kHz	
Phase Response (100 Hz)	<10 °	<10 °	
Damping Ratio	55 % Critical	55 % Critical	[2]
Broadband Resolution (0.5 to 100 Hz)	240 μ g rms	2350 μ m/s ² rms	[2]
Non-Linearity	$\leq 1\%$	$\leq 1\%$	[5]
Transverse Sensitivity	$\leq 3\%$	$\leq 3\%$	[6]
ENVIRONMENTAL			
Overload Limit (Shock)	± 2000 g pk	$\pm 19,600$ m/s ² pk	
Temperature Range (Operating)	-40 to +185 °F	-40 to +85 °C	
(Storage)	-85 to +250 °F	-65 to +121 °C	
Temperature Coefficient of Sensitivity	$\leq 0.042\%$ /°F	$\leq 0.076\%$ /°C	[3]
Zero g Offset Temperature Coefficient	$\leq 0.015\%$ /°F	≤ 0.268 m/s ² /°C	[3]
Base Strain Sensitivity	0.0001 g/ μ ε	0.001 (m/s ²)/ μ ε	[2]
Magnetic Sensitivity	65 equiv. μ g/gauss	6.38 (m/s ²)/Tesla	[2]
ELECTRICAL			
Excitation Voltage	5 to 30 VDC	5 to 30 VDC	
Current Consumption	≤ 30 mA	≤ 30 mA	
Output Impedance	≤ 50 ohm	≤ 50 ohm	
Offset Voltage (0 g)	± 30 mVDC	± 30 mVDC	[1]
Spectral Noise (1 Hz)	65 μ g/ $\sqrt{\text{Hz}}$	640 (μ m/s ²)/ $\sqrt{\text{Hz}}$	[2]
(10 Hz)	25 μ g/ $\sqrt{\text{Hz}}$	245 (μ m/s ²)/ $\sqrt{\text{Hz}}$	[2]
(100 Hz)	15 μ g/ $\sqrt{\text{Hz}}$	147 (μ m/s ²)/ $\sqrt{\text{Hz}}$	[2]
Electrical Isolation (Base)	>10 ⁸ ohm	>10 ⁸ ohm	
PHYSICAL			
Housing Material	Titanium	Titanium	
Sealing	Epoxy	Epoxy	
Size (Length x Width x Height)	1.1 in x 1.1 in x 1.1 in	28 mm x 28 mm x 28 mm	
Weight (with cable)	5.9 oz	168.7 gm	
Electrical Connector	Integral Cable	Integral Cable	
Electrical Connection Position	Side	Side	
Cable Type	037 10-cond Shielded	037 10-cond Shielded	
Cable Length	10 ft	3.05 m	
Mounting Thread	10-32 Female	10-32 Female	
SUPPLIED ACCESSORIES:			
Model 080A190 Adhesive Mounting Base (1)			
Model 081A05 Mounting stud, 10-32 to 10-32 x 0.27" long, BeCu (H900), no shoulder (1)			
Model ACS-11T NIST traceable amplitude response calibration from 0.5 Hz to upper point. (1)			
Model M081A05 Mounting Stud (1)			
OPTIONAL VERSIONS			
HT - High temperature, extends normal operation temperatures			
Temperature Range (Operating)	-40 to +250 °F	-40 to +121 °C	

All specifications are at room temperature unless otherwise specified.

NOTES:

[1] Offset tolerance is based on manufacturers supplied cable length.

[2] Typical.

[3] Valid from 70°F to 185°F [21°C to 85°C]

[4] Measured at 100 Hz, 1 grms.

[5] Zero-based, least-squares, straight line method.

[6] Transverse sensitivity is typically $\leq 1.5\%$

[7] See PCB Declaration of Conformance PS027 for details.



In the interest of constant product improvement,
we reserve the right to change specifications without notice.

Figure E.8: Model 3703D1FE50G Spec Sheet.

Model 650A10

Product Type: Accelerometer, Vibration Sensor

Industrial, capacitive accel., 10 mV/g, +/- 200 g, 16 VDC excitation voltage, 10-ft integral cable

View [drawing](#).

PERFORMANCE	ENGLISH	SI
Sensitivity ($\pm 5\%$)	10 mV/g	1.02 mV/(m/s ²) [4]
Measurement Range	± 200 g pk	± 1961 m/s ² pk
Frequency Range ($\pm 5\%$)	0 to 48,000 cpm	0 to 800 Hz
($\pm 10\%$)	0 to 600,000 cpm	0 to 1000 Hz
Resonant Frequency	>150 kcpm	>2.5 kHz
Phase Response (100 Hz)	<5 °	<5 °
Damping Ratio	70 % Critical	70 % Critical [2]
Broadband Resolution (0.5 to 100 Hz)	450 μ g rms	4410 μ /(m/s ²) rms [2]
Non-Linearity	$\leq 1\%$	$\leq 1\%$ [5]
Transverse Sensitivity	$\leq 5\%$	$\leq 5\%$ [6]
ENVIRONMENTAL		
Overload Limit (Shock)	± 3000 g pk	$\pm 29,400$ m/s ² pk
Temperature Range (Operating)	-40 to +185 °F	-40 to +85 °C
(Storage)	-85 to +250 °F	-65 to +121 °C
Zero g Offset Temperature Coefficient	≤ 0.035 g/°F	≤ 0.613 m/s ² /°C [3]
Base Strain Sensitivity	0.0005 g/ μ ϵ	0.005 (m/s ²)/ μ ϵ [2]
Magnetic Sensitivity	3 equiv. μ g/gauss	0.3 (m/s ²)/Tesla [2]
Temperature Response	$\leq 0.042\%$ /°F	$\leq 0.076\%$ /°C [3]
ELECTRICAL		
Excitation Voltage	16 to 30 VDC	16 to 30 VDC
Current Consumption	≤ 10 mA	≤ 10 mA
Output Impedance	≤ 50 ohm	≤ 50 ohm
Offset Voltage (0 g)	± 40 mVDC	± 40 mVDC [1]
Spectral Noise (1 Hz)	210 μ g/ $\sqrt{\text{Hz}}$	2060 (μ m/s ²)/ $\sqrt{\text{Hz}}$ [2]
(10 Hz)	55 μ g/ $\sqrt{\text{Hz}}$	540 (μ m/s ²)/ $\sqrt{\text{Hz}}$ [2]
(100 Hz)	25 μ g/ $\sqrt{\text{Hz}}$	245 (μ m/s ²)/ $\sqrt{\text{Hz}}$ [2]
Electrical Isolation (Case)	>10 ⁸ ohm	>10 ⁸ ohm
PHYSICAL		
Housing Material	Stainless Steel	Stainless Steel
Sealing	Hermetic	Hermetic
Size (Hex x Height)	7/8 in x 4.29 in	22.2 mm x 108 mm
Weight	2.7 oz	76.5 gm [2]
Electrical Connector	Integral Cable	Integral Cable
Electrical Connection Position	Top	Top
Cable Type	059 4-cond Shielded	059 4-cond Shielded
Cable Length	10 ft	3 m
Cable Termination	Pigtail	Pigtail
Mounting Thread	1/4-28 Female	No Metric Equivalent
SUPPLIED ACCESSORIES:		
Model 080A109 Petro Wax (1)		
Model 081B20 Mounting Stud, with shoulder (1/4-28 to 1/4-28) (1)		
Model ACS-11 NIST traceable amplitude and phase response from 0.5 Hz to upper 5% frequency (1)		
OPTIONAL VERSIONS		
M - Metric Mount		
Supplied Accessory : Model M081B20 Mounting Stud 1/4-28 to M6 X 0.75 (1) replaces Model 081B20		

*All specifications are at room temperature unless otherwise specified.***NOTES:**

[1] Offset tolerance is based on manufacturers supplied cable length.

[2] Typical value.

[3] Valid from 70°F to 185°F [21°C to 85°C]

[4] Measured at 1,800 cpm, 1 grms [(30 Hz)(9.8 m/s² rms)].

[5] Zero-based, least-squares, straight line method.

[6] Transverse sensitivity is typically $\leq 3\%$.[Download Drawing \(PDF\)](#)

In the interest of constant product improvement,
we reserve the right to change specifications without notice.

Figure E.9: Model 650A10 Spec Sheet.

Appendix F

CD-ROM contents

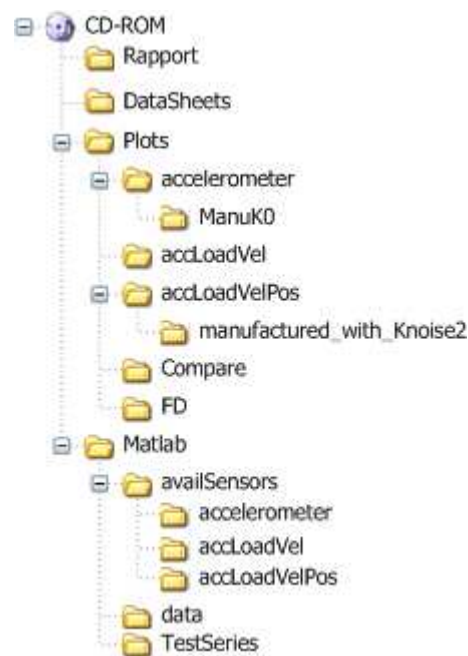


Figure F.1: CD-ROM contents.

F.1 Plots

All the plots from the simulations are in the file 'Plots'. The simulations with accelerometer as only sensor are in the file 'acceleration', which has the subfile 'ManuK0' that contains the plots from the manufactured input signal without noise. 'accLoadVel' contains the plots from the simulation with all sensors except the range finders. The results from the Kalman filter simulation with all sensors are in the file 'accLoadVelPos', while 'manufactured_with_Knoise2' contains the plots from the manufactured input signal with noise.

'FD' contains the force/displacement plots, and 'Compare' contains the raw output from the accelerometers in every direction.

F.2 Matlab files

accKalmanScript.m Main file for the Kalman filter using only the acceleration measurements. Uses the file accKalman.mdl.

accLoadVelKalmanScript.m Main file for the Kalman filter using acceleration, load-cell and velocity measurements. Uses the file accLoadVelKalman.mdl.

accLoadVelPosKalmanScript.m Main file for the Kalman filter using acceleration, load-cell, range finder and velocity measurements. Uses the file accLoadVelPosKalman.mdl.

compare.m Compares plots from different test series.

correctedForceDisplacement.m Function to compute the new PGB measurements with rotation correction.

determineRotation.m Determines when the rotation takes place

generateSignal.m Generates the manufactured data to test the Kalman filter's performance.

Hastighet.m Function for computing the impact velocity.

loadAcceleration.m Creates *.m files with the acceleration measurements from the *wk1 files containing all sensor data.

loadLoadcells.m Creates *.m files with the load-cell measurements from the *wk1 files containing all sensor data.

loadPosGiverBar.m Creates *.m files with the range finder measurements from the *wk1 files containing all sensor data.

loadVelocity.m Creates *.m files with the velocity measurements from the *wk1 files containing all sensor data.

plotCompare.m Plots the results from compare.m.

rotAcc.m Function to generate the manufactured angular acceleration.

rotFromPGB.m Calculates the rotation from range finder measurements.

accKalman.mdl Simulink model for accKalmanScript.m.

accLoadVelKalman.mdl Simulink model for accLoadVelKalmanScript.m.

accLoadVelPosKalman.mdl Simulink model for accLoadVelPosKalmanScript.m.

fabrication.mdl Used in the making of the manufactured data set.